



UNIVERSITÀ DEGLI STUDI DI NAPOLI
“FEDERICO II”

**International PhD program on Novel Technologies for
Materials, Sensors and Imaging
XXII cycle**

***Monitoring of laser – biological tissue
interaction on plane angioma by
functional infrared imaging***

Massimo Rippa

Supervisor:
Dr. Pasquale Mormile

*For Veronica,
the light of my life*

TABLE OF CONTENTS

Introduction	i-iv
---------------------------	------

Chapter 1

LASER – BIOLOGICAL TISSUE INTERACTION

1.1 Introduction.....	1
1.2 Reflection and refraction of the tissue.....	2
1.3 Absorption of the biological tissue.....	3
1.4 Scattering.....	5
1.5 Turbid media.....	7
1.6 Laser-Tissue: Interaction Mechanisms.....	9
1.6.1 Thermal Interaction.....	10
1.6.2 Photochemical Interaction.....	19
1.6.3 Photoablation.....	20
1.6.4 Plasma-induced Ablation.....	23
1.6.5 Photodisruption.....	25
1.7 Laser Applications in the medical field.....	27

Chapter 2

INFRARED IMAGING: Principles and applications

2.1 Introduction.....	32
2.2 Passive thermography.....	34
2.3 Active thermography: Testing procedures.....	35
2.3.1 Pulsed Thermography.....	37
2.3.1.1 The complete thermogram sequence.....	40
2.3.1.2 Definitions of thermal contrast.....	42
2.3.2 Step Heating (Long Pulse).....	47
2.3.3 Lock-in Thermography.....	49
2.3.4 Vibrothermography.....	50
2.4 Infrared detectors.....	52
2.4.1 Atmospheric Transmittance.....	53
2.4.2 Bolometers.....	55
2.4.3 Pyroelectric detectors.....	56
2.4.4 Quantum Detectors.....	57
2.5 Infrared Imaging Devices: Focal Plane Arrays (FPA).....	58
2.5.1 Detectors: Performance parameters.....	60
2.6 New approach of infrared imaging in medical science.....	62

Chapter 3

INFRARED MONITORING ON PLANE ANGIOMA: PT model and numerical simulation

3.1	Introduction.....	65
3.2	Infrared monitoring of plane angioma treatment: approach description.....	65
3.3	Plane angioma pathology (Port Wine Stain).....	70
3.4	Pulsed Thermography model.....	72
3.4.1	Formulation of the forward problem: 3D thermal quadrupoles.....	73
3.4.2	Resolution of the forward problem: mathematical perturbations.....	77
3.4.3	Evaluation of the depth.....	80
3.4.4	Evaluation of the thickness.....	81
3.4.5	Statistical analysis of the accuracy of the inversion procedures.....	82
3.5	Numerical simulation: biometric heat transfer model.....	84
3.5.1	Model Computation.....	86

Chapter 4

EXPERIMENTAL AND NUMERICAL RESULTS

4.1	Introduction.....	88
4.2	Materials and method.....	89
4.3	Preliminary results and observations.....	92
4.4	Pulsed Thermography model: experimental results	97
4.5	Numerical simulations: results.....	100
4.6	Limit conditions for applications of laser treatments.....	116
4.7	Final conclusions: set of laser parameters.....	117

General Conclusions.....	120
---------------------------------	------------

<i>References.....</i>	<i>125</i>
------------------------	------------

Introduction

The application field that attracted a great deal of attention has been the medicine since the birth of the laser. From the beginning it was considered as a very potential and promising tool for several different application in medicine. Nevertheless nobody could have imagined at that time the development and the enormous effect of its use in so many different sectors of medicine ranging from surgery to oncology, from urology to ophtalmology, from ginecology to dermatology, from physiotherapy to aesthetic medicine. Nowadays the use of laser has become a very common practice in all the medicine sectors and with different pathologies. These pathologies have been cured thanks to the use of different laser sources, selected as a function of both wavelengths and power, and to more and more sophisticated technologies. We can just think to very complicated surgery operation which are performed in a successful way with the help of laser-scalpel, or to skin tumours treated with coherent light, to operation with laser endoscopy which is now the common practice, to get up to aesthetic, ophtalmology, and dermatological operations, and so on.

Dermatology is one of the medical field in which laser action has been succesfully employed. Deseases like skin melanoms and angioma are usually treated with laser theraphy. In this field, during the last decades, technology supplied laser sources with technical properties specifically designed in order to accomplish the specific requirements of several application. Nowadays dermatologists can rely on a wide range of lasers which vary in wavelengths (some of them out of the visible range) and thus they can be selectively employed according to the specific application and type of pathology. The activity of the doctor consists in applying the laser light for a specific time and with a fixed intensity in the area of interest of the skin of the patient. After, he verifies the effects induced by the light laser after one or two weeks time. The physician usually makes use of the laser on his patient in an empirical way. Basically, just according to his own experience he decides the duration of the application and the intensity of laser light on the skin according to some parameters such as the individual patient, the pathology and the skin phototype. In most of the treatments what happens is that the doctor has no possibility to directly evaluate the effect of the laser applied on line since the wavelength of

it is not in the visible range or it is pulsed. This means flashes of few milliseconds too fast to be recorded by the eyes. This limits the operation of the doctor because the beam power chosen might be too low or too high on one side or the duration of the pulse too short or too long respectively. The information comes only after a few days or weeks later to the physician. And this seems to be the only remarkable limit in the application of laser in dermatology. It is important to underline that the doctor should always work under a safe regime for the patient. This means that he has to avoid damages like scars which might occur since he has no direct vision of the interaction light-treated tissues and so he usually prefers working with a lower intensity of light. This aspect, on one side means a safer situation for the patient but on the other side minimize the efficacy of the therapy making the cure time longer. The possibility to give to the doctor a tool which makes him able to monitor on-line the reaction of the skin during the laser application (and not just examining the post application effects) means:

- 1- To enhance the performances of the light effect enlarging remarkably the application fields
- 2- To optimize the action in itself in terms of both efficiency and curing times.

In photothermal regime, since the effect of the application of laser light on skin is linked to the local temperature induced, it is possible to evaluate the effects of such an interaction studying the thermal dynamic and in general the thermal behaviour of the tissues.

In this view infrared thermography seems to be the best solution. Thanks to this technique, it is possible to achieve information about thermal interaction of surface and subsurface structure of the target under investigation by analysis and images elaboration.

In the laser therapy field, infrared imaging technology can be used for a real-time monitoring of the laser-biological tissue interaction. This technique makes possible the direct evaluation about the reaction of the tissue in the specific region treated.

The equipment capable of performing such measures is the infrared camera since it supplies thermal images which represent the dynamic thermal evolution laser induced.

In the research activity of this work-thesis, the main pathology monitored and studied by infrared technique has been the Plane Angioma known as Port Wine Stain (PWS) pathology. This pathology is a vascular malformation that consists of a blood vessels accumulation under the tissue. This accumulation form a subsurface *plane of vessels* of depth and thickness depending on the specific anatomic region and, in general, different from case to case.

It's possible to obtain information about the specific plane of blood vessels under treatment monitoring the thermal reaction of the tissue under laser action by IR imaging technique.

The main target of this study are:

- To evaluate the support of the infrared imaging, in the dermatological field, as a tool for scientific investigation

And in particular way

- To evaluate the employment of this technique as a tool for the control and optimization of laser parameters in order to make the treatment safer and more efficient

In this work a novel methodological approach for the laser parameters optimization in the treatment on plane angioma is proposed. In particular, with this approach, an active thermography model, present in the literature, is employed in order to find morphological information for a specific plane angioma.

With this model from the temporal evolution of the temperature obtained on the tissue after a single laser pulse-test (heat source), it is possible to get a local evaluation of the depth and thickness of the plane of blood vessels in the anatomic area that the physician wants to treat. This information permits a morphological reconstruction of the multilayer biological tissue under treatment. Subsequently, a 2D+1 numerical simulation based on a biometric heat transfer model is executed on this multilayer. With the simulations the thermal behaviour of the biological multilayers can be achieved for different set of laser parameters as input.

By the evaluations obtained with this approach, the operator can adjust the laser parameters for each specific therapy in a proper way changing the intensity and the duration of the laser light according to the type of plane of vessels and to the skin phototype treated. This allows to specialists to employ laser systems in a more specific, well controlled and less empiric way.

The research activity, theoretical and experimental, object of this thesis work, is described in four chapters.

In the first chapter the fundamental theoretical concept of the laser–tissue interaction are presented. In particular, the main interaction mechanisms as the photothermal interaction, the photochemical interaction, the photoablation, the plasma-induced ablation and the photodisruption are described. The chapter conclude with the state of art of the laser application in medical field.

In the second chapter the priciples and applications of the infrared imaging technique are reported. The passive and active approach are explained. The problems relative to atmospheric trasmittance and infrared detectors are treated. At the end of the chapter, our novel approach and , in particular, the new application of infrared imaging in medical science are discussed.

The third chapter, is the reading key for the understanding of the experimental work presented in this thesis. A detailed description of the activity research is given. The novel approach proposed and realized, the pathology analized and computation instruments used are treated and discussed. Particularly, the pulsed thermography model and the numerical approach employed in the operative protocol performed are explained in detail.

In the last chapter, the main experimental and numerical results found are reported and discussed. The main characteristic of the laser tool and the infrared cameras used in the monitoring are showed. Some preliminaries results are presented. Numerical and experimental results achieved with the novel approach proposed and relative to different multilayer biological tissues affected by plane angioma are illustrated and compared. In the conclusions of the chapter, some set of laser parameters optimized for treatment of specific clinical situations are proposed.

The experimental research activity has been made in collaboration with the Department of Dermatology of the University II Policlinico in Naples, monitoring patients in the laser therpay and photodynamics ambulatory. The data analysis and imaging elaboration have been done in the LIRT of the Cibernetic Institute of CNR “E. Caianiello” in Pozzuoli (Na), which funded my grant, under the supervision of Dr. P. Mormile and in collaboration with Dr. L. Petti to whom go my most sincere thanks.

In addition I also want to thank Dr. A. Baldo and Dr. G. Monfregola of the Department of Dermatology of the University II Policlinico for their availability, support and courtesy.

Chapter 1

LASER – BIOLOGICAL TISSUE INTERACTION

1.1 Introduction

In this chapter, it will be discussed basic phenomena occurring when matter is exposed to light. Matter can act on electromagnetic radiation in manifold ways. When a light beam is incident on a slice of matter, in principle, three effects exist which may modify its propagation [1-4]:

- reflection and refraction
- absorption
- scattering

In medical laser applications, however, refraction plays a significant role only when irradiating transparent media (corneal tissue). In opaque media, it is, usually, difficult to measure the effect of refraction due to absorption and scattering. According to the type of material and the incident wavelength, we can have a predominance of either losses or reflection, absorption or scattering. The optical parameters as the refractive index, the absorption and scattering coefficient depend on the wavelength of the incident light. In particular, the index of refractive strongly depends on wavelength in spectral regions of high absorption for the tissue only.

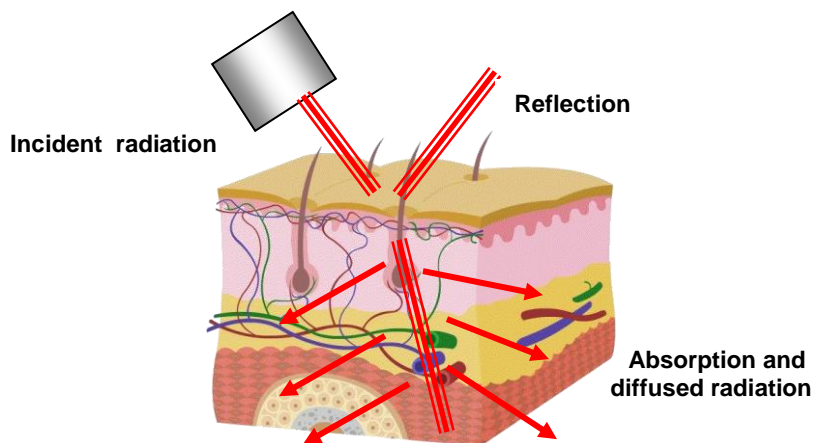


Fig 1.1 : *Geometry of reflection, refraction, absorption and diffused radiation*

1.2 Reflection and refraction of the tissue

In laser surgery, knowledge of absorbing and scattering properties of a selected tissue is essential in order of predicting a successful treatment. In reality, of course, limitations are given by the inhomogeneity of biological tissue which are also responsible for our inability to provide more than mean parameters of the tissues.

Reflection is defined as the returning of electromagnetic radiation by surfaces upon which it is incident. In general, a reflecting surface is the physical boundary between two materials of different indices of refraction such as air and tissue. The simple law of reflection states that the reflection angle θ' equals the angle of incidence θ , expressed by:

$$\theta = \theta' \quad 1.1$$

In contrast, when the roughness of the reflecting surface is comparable or even larger than the wavelength of radiation, diffuse reflection occurs. Diffuse reflection is a common phenomenon of all tissues, since none of them is a highly polished surface such as an optical mirror.

Refraction occurs when the reflecting surface separates two media of different indices of refraction (i.e. n_1 and n_2). The mathematical relation governing refraction is known as *Snell's law* :

$$n_1 \sin \theta_1 = n_2 \sin \theta_2 \quad 1.2$$

When $\sin \theta_1 > n_2 / n_1$ the relation (1.2) is not fulfilled and a total reflection occurs.

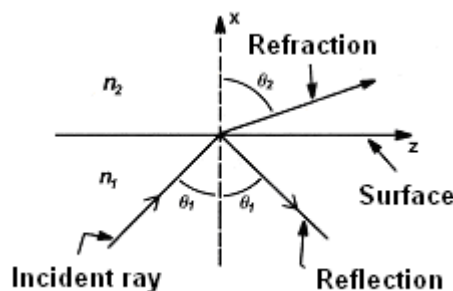


Fig. 1.2: Geometry of light propagation

1.3 Absorption of the biological tissue

Absorption is due to a partial conversion of light energy into heat motion of vibrations of molecules of the absorbing material. A perfectly transparent medium permits the passage of light without any absorption. Among biological tissue cornea and lens can be considered as being highly transparent for visible light. In contrast, media in which incident radiation is reduced practically to zero are called opaque.

The terms “transparent” and “opaque” are relative, since they are wavelength dependent. Actually, no tissue is known to be either transparent or opaque to all wavelengths of the electromagnetic spectrum.

The law that describes the effect of thickness on absorption is called Lambert-Beer law and is expressed by:

$$I(z) = I_0 \exp(-\alpha z) \quad 1.3$$

where z denotes the optical axis, $I(z)$ is the intensity at a distance z , I_0 is the incident intensity, α is the absorption coefficient of the medium. The inverse of the absorption coefficient α is also referred to as the absorption length L

$$L=1/\alpha \quad 1.4$$

The absorption length measures the distance z in which the intensity $I(z)$ has dropped to $1/e$ of its incident value I_0 .

In biological tissues, absorption is mainly caused by either water molecules or macromolecules such as proteins and pigments. Whereas absorption in the IR region of the spectrum can be primarily attributed to water molecules, proteins as well as pigments mainly absorb in the UV and visible range of the spectrum.

In fig 1.3, absorption spectra of two elementary biological absorbers are shown. They belong to melanin and hemoglobin (HbO_2), respectively.

Melanin is the basic pigment of skin and is by far the most important epidermal chromophore. Its absorption coefficient monotonically increases across the visible spectrum toward the UV. Haemoglobin is predominant in vascularized tissues. It has relative absorption peaks around

280 nm, 420 nm, 540 nm and 580 nm, and then exhibits a cut-off at approximately 600 nm. Since the green and yellow wavelengths of Argon and Krypton ion laser perfectly match the absorption peaks of haemoglobin, these lasers can be used for the coagulation of blood and blood vessels. For some clinical applications, dye lasers may be an alternative choice since their tunability can be advantageously used to match particular absorption bands of specific proteins and pigments (selective absorption).

Since neither macromolecules nor water strongly absorb in the near IR, a therapeutic window for many pathologies is delineated between roughly 600 nm and 1200 nm. In this range, radiation penetrates biological tissues at lower loss, thus enabling treatment of deeper tissue structures.

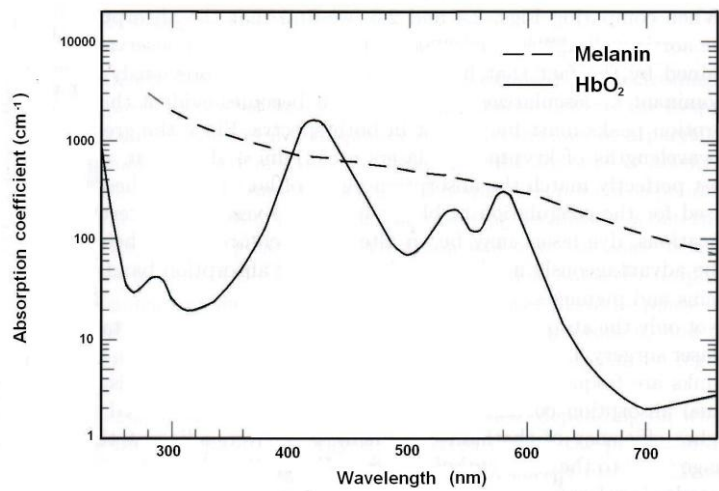


Fig. 1.3: Absorption spectra of melanin in skin and haemoglobin (HbO₂) in blood

1.4 Scattering

Scattering is a class of phenomena by which particles are deflected by collisions with other particles. In particular, it takes place when charged particles are exposed to electromagnetic waves of frequencies not corresponding to those natural frequency of free vibration of the same particles (resonance frequencies). Scattering can be elastic or inelastic, depending on whether part of the incident photon energy is converted during the process of scattering. Elastic scattering occurs when incident and scattered photons have the same energy. A special kind of elastic scattering is Rayleigh scattering. Its only restriction is that the scattering particles are smaller than the wavelength of the incident radiation. In particular, it's possible to find a relationship between scattered intensity and refraction index. This statement is also known as Rayleigh's law and is given by:

$$I_s \approx \frac{(n-1)^2}{\lambda^4} \quad 1.5$$

If the scattering angle θ is taken into account, a more detailed analysis yields

$$I_s \approx \frac{1 + \cos(\theta)}{\lambda^4} \quad 1.6$$

where $\theta=0$ denotes forward scattering. Rayleigh's law is illustrated in fig. 1.4

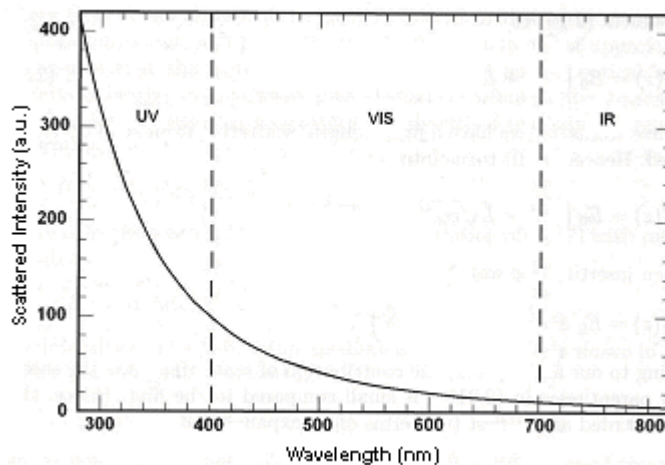


Fig. 1.4: Rayleigh's law of scattering in three different regions

Within the visible spectrum, scattering is significantly reduced when we shift from blue to red light. In the derivation of Rayleigh's law, (1.5) and (1.6), absorption has been neglected. Therefore the relations given are valid only for wavelengths far away from any absorption band. If the size of the scattering particles becomes comparable to the wavelength of the incident radiation, such as in the blood cells, Rayleigh scattering no longer applies and another type of scattering called Mie scattering occurs. The theory of Mie scattering is rather complex and will not be repeated here. However, it is well known that Mie scattering and Rayleigh scattering differ in two important aspects. First, Mie scattering shows a weaker dependence on wavelength ($\sim\lambda^{-x}$ with $0.4 \leq x \leq 0.5$) compared to Rayleigh scattering ($\sim\lambda^{-4}$). Second, Mie scattering preferably takes place in the forward direction, whereas Rayleigh scattering is proportional to $1+\cos^2(\theta)$ according to (1.6), i.e. forward and backward scattered intensities are the same.

In most biological tissues, it was found by Wilson and Adam (1983), Jacques et al. (1987), and Parsa et al. (1989) that photons are preferably scattered in the forward direction. This phenomenon cannot be explained by Rayleigh scattering. On the other hand, the observed wavelength dependence is somewhat stronger than that predicted by Mie scattering. Thus, neither Rayleigh scattering nor Mie scattering completely describe scattering in tissues. Therefore, it is very convenient to define a probability function $p(\theta)$ of a photon to be scattered by an angle θ which can be fitted to the experimental data. When $p(\theta)$ does not depend on θ , the scattering is isotropic. Otherwise, anisotropic scattering occurs.

A measure of the anisotropy of scattering is given by the coefficient of anisotropy g , where $g = 1$ denotes purely forward scattering, $g = -1$ purely backward scattering, and $g = 0$ isotropic scattering. In polar coordinates, the coefficient g is defined by

$$g = \frac{\int_{4\pi} p(\theta) \cos(\theta) d\omega}{\int_{4\pi} p(\theta) d\omega} \quad 1.7$$

where $p(\theta)$ is a probability function and $d\omega = \sin(\theta)d\theta d\phi$ is the elementary solid angle. By definition, the coefficient of anisotropy g represents the average value of the cosine of the scattering angle θ . As a good approximation, it can be assumed that g ranges from 0.7 to 0.99 for most biological tissues. Hence the corresponding scattering angles are most frequently between 8° and 45° .

The important term in 1.7 is the probability function $p(\theta)$, also called *phase function*. Several theoretical phase function $p(\theta)$ have been proposed in literature in order to find the best accordance with experimental observation. More detailed information on these phase functions are provided in the references [5-8].

1.5 Turbid media

In the previous two sections, we have considered the occurrences of either absorption or scattering. In most tissue both of them are present simultaneously. Such media are called turbid media. Their total attenuation coefficient can be expressed by

$$\alpha_t = \alpha + \alpha_s \quad 1.8$$

In turbid media, the mean free optical path of incident photons is thus determined by

$$L_t = \frac{1}{\alpha_t} = \frac{1}{\alpha + \alpha_s} \quad 1.9$$

Only in some cases either α or α_s may be negligible with respect to each other, but it is important to realize the existence of both processes and the fact that usually both are operating. It is very convenient to define an additional parameter, the optical albedo a , by

$$a = \frac{\alpha_s}{\alpha_t} \quad 1.10$$

For $a = 0$, attenuation is exclusively due to absorption, whereas in the case of $a = 1$ only scattering occurs. For $a = 0.5$, the relation (1.10) can be turned into the equality $\alpha = \alpha_s$. In general, both effects will take place but they will occur in variable ratios.

In fig. 1.4 it is shown the albedo as a function of the scattering coefficient. Three different absorption coefficient are assumed which are typical of biological tissue. For $\alpha_s \gg \alpha$, the albedo asymptotically approaches unity.

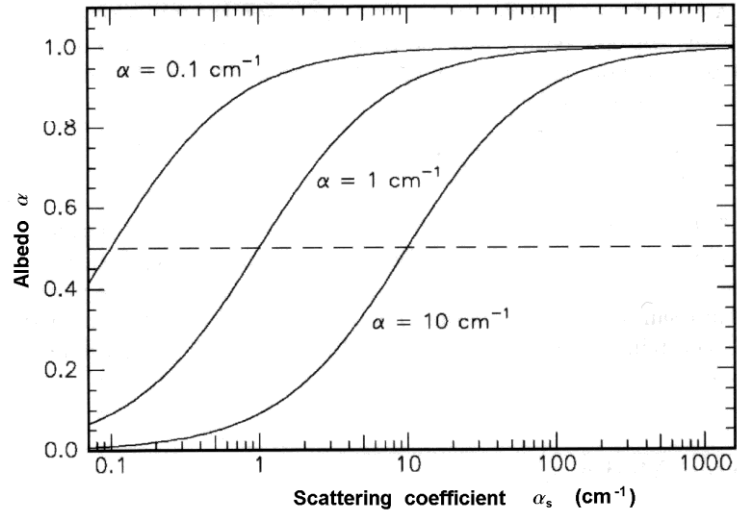


Fig. 1.5: Optical albedo as a function of scattering coefficient

In literature, reduced scattering and attenuation coefficient are often used and are given by

$$\alpha_s' = \alpha_s(1 - g) \tag{1.11}$$

and

$$\alpha_t' = \alpha + \alpha_s' \tag{1.12}$$

since forward scattering alone, i.e. $g = 1$, would not lead to an attenuation of intensity.

1.6 Laser-Tissue: Interaction Mechanisms

The interaction mechanisms that may occur when applying laser light to biological tissue are manifold. Specific laser characteristics as well as laser parameters contribute to this diversity. Most important among optical tissue properties are the coefficients of reflection, absorption, scattering and others such as heat conduction and heat capacity. All together, they determine the total transmission of the tissue at certain wavelengths. On the other hand, the following parameters are given by the laser radiation itself: wavelength, exposure time, energy density and spot size. Among these, the exposure time is a very crucial parameter when selecting a certain type of interaction.

Although the number of possible combinations for the experimental parameters is unlimited, five main categories of interaction types are classified today : photochemical interaction, thermal interaction, photoablation, plasma-induced ablation and photodisruption. All these different interaction types share a single common issue: the characteristic energy density ranges from approximately 1 to 1000 J/cm² . On the other hand, the parameter that distinguishes and controls these processes is the exposure time. A map with the five basic interaction types is shown in fig. 1.6

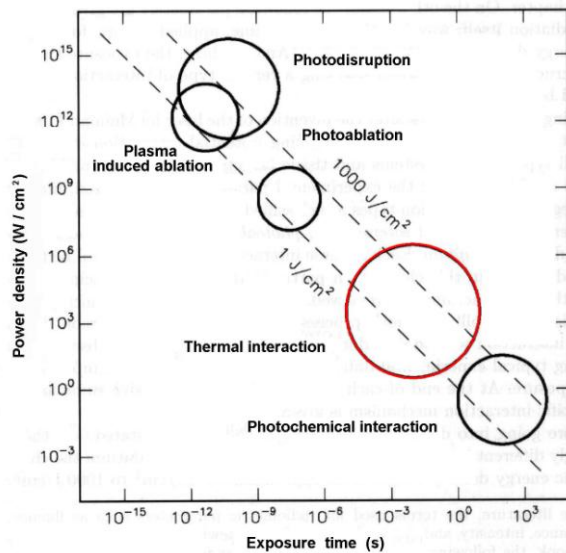


Fig. 1.6: Map of laser tissue interaction

The y axis expresses the applied power density in W/cm² and the exposure time in seconds is reported on the x axis. According to this map, the time scale can be roughly divided into five

sections: continuous wave or exposure times more than 1 s for photochemical interaction, from 1 s to 1 μ s for thermal interaction, from 1 μ s to 1 ns for photoablation, and less than 1 ns for plasma-induced ablation and photodisruption. The difference between the latter two is attributed to different energy densities.

The reciprocal correlation between power density and exposure time clearly demonstrates that roughly the same energy density is required for any type of interaction. Thus, the exposure time appears to be the main parameter responsible for the variety of interaction mechanisms. Anyway, adjacent interaction types present in the map cannot always be strictly separated. For instance, thermal effects may also play an important role during photochemical interaction. In the next sections each of these interaction mechanisms will be briefly discussed whereas a greatest attention will be given to the description of the thermal interaction mechanism which is core of the present thesis work.

1.6.1 Thermal Interaction

The thermal interaction term stands for a large group of interaction types, where the increase in local temperature induces the significant parameter change. Thermal effects can be induced by either CW or pulsed laser radiation. Depending on the duration and peak value of the tissue temperature achieved, different effects like coagulation, vaporization, carbonization, and melting may be distinguished :

- *Coagulation*: during the process of coagulation, temperature reaches at least 60°C, and coagulation tissue becomes necrotic.
- *Vaporization*: It is a thermomechanical effect due to the pressure build-up involved. This effect is attributed to the rich presence of water molecules in the tissues. Water, in fact, strongly absorbs to different wavelength in the NIR region (i.e. 2.94 μ m). If a laser with one of these wavelengths is used (i.e. Er:YAG) a higher pressure in the tissue is induced (water tries to expand in volume as it vaporizes) and this produce localized microexplosions. The resulting ablation is called thermal decomposition
- *Carbonization*: At temperature over 100°C, the tissue starts to carbonize. For medical laser applications, carbonization should be avoided in any case, since tissue already becomes necrotic at lower temperatures. Thus, carbonization only reduces visibility during surgery.

- *Melting*: They originate from thermal stress induced by a local temperature gradient across the tissue surface.

Temperature, obviously, is the governing parameter of all thermal laser-tissue interactions. At the microscopic level, thermal effect have their origin in bulk absorption occurring in molecular vibration-rotation bands followed by nonradiative decay. The reaction can be considered as a two step process. First, absorption of a photon with an energy $h\nu$ promotes the molecule to an excited state A^* , and second, inelastic collision with some partner of the surrounding medium lead to a deactivation of A^* and a simultaneous increase in the kinetic energy M . Therefore, the temperature rise microscopically originates from the transfer of photon energy to kinetic energy. This two step process can be written as

- absorption $A + h\nu \rightarrow A^*$
- deactivation $A^* + M(E_{kin}) \rightarrow A + M(E_{kin} + \Delta E_{kin})$

Both these steps are highly efficient provided that the duration of laser exposure is properly selected. In biological tissues, absorption is mainly due to the presence of free water molecules, proteins, pigments, and other macromolecules and it is governed by Lambert-Beer law. The absorption coefficient strongly depends on the wavelength of the incident laser radiation. In thermal interactions, absorption by water molecules plays a significant role. Therefore, the absorption spectrum of water, an important constituent of most tissues, is shown in the next figure

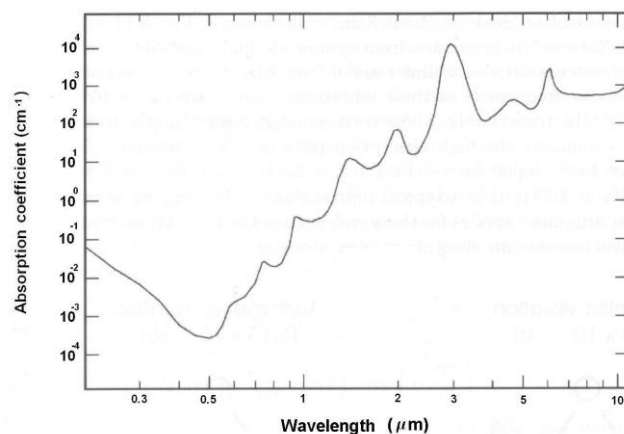


Fig. 1.7: Absorption of water

As it is possible to see the absorption of water is extremely small in the visible range while in the IR range water molecules are the dominant absorbers. In this last region absorption originates from the presence of resonance frequencies associated to symmetric and asymmetric vibrational modes of water molecules. Typical absorption coefficients α and the corresponding absorption length L for the most important laser wavelengths are summarized in table 1.1. The great attenuation in the UV region is strongly enhanced by Rayleigh scattering.

Wavelength (nm)	Laser type	α (cm ⁻¹)	L (cm)
193	ArF	0.1	10
248	KrF	0.018	55
308	XeCl	0.0058	170
351	XeF	0.0023	430
514	Argon ion	0.00029	3400
633	He-Ne	0.0029	340
694	Ruby	0.0056	180
800	Diode	0.020	50
1053	Nd:YLF	0.57	1.7
1064	Nd:YAG	0.61	1.6
2120	Ho:YAG	36	0.028
2940	Er:YAG	12000	0.00008
10600	CO ₂	860	0.001

Tab 1.1: Absorption coefficients α and absorption length L of water at different wavelength

- Heat Generation

Heat generation is determined by laser parameters and optical tissue properties. We assume that a slab of tissue in air is illuminated by Gaussian-shaped laser beam as illustrated in fig. 1.8.

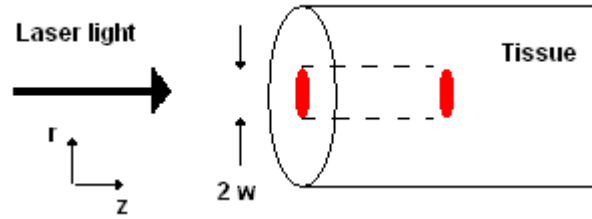


Fig. 1.8: Geometry of the tissue irradiation

For the sake of simplicity, a cylindrical geometry is chosen with z denoting the optical axis, and r the distance from this axis. Then, the amplitude of the electric field and the corresponding intensity inside the tissue are given by

$$\begin{aligned} E(r, z, t) &= E_0 \exp\left(-\frac{r^2}{\omega^2} - \frac{\alpha z}{2}\right) \exp\left(-\frac{4t^2}{\tau^2}\right) \\ I(r, z, t) &= I_0 \exp\left(-\frac{2r^2}{\omega^2} - \alpha z\right) \exp\left(-\frac{8t^2}{\tau^2}\right) \end{aligned} \quad 1.13$$

where E_0 and I_0 are the incident values of electric field and intensity, respectively, ω is the beam waist, α is the absorption coefficient, and τ is the pulse duration. The incident values E_0 and I_0 are related to each other by the basic electrodynamic equation

$$I_0 = \frac{1}{2} \varepsilon_0 c E_0^2 \quad 1.14$$

where ε_0 is the dielectric constant, and c is the speed of light.

By means of the two-step process as described above, heat is generated inside the tissue during the laser exposure. Deposition of heat in tissue is due only to light that is absorbed in the tissue.

For a light flux in the z -direction in a nonscattering medium, the local heat deposition per unit area and time in a thickness Δz is given by

$$S(r, z, t) = \frac{I(r, z, t) - I(r, z + \Delta z, t)}{\Delta z} \quad 1.15$$

And, as Δz approaches zero, we have that

$$S(r, z, t) = -\frac{\partial I(r, z, t)}{\partial z} \quad 1.16$$

Therefore, under all circumstances, heat deposition is determined by

$$S(r, z, t) = \alpha I(r, z, t) \quad 1.17$$

Thus, the local heat source $S(r, z, t)$ inside the exposed tissue is a function of the absorption coefficient α and the local Intensity $I(r, z, t)$. Since α is strongly wavelength-dependent, the same applies for S . If phase transitions or tissue alterations do not occur, an alteration in heat content dQ induces a linear change in temperature dT according to the basic law of thermodynamics

$$dQ = mcdT \quad 1.18$$

where m is the mass, and c is the specific heat capacity. For most tissues a good approximation is given by

$$c = (1.55 + 2.8 \frac{\varphi_w}{\varphi}) \quad 1.19$$

where φ is the tissue density and φ_w is its water content expressed in Kg/m^3

- Heat Effects

Approximate values of achievable temperatures can often be estimated. The thermal interactions dealing with biological effects are related to different temperatures inside the tissue. As already stated, these can be manifold, depending on the type of tissue alterations.

Assuming a body temperature of 37°C , no measurable effects are observed for the next 5°C above this. The first mechanism by which tissue is thermally affected can be attributed to conformational changes of molecules. These effects, accompanied by bond destruction and membrane alterations, are summarized in the single term hyperthermia ranging from approximately $42\text{-}50^{\circ}\text{C}$. If such a hyperthermia lasts for several minutes, a significant percentage of the tissue will undergo necrosis as described below by Arrhenius' equation. Beyond 50°C , a measurable reduction in enzyme activity is observed, resulting in reduced energy transfer within the cell and immobility of the cell. Furthermore, certain repair mechanisms of the cell are disabled. Thereby, the fraction of surviving cells is further reduced.

At 60°C , denaturation of proteins and collagen occurs which leads to coagulation of tissue and necrosis of cells. The corresponding macroscopic response is the visible paling of the tissue. At even higher temperatures more than 80°C the membrane permeability is drastically increased, thereby destroying the otherwise maintained equilibrium of chemical concentrations.

At 100°C , water molecules contained in most tissues start to vaporize. The large vaporization heat of water (2253 KJ/Kg) is advantageous, since the vapor generated carries away excess heat and helps to prevent any further increase in the temperature of adjacent tissues. Due to the large increase in volume during this phase transition, gas bubbles are formed inducing mechanical ruptures and thermal decomposition of tissue fragments. Only if all water molecules have been vaporized, and laser exposure is still continuing, does the increase in temperature proceed. At temperatures exceeding 100°C , carbonization takes place which is observable by the blackening of adjacent tissues and the escape of smoke. To avoid carbonization, the tissue is usually cooled down with either water or gas. Finally, beyond 300°C , melting can occur, depending on the target material.

All these steps are summarized in table 1.2, where the local temperature and the associated tissue effects are listed

Temperature (°C)	Biological effect
43 - 45	- Conformational alteration - Shrinkage of the tissue - Hyperthermia
45 - 60	- Alteration of enzymatic activity - Cell immobility
60 - 75	- Protein denaturation - Coagulation
75 - 100	- Collagen denaturation - Permeabilization of membranes
100	- Vaporization - Thermal decomposition (ablation)
>100	- Carbonization - Formation and breaking of vacuols
>300	- Thermoablation of the tissue

Tab. 1.2 : *Thermal effects of laser radiation*

However, it was observed that not only the temperature achieved but also the temporal duration of this temperature plays a significant role for the induction of irreversible damage. It is illustrated in fig. 1.9 how the critical temperature and the corresponding temporal duration relate to each other if irreversible damage is meant to occur. The curve is derived from several empirical observation.

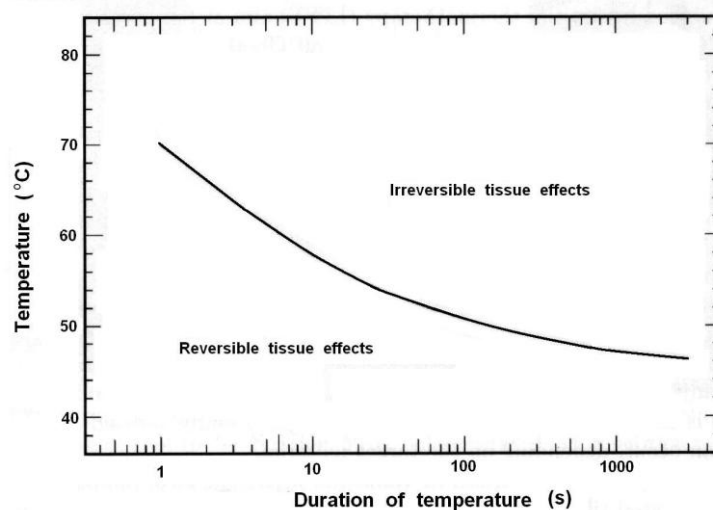


Fig. 1.9: *Critical temperature for the occurrence of cell necrosis*

Areas in which the temperature reaches values higher than 60°C are coagulated and irradiated tissue cells become necrotic. Areas with maximum temperatures less than 60°C are treated hyperthermally only, and the probability of cells staying alive depends on the duration and temporal evolution of the temperature obtained. For a quantitative approximation of both the remaining active molecules and cells at certain temperature level, Arrhenius' equation is very useful

$$\ln \frac{C(t)}{C_0} = -A \int_0^t \exp\left(-\frac{\Delta E}{RT(t')}\right) dt' \equiv -\Omega \quad 1.20$$

where C_0 is the initial concentration of molecules or cells, $C(t)$ is the concentration at a time t , A is Arrhenius' constant, R is the universal gas constant, and ΔE and Ω are specific tissue properties.

The local degree of tissue damage is determined by the damage integral given by (1.20). The damage degree is defined as the fraction of deactivated molecules or cells given by

$$D_d(t) = \frac{C_0 - C(t)}{C_0} = 1 - \exp(-\Omega) \quad 1.21$$

Thus, by inserting an appropriate value of the tissue constant Ω , we are able to calculate the probable damage degree $D_d(t)$ as a function of time (t). Unfortunately, experimental data for the two parameters A and ΔE are very difficult to be obtained due to the inhomogeneity of most tissues and the uncertainty in measuring the surviving fraction. However in literature [9-13] some values of various tissues are given as the result of different studies.

Laser radiation acts thermally if power densities more than 10 W/cm² are applied from either CW radiation or pulse durations exceeding approximately 1 μ s. Typical lasers for coagulation are Nd:YAG lasers, Dye lasers and diode lasers. CO₂ lasers are very suitable for vaporization and the precise thermal cutting of tissues. Carbonization and melting can occur with almost any type of laser if sufficient power densities and exposure durations are provided.

Frequently, not only one but several thermal effects are induced in biological tissues, depending on the laser parameters. These effects might even range from carbonization at the tissue surface to hyperthermia a few millimeters inside the tissue.

Since the critical temperature for cell necrosis is determined by the exposure time, no well-defined temperature can be declared which distinguishes reversible from irreversible effects. Thus, exposure energy, exposure volume, and exposure duration all together determine the degree and extent of tissue damages. Therefore, careful evaluation of the required laser parameters is essential. The concomitance of several thermal processes is illustrated in fig. 1.20. The location and spatial extent of each thermal effect depend on the locally achieved temperature during and after laser exposure.

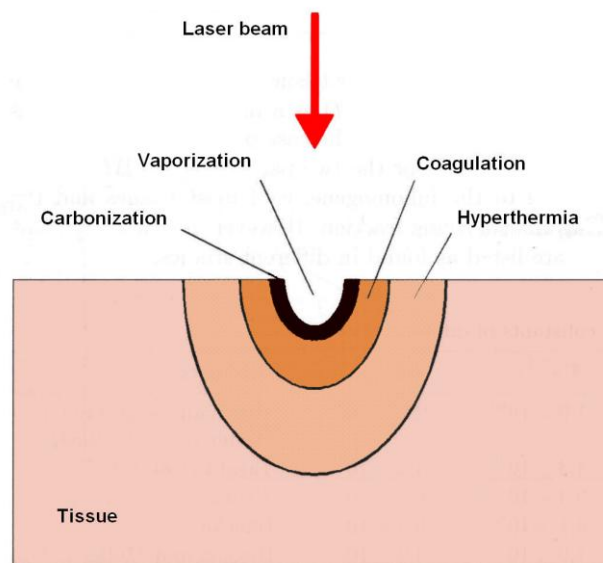


Fig. 1.20: Location of thermal effects inside biological tissue

1.6.2 Photochemical Interaction

Photochemical interactions are based on empirical observations stating that light can induce chemical effects and reactions within macromolecules or tissues. These interactions take place at very low power densities (typically 1 W/cm^2) and long exposure times ranging from pulses of seconds to continuous waves. Careful selection of laser parameters yields a radiation distribution inside the tissue that is determined by scattering. In most cases, wavelengths in the visible range (e.g. Rhodamine dye lasers at 630 nm) are used because of their efficiency and their high optical penetration depths. The latter are of importance if deeper tissue structures are to be reached.

In the field of medical laser physics, photochemical interaction mechanisms play a significant role during photodynamic therapy (PDT). Frequently, biostimulation is also attributed to photochemical interactions, although this is not scientifically ascertained.

- **Photodynamic therapy (PDT)**

During PDT, spectrally adapted chromophores are injected into the body. Monochromatic irradiation may then trigger selective photochemical reactions, resulting in certain biological transformations. A chromophore compound which is capable of causing light-induced reactions in other non-absorbing molecules is called a photosensitizer. After resonant excitation by laser irradiation, the photosensitizer performs several simultaneous or sequential decays which result in intramolecular transfer reactions. At the end of these diverse reaction channels, highly cytotoxic reactands are released causing an irreversible oxidation of essential cell structures.

- **Biostimulation**

Biostimulation is believed to occur at very low irradiances and to belong to the group of photochemical interactions. Unfortunately, the term biostimulation has not been scientifically very well defined, so far. The potential effects of extremely low laser powers (1-5mW) on biological tissues have been a subject of controversy, since they were first claimed by the Hungarian surgeon Mester at the end of the 1960s. Wound healing and anti-inflammatory properties by red or near infrared light sources such as helium-neon lasers or diode lasers were

reported. Typical energy fluences lie in the range 1-10 J/cm² .

In several cases, researchers have noticed improvements in the patients. But in a few studies only, results could be verified by independent research groups. Moreover, contradictory results were obtained in many experiments. However, only very few patients were treated, and no clinical protocols were established. Furthermore, the success is rather doubtful, since In many of these diseases 50 % of the patients are spontaneously cured even without any treatment. According to Wilder-smith (1988), the distinction from an ordinary “placebo” effect is thus rather difficult to be verified.

According to Karu (1987), local wound healing effects with helium-neon or diode lasers may be explained by the action of low-intensity light on o proliferation. In the area of such injuries, conditions are usually create preventing proliferation such as low oxygen concentration or pH. The exposure to red or near infrared light might thus serve as a stimulus to increase cell proliferation. When irradiating fresh wounds the effect of biostimulation is found to be minimal or even nonexistent. This observation is probably due to the fact that cell proliferation is very active in fresh wounds, and regeneration is not significantly altered by laser irradiation. However, biostimulation is a research field with a lot of speculation involved. Usually, the controversy stems from our inability to specify the photochemical channels of potential reactions. Detailed investigations in this area and reproducible experimental results are badly needed.

1.6.3 Photoablation

Photoablation is a laser-tissue interaction where the biological tissue is decomposed when exposed to high intense laser irradiation. With this effect a direct breaking of molecular bonds by high-energy (UV) photons is obtained. Typical threshold values of this type of interaction are 10⁷-10⁸ W/cm² at laser pulse durations in the nanosecond range. The ablation depth (which defines the depth of tissue removal per pulse) is determined by the pulse energy up to a certain saturation limit. The geometry of the ablation pattern itself is defined by the spatial parameters of the laser beam. The main advantages of this ablation technique lie in the precision of the etching process, its excellent predictability, and the lack of thermal damage to adjacent tissue. Today, in medical applications, photoablation is one of the most successful techniques for refractive corneal surgery, in which the refractive power of the cornea is altered in myopia,

hyperopia or astigmatism.

In order to obtain a physical explanation of the photoablation process, let us assume that two atoms A and B are bound by a common electron. The character of the bonds within an organic material is primarily covalent. The corresponding energy level diagram of the ground and several excited states is shown in fig. 1.21

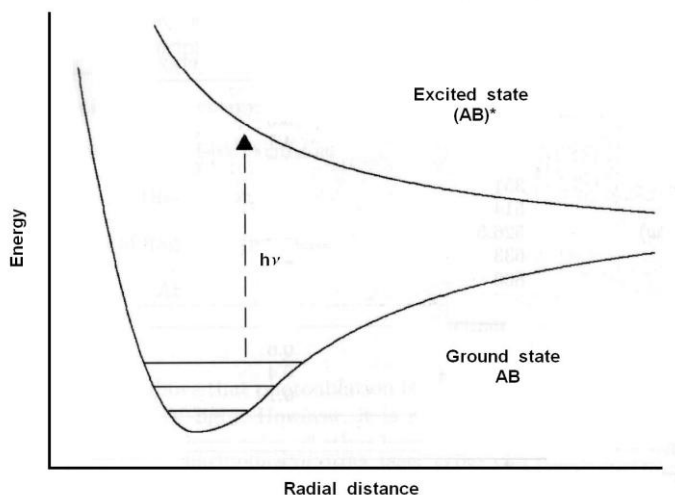


Fig. 1.21: Energy level diagram for photoablation

Due to the macromolecular structure, each electronic level is split into further vibrational states. Absorption of a photon may promote the two atoms to an excited state (AB)*. Usually, the excitation is achieved by satisfying the Franck-Condon principle. It states that the radial distance of the two nuclei of the atoms A and B will not be affected during the process of excitation due to the small electron mass. Thus, transitions characterized by a vertical line in the energy level diagram are favored. The probability of such transition is increased if the maxima of the corresponding Schrödinger function of the initial and final states coincide at the same radial distance.

If a UV photon is absorbed, the energy gain is usually high enough to access an electronic state which exceeds the bond energy. In this case, the two atoms A and B may dissociate at the very next vibration. Thus, photoablation can be summarised as a two-step process :

- excitation: $AB + h\nu \rightarrow (AB)^*$
- dissociation: $(AB)^* \rightarrow A + B + E_k$

The dissociation energies of some typical chemical bonds, the wavelengths and the corresponding photon energies of selected laser systems are given in the following tables:

Type of bond	Dissociation energy (eV)
C=O	7.1
C=C	6.4
O-H	4.8
N-H	4.1
C-O	3.6
C-C	3.6
S-H	3.5
C-N	3.0
C-S	2.7

Tab. 1.3 : *Dissociation energies of some chemical bound*

Laser type	Wavelength (nm)	Photon energy (eV)
ArF	193	6.4
KrF	248	5.0
XeCl	308	4.0
XeF	351	3.5
Argon ion	514	2.4
Dye - Rhodamine	595	2.2
He-Ne	633	2.0
Diode	800	1.6
Nd:YAG	1064	1.2
Er:YAG	2940	0.4
CO ₂	10600	0.1

Tab. 1.4: *Laser systems used in medical applications*

When comparing both tables, we find that only photons from UV lasers, typically excimer lasers, provide an energy sufficient for dissociating such bonds. Therefore, the interactions mechanism of photoablation is limited to the application of UV light.

However, it was observed that a certain threshold intensity must be applied to achieve photoablation. Above this intensity, a well-defined depth is ablated, depending on the absorption coefficient and the incident intensity. If the incident Intensity is moderate and such that the ablation depth is smaller than the corresponding optical absorption length, subsequent pulses will enter partially irradiated tissues as well as unexposed tissues. Therefore, only the first few pulses are unique. After these a linear relation between the number of applied pulses and the total etch depth is obtained. In practice, the etch depths are averaged over several pulses and noted as ablation depth per pulse. This value is reproducible within an uncertainty of about 10% for most materials which is an excellent value when taking all the inhomogeneities of tissues into account.

1.6.4 Plasma-induced Ablation

When obtaining power densities exceeding 10^{11} W/cm² in solids and fluids a phenomenon called *optical breakdown* occurs. As result of a *optical breakdown* a plasma-induced ablation phenomenon can occur. Sometimes, plasma-induced ablation is also referred to as plasma-mediated ablation [14-16]. Plasma-induced ablation permit an ablation of the tissue by ionizing plasma formation. By means of plasma-induced ablation, very clean and well-defined removal of tissue without evidence of thermal or mechanical damage can be achieved.

The most important parameter of plasma-induced ablation is the local electric field strength E which determines when optical breakdown is achieved. If E exceeds a certain threshold value, for instance, if the applied electric field forces the ionization of molecules and atoms, breakdown occurs. The electric field strength itself is related to the local power density I by the basic electrodynamic equation

$$I_0 = \frac{1}{2} \varepsilon_0 c E_0^2 \quad 1.22$$

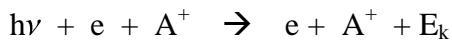
where ε_0 is the dielectric constant, and c is the speed of light. For picosecond pulses, typical threshold intensities of optical breakdown are 10^{11} W/cm². Hence the corresponding electric field amounts to approximately 10^7 V/cm. This value is comparable to the average atomic or intramolecular Coulomb electric fields, thus providing the necessary condition for plasma ionization. Within a few hundred of picoseconds, a very large free electron density with typical value of 10^{18} /cm³ is created in the focal volume of the laser beam. In general, plasma generation due to an intense electric field is called *dielectric breakdown*. The term *optical breakdown* especially emphasises that UV, visible and IR light are strongly absorbed by the plasma. The physical principles of breakdown have been investigated in several theoretical studies [17-22].

The initiation of plasma generation can be two-fold [23]. It was observed that either Q-switched pulses in the picosecond or femtosecond range can induce a localized microplasma. In Q-switched pulses, the initial process for the generation of free electrons is supposed to be thermoionic emission. In mode locked pulses, multi-photon ionization may occur due to the high electric field induced by the intense laser pulse.

In general, the term multi-photon ionization denotes processes in which coherent absorption of

several photons provides the energy needed for ionization. Due to the requirement of coherence, multi-photon ionization is achievable only during high peak intensities as in picosecond or femtosecond laser pulses. Plasma energies and plasma temperatures are usually higher in Q-switched laser pulses because of the associated increase in threshold energy of plasma formation. Thus, optical breakdown achieved with nanosecond pulses is often accompanied by nonionizing side effects.

In either case, however, a few "lucky" electrons initiate an avalanche effect, leading the accumulation of free electrons and ions. A free electron absorbs a photon and accelerates. The accelerated electron collides with another atom and ionizes it resulting in two free electrons. Each of them will have less individual kinetic energy than the initial electron. Again, these free electrons may absorb incoming photons, accelerate, strike other atoms, release two more electrons, and so forth. The basic process of photon absorption and electron acceleration taking place in the presence of an atom is called *inverse Bremsstrahlung*. It is based on a free-free absorption, for instance, a transition where a free electron is present in the initial and final states. In order to fulfill the conservation laws of energy and momentum, this event must necessarily take place in the electric field of an ion A^+ or a neutral atom. The process is schematically represented as :



In particular, the important feature of optical breakdown is that it renders possible an energy deposition not only in pigmented tissue but also in nominally weakly absorbing media. This is due to the increased absorption coefficient of the induced plasma. Thereby, the field of potential medical laser applications is considerably widened. Especially in ophthalmology, transparent tissues - like cornea and lens - become potential targets of laser surgery. It is also worthwhile noting that during the process there is no restriction of the photon energy involved. The electron may increase its kinetic energy by means of absorbing any amount of energy, thus leading to a very short risetime of the free electron density of the order of picoseconds. In order to achieve optical breakdown the irradiance must be intense enough to cause rapid ionization so that losses do not quench the electron avalanche. According to Smith and Haught (1966), inelastic collisions and diffusion of free electrons from the focal volume are the main loss mechanisms during avalanche ionization.

1.6.5 Photodisruption

Photodisruption effect consist on the fragmentation and cutting of tissues by mechanical forces . In general, the physical effects associated with optical breakdown are *plasma formation* and *shock wave generation*. If breakdown occurs inside soft tissues or fluid, *cavitation* and *jet formation* may additionally take place.

Cavitation is an effect that occurs when focusing the laser beam not on the surface of a tissue but into the tissue. By means of the high plasma temperature, the focal volume is vaporized and a bubble, typically made of water vapor and carbon oxides, is formed. As a result of the outer static pressure, the boubble implodes determining a permanent tissue damage.

Jet formation occur when cavitation bubble collapse in the vicinity of a solid boundary. In this case, a high speed liquid jet directed toward the wall is produced. if the bubble is in direct contact with the solid boundary during its collapse, the jet can cause high-impact pressure against the wall resulting in a severe damage and erosion of tissue. Thus, consequent to jet formation phenomenon, bubbles attached to solids have the largest damage potential.

When discussing plasma-induced ablation, any secondary effects of the plasma have been neglected. At higher pulse energies, and thus higher plasma energy, shock waves and other mechanical side effects become more significant and might even determine the globe effect upon the tissue. Primarily, this is due to the fact that mechanical effects scale linearly with the absorbed energy. Then, because of the mechanical impact, the term *photodisruption* is more appropriate.

During photodisruption, the tissue is split by mechanical forces. Whereas plasma-induced ablation is spatially confined to the breakdown region, shock wave and cavitation effects propagate into adjacent tissues, thus limiting the localizability of the interaction zone. For pulse durations in the nanosecond range, the spatial extent of the mechanical effects is already of the order of millimeters even at the very threshold of breakdown. Actually, purely plasma-induced ablation is not observed for nanosecond pulses, because the threshold energy density of optical breakdown is higher compared to picosecond pulses, and the pressure gradient scales with plasma energy.

Hence, for nanosecond pulses, optical breakdown is always associated with shock wave formation even at the very threshold. Since adjacent tissues can be damaged by disruptive forces, the presence of these effects is often an undesired but associated symptom. In contrast, picosecond or femtosecond pulses permit the generation of high peak intensities with

considerably lower pulse energies. With these extremely short pulse durations, optical breakdown may still be achieved with significantly reducing plasma energy and, thus, disruptive effects. Moreover, spatial confinement and predictability of the laser-tissue interaction is strongly enhanced. Since both interaction mechanisms, plasma-induced ablation as well as photodisruption, rely on plasma generation, it is not always easy to distinguish between these two processes. Actually, in the 1970s and 1980s, all tissue effects evoked by ultrashort laser pulses were attributed to photodisruption. It was only because of recent research that a differentiation between ablations solely due to ionization and ablations owing to mechanical forces seems justified.

In general, photodisruption may be regarded as a multi-cause mechanical effect starting with optical breakdown. In fig. 1.22, a schematic sequence of these processes is illustrated indicating their relations to each other. Moreover, the distinction between photodisruption and plasma-induced ablation is emphasized

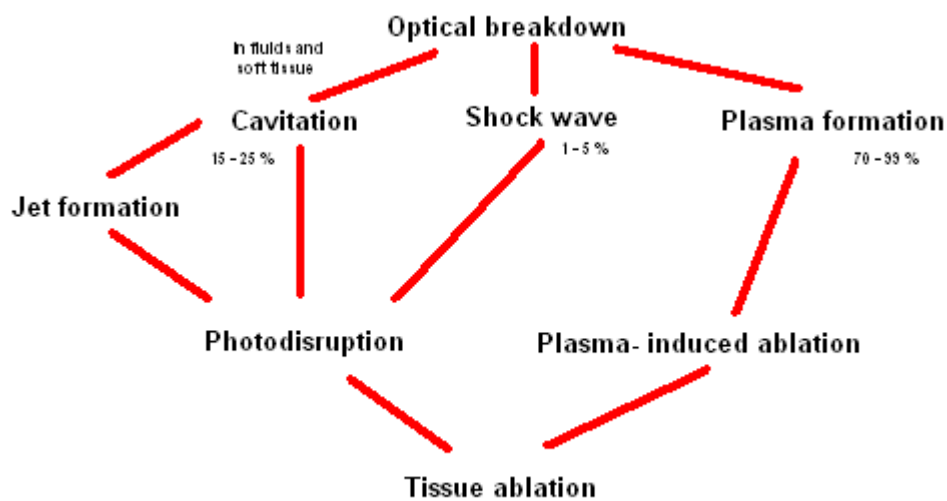


Fig. 1.22: Scheme of the physical process associated with optical breakdown. Percentages given are rough estimates of the approximate energy transferred to each effect

The four effects, plasma formation, shock wave generation, cavitation, and jet formation, all take place at a different time scale. Plasma formation begins during the laser pulse and lasts for a few nanoseconds afterwards. This basically is the time needed by the free electrons to diffuse into the surrounding medium. Shock wave generation is associated with the expansion of the plasma and, thus, already starts during plasma formation. However, the shock wave then

propagates into adjacent tissue and leaves the focal volume. Approximately 30-50 ns later, it has slowed down to an ordinary acoustic wave.

Cavitation, finally, is a macroscopic effect starting roughly 50-150 ns after the laser pulse. The time delay is caused by the material during the process of vaporization. Usually, the cavitation bubble performs several oscillations of expansion and collapses within a period of a few hundred microseconds. Since the pressure inside the bubble again increases during collapse, each rebound of the cavitation bubble is accompanied by another shock wave. Furthermore, every collapse can induce a jet formation if the bubble is generated in the vicinity of a solid boundary.

Photodisruption has become a well-established tool of minimally invasive surgery (MIS), since it was introduced by Krasnov (1973) and then further investigated by Aron-Rosa et al (1980) and Fankhauser et al (1981) [24-26]. Two of the most important applications of photodisruptive interaction are posterior capsulotomy of the lens, frequently being necessary after cataract surgery, and laser-induced lithotripsy of urinary calculi.

1.7 Laser Applications in the medical field

Since their first appearance, lasers have found numerous applications in the field of medicine. The first medical application of lasers dates back to 1962, when a ruby laser was used for reattachment of the retina in the eye. It was the invention of the CO₂ laser in 1967 with its high absorption by water that opened up the vast field of surgical applications.

After 1974, the availability of optic fibers permitted the combination of laser technology with endoscopy. In table 1.4 the most used laser systems in medical applications are listed.

The high absorption rate in water, hemoglobin, and melanin guarantees efficient clinical applications with optimal medical results.

Nowadays, the development of new technologies and the increasing understanding of the utilization of that technology by the medical community have brought a continuous increase of laser use in a wide range of medical applications. Below, some of the principal applications of laser in modern medicine are described .

- Laser in Dermatology

In dermatology, thermal effects of laser radiation are commonly used, especially coagulation and vaporization [27, 28]. Since the optical parameter of skin, i.e. absorption and scattering, are strongly wavelength-dependent, various kinds of tissue reaction can be induced by different laser systems. In clinical practice, five types of lasers are currently being used: argon ion lasers, dye lasers, CO₂ lasers, Erbium lasers and Nd:YAG lasers.

Radiation from argon ion laser is strongly absorbed by hemoglobin and melanin. This laser is thus predestined for superficial treatments of highly vascularized skin. One of the most frequent applications of this laser is upon patients with plane angioma pathologies

The first laser to produce selective light induced injury was the pulsed dye laser. This device is used to treat a variety of blood vessel abnormality and, in particular, in the last years is preferred to the argon laser for treatment on port wine stains (plane angiomas). The pulsed dye laser approved by FDA in 1988 has revolutionized the treatment of this disorder and has then been used to treat other disorders of the blood vessel including broken blood vessels on the face, spider veins on the legs, different types of scars and even warts [29-33]. Pigmented laser disorders such as aging spots, café-au-lait spots, brown birthmarks and tattoos are treated by pulsed laser technology [34, 35]. Laser has recently been developed for hair removal by selectively damaging the hair bulb. The most recent development that generated tremendous interests are the use of pulsed CO₂ and Erbium lasers for skin resurfacing. By using short pulses of light that are absorbed by the upper layers of skin, these lasers resurface the skin making it much smoother and restoring it to a more youthful appearance This treatment is effective in rejuvenating skin of patients with wrinkles or other sun-induced damage and also for smoothing the textural change of acne scarring. Compared to chemical peels, laser resurfacing is more precise. The results are more impressive and side effects are no more frequent. These dramatic developments have reshaped the ability to treat skin disorders. Radiation from Nd:YAG lasers is significantly less scattered and absorbed in skin than radiation from the other lasers. The optical penetration depth of Nd:YAG lasers radiation is thus much larger. Hence, major indications for this laser in dermatology are given by deeply located hemangiomas or semimalignant skin tumor.

- Laser in Dentistry

Although dentistry was the second medical discipline (after ophthalmology) where lasers were applied, it basically remains a field of research. Especially in caries therapy (the most frequent dental surgery) conventional mechanical drills are still superior compared to most types of lasers, particularly CW or long-pulse lasers [36, 37]. Only laser systems capable of providing ultrashort pulses might be an alternative to mechanical drills. However, many clinical studies and extensive engineering effort still remain to be done in order to achieve satisfactory results. Recently, studies have established the disturbing link between periodontal disease, heart disease and strokes. Those patients with infected gums and gum diseases suffer twice the heart attack rate and almost triple the stroke rate of those who do suffer from gum infection. The last one is crucial when arterial cardiovascular damage is present in a patient. Pre-surgical laser protocol can help eliminate bacteremia by efficiently addressing buildup of bacterial colonies that cause and sustain periodontal disease in a patient ready to receive open-heart surgery.

- Laser in Otolaryngology

Otolaryngology was one of the first areas in which lasers have been applied. Particularly, the CO₂ laser has found use in the treatment of airway in which precision, homeostasis and lack of swelling are necessary. This allows removal of diseased tissue without compromising the patient's breathing. Carbon dioxide lasers have been used to remove both benign and malignant conditions of the larynx (voice box), pharynx (throat) and oral cavity. Similarly, ND:YAG and KTP lasers can be transmitted through a fiber optic cable to remove growths in the tracheobronchial tree as well as esophagus. These two wavelengths have been applied to surgery within the nasal passages and sinuses. The CO₂ and Argon laser have been used to treat otologic disorders such as otosclerosis. The precision afforded allows delicate removal of bone tissue and replacement with artificial prosthesis to improve hearing. Currently otolaryngologists are at the forefront of using various imaging modalities to view laser tissue interaction deep within the head and neck to afford greater therapy precision in the care of patients.

- Laser in Urology

Various types of lasers are utilized to successfully treat a number of diseases on the urinary and genital systems [38]. The more common diseases include: urinary stones, urothelial tumors, obstructions due to narrowing of ureteropelvic junction, ureteral structure, benign enlargement of the prostate urethral structures, benign condylomas and superficial cancer of the penis. Majority of such treatments require general anesthesia but can be performed as an outpatient basis with little or no blood loss and excellent results.

- Laser in Podiatry

Many conditions treated by laser include: fungal nails, ingrown nails, deformed nails, matrixectomies, granulomas, porokeratosis, hemangiomas, pigmented villonodular, synovitis, neurofibromatosis, periungual fibromas, remodeling hypertrophic scars/keloids, adjunct ulcer therapy (like debridement), plantar warts, skin fissures, tumors, various types of cysts including foreign body cysts, incision and excision of neuromas and release of sublesional hematomas.

- Laser in Ophthalmology

In ophthalmology, various types of lasers are being applied today for either diagnostic or therapeutic purpose [39, 40]. However, lasers have three main applications in ophthalmology:

- 1) They are used to treat glaucoma, a group of diseases caused by increased pressure in the eye.
- 2) Refractive surgeons use excimer lasers to reshape the cornea and help the eye focus properly.

Laser vision correction to treat near-sightedness, farsightedness and astigmatism

- 3) Retina specialists use lasers (argon or ruby lasers) to treat macular degeneration.

The procedure combines a light activated drug with a low-power red light to destroy abnormal blood vessels.

- Lasers in Neuro-surgery

Microsurgical lasers are used for precision cutting, for making incisions into the brain and spinal cord producing discrete results for the relief of pain. The CO₂, KTP and ND:YAG are used frequently in the vaporization and coagulation of tumors, particularly, if located intracranially or deep within the brain. The use of laser has been particularly beneficial for very narrow approaches that are required to access tumors in these locations. Fiber-optically delivered lasers are being more frequently used for the vaporization and shrinkage of spinal discs to treat patients with herniated discs within the upper, mid and lowerback through minimally invasive surgical approach using the endoscopic guidance.

Chapter 2

INFRARED IMAGING: Principles and applications

2.1 Introduction

Among the different non-destructive techniques that are in use nowadays, Infrared Thermography (IT) stands as an attractive tool for non-contact inspections [41, 42].

It is one among the numerous techniques used to “*see the unseen*”. As the name implies, it uses the distribution (*suffix –graphy*) of surface temperatures (*prefix thermo-*) to assess the structure or behavior of what is under the surface.

Infrared Thermography is a contactless imaging technique with distinct advantages.

It is based on the recording of the natural thermal radiation emission of a body by employing an infrared camera. The result is the temperature distribution of the body’s surface under investigation. By analysis and images elaboration it is possible to achieve information about the condition of surface and subsurface structure of the sample such as:

- Homogeneity degree
- Individuation and characterization of anomalies
- Monitoring of the sample under external heating

In general infrared technique can be deployed in two different experimental approaches depending on the specific application: passive and active method.

Passive thermography is based on the detection of the infrared images under natural conditions without an external stimulation. In *active thermography* a sequence of infrared images is detected during or after application of an external thermal stimulation.

Distinctions between the passive and active approaches are not as sharp as it seems. For example, although maintenance investigation of buildings is generally considered as a passive thermography application, it can be performed by the active approach as well. As it is known, water in a wall activates undesired chemical reactions in building and thus a degradation process. In the case of monumental buildings, due to the extremely high cost of restoration, it is first necessary to assess the moisture problem. This can be done by heating the wall uniformly

from one side while observing the isotherm pattern on the other side. The thermal map recorded depends on the water content since the heat capacity is higher for water than for dry material. It is interesting to note that moisture evaluation of buildings and roofs in particular has been reported by passive methods as well. In this case, thermographic inspection is performed at night or early in the morning and detection is based on the fact that moist areas retained day sunshine heat better than did sound dry areas because of the high thermal capacity of water. In that case, too, the passive label is debatable since solar heating is a form of external thermal stimulation.

What is generally recognized is that if one does not need thermal stimulation, the procedure is called passive and active otherwise.

In this chapter both approaches are described, focusing the attention on different active procedures. The most important features of infrared detectors are discussed and, finally, the chapter is completed with an overview on the new perspectives of infrared imaging applications in medical science.

2.2 Passive thermography

The first law of thermodynamics concerns with the principle of energy conservation and states that an important quantity of heat is released by any process consuming energy because of the law of entropy. Temperature is thus an essential parameter to measure in order to assess proper operation. In passive thermography, the sample is observed under natural thermal condition while no external thermal perturbation is applied. In this procedure, abnormal temperature profiles indicate a potential problem, and a key term is the temperature shift with respect to a reference, often referred to as the delta-T (ΔT) value or the hot spot. A ΔT value of a few degrees ($> 3\text{ }^{\circ}\text{C}$) is generally suspicious, while higher values indicate strong evidence of abnormal behavior. Applications such as control of industrial processes [43-45], building inspection [46-49], military surveys, welding, fire detection (for example in the forest), and some medical investigation make use of this mode of operation, where surface temperature distribution, as it is, contains relevant information concerning possible disorders, the presence or absence of anomalies, and so on.

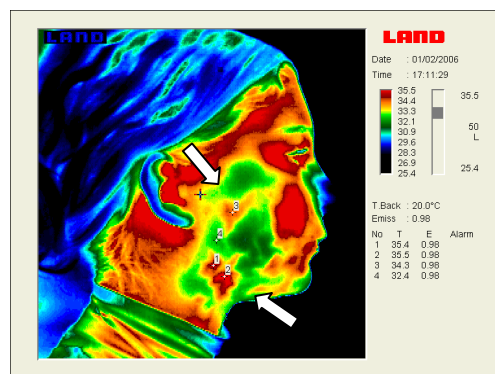


Fig. 2.1: *Passive thermography on a sclerodermic patient: in the image hot spots associated to some morphea plaques are well visible*

Generally, passive thermography is rather qualitative since the goal is simply to individualize anomalies. However, if thermal modeling is available, some investigations provide quantitative measurements, so that measured surface temperature (isotherm) can be related to specific behaviors or subsurface flaws. For instance, such dedicated modeling helps us to understand needle heating during high-speed sewing in the automobile industry. This makes it possible to optimise sewing operations through needle redesign and needle cooling, with significant economic and quality benefits, due to the millions of products sewed daily (seat cushions, airbags, etc...) [50].

2.3 Active thermography : Testing procedures

In active thermography it is necessary to transfer some energy to the specimen inspected in order to obtain significant temperature differences emphasizing the presence of subsurface anomalies.

Defect detection principle, in active thermography, is based on the followed idea:

If a thermal front, travelling inside the sample, meet a dishomogeneous area, its part is reflected behind and modifies the temperature of the surface over the defect

So, from the acquisition of a sequence of superficial images, during and after a thermal stimulation, it is possible, by images elaboration, to obtain information about structural subsurface homogeneity, defect individuation and quantification purposes (inverse problem).

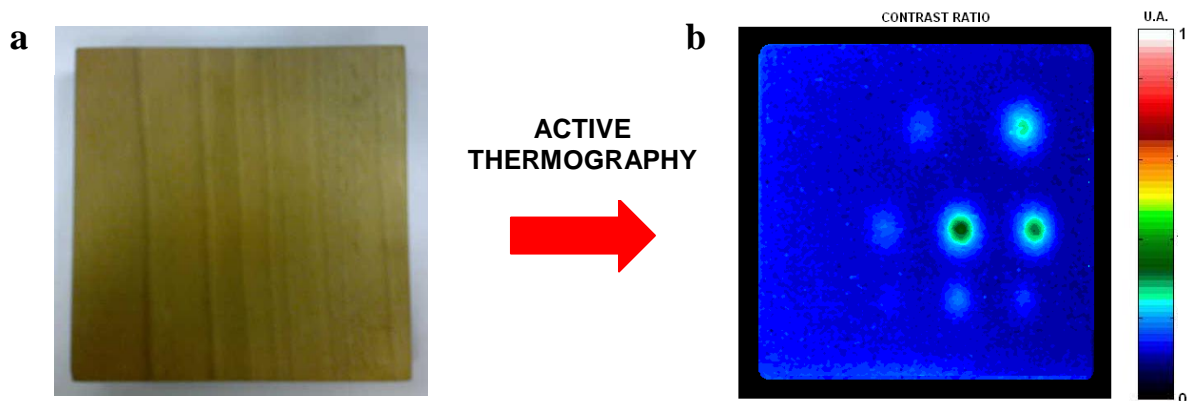


Fig. 2.2: Active thermography applied on a wood specimen: a) visible image of the specimen, b) contrast thermal image obtained after a procedure of pulsed thermography. The thermal contrast image emphasizes the presence of air holes to different depth inside the wood

Hence, contrary to the passive approach, the active approach requires an external appropriate heat source to stimulate the materials for inspection.

This is a crucial aspect since lack of success in active thermography applications is often related to problems with the thermal stimulation device, such as the lack of homogeneity of the heating source. In pulsed thermography, when step heating is used to reveal subsurface defects, it is necessary to generate a thermal transient inside the part. Such a thermal transient can be

generated as either a static or a mobile configuration. Such a thermal stimulation can be either hot (hotter than the sample) or cold (cooler than the sample) since a thermal front propagates in the same way in both situations. The cold approach has, under certain circumstances, several advantages over the warm approach: for example, when the part to be inspected is already hot, like the external part of a curing oven in the case of graphite-epoxy panels. In these cases, it is uneconomical adding extra heat to the part, while cooling is more economical. Another benefit is that a cool thermal stimulating device will not generate any thermal noise since it is at a reduced temperature with respect to the component to be inspected. Such a cool thermal perturbation device can be deployed using :

- Cool water jets
- Cool air/gas jets
- Snow or ice (with contact)
- Cool water bag (with contact)

More traditionally, a hot thermal perturbation is used, which can be:

- High-powered cinematographic lamps
- Sequence of quartz infrared line lamps
- High-powered photographic flashes
- laser beam (Scanned or single beam)
- Heat gun, hot water jets, hot air jets, hot water bag

The main desirable characteristics of the thermal perturbation (either cool or warm) is repeatability, uniformity, timeliness, and duration.

Repeatability is needed in order to compare among results obtained on many identical parts. It is worthwhile to notice that lamp aging can reduce power deposit significantly: up to 40% of light intensity can be lost due to the deposition of evaporated tungsten from the filament on the inner lamp glass envelope.

Uniformity is necessary when inspection is performed on wide surfaces. Dishomogeneous thermal stimulation will produce spurious hot (cold) spots, which may be interpreted as subsurface flaws (especially in the case of the pulsed scheme, described below). This uniformity characteristic is hard to achieve. However, specific deconvolution algorithms,

specific calibration and contrast computations can allow for stimulation correction after its application.

For the pulsed scheme, *timeliness* and *duration* are other important issues for thermal stimulation. In this case, in fact, for a better agreement with theoretical models and to enable data inversion, a square thermal pulse is needed. In order to optimize this parameter a mechanical shutter may be used in front of the thermal perturbation device for the start-stop of the pulse. Nowadays, several active thermographic techniques exist differing from each other mainly in the way data is acquired and/or processed as reviewed and discussed briefly below. In this description more emphasis is given to the presentation of the *pulsed thermography* method because part of the experimental procedure used in this thesis work (described in the next chapters) make use of this active technique.

2.3.1 Pulsed Thermography

Pulsed thermography (PT) is one of the most common thermal stimulation methods used in infrared imaging [51-62]. One reason for this is how fast is the inspection, during which a short thermal stimulation pulse lasting from a few milliseconds for high-conductivity material (such as metal) to a few seconds for low-conductivity samples (such as plastics, wood, graphite-epoxy laminates) is used. Basically, PT consists of a fast heating of the sample under investigation and then recording the temperature decay curve. Qualitatively, the phenomenon can be described in the following. The temperature of the material changes rapidly after the initial thermal pulse because the thermal front propagates by diffusion under the surface and also because of radiation and convection losses. The presence of a subsurface defect modifies the diffusion rate. Thus when observing the surface temperature, a different temperature with respect to the surrounding sound area appears over a sub-surface defect once the thermal front has reached it. Consequently, deeper defects will be observed later and with reduced contrast. In fact, the observation time t is a function (in a first approximation) of the square of the depth z [63] and the loss of contrast c is inversely proportional to the cube of the depth [64]

$$t \approx \frac{z^2}{\alpha} \quad c \approx \frac{1}{z^3} \quad 2.1$$

where α is the thermal diffusivity of the material. These relations (2.1) show two limitations of PT : observable defects will generally be shallow and the contrast weaks.

A well known empirical rule says that: *the radius of the smallest detectable defect should be at least one to two times larger than its depth under the surface* [65].

In general, there are two different operation way in PT. The sample is heated from one side while thermal data is collected either from the same side (*i.e.* **reflection mode**) or from the opposite side (*i.e.* **transmission mode**) (Fig. 2.3).

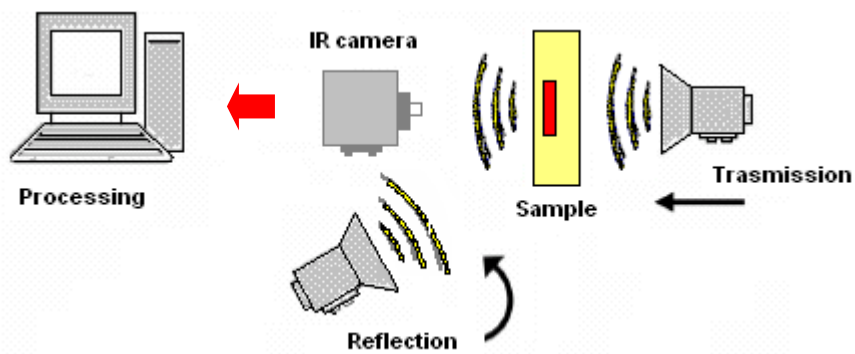


Fig. 2.3: Pulsed Thermography set-up: reflection and trasmission mode

Reflection is used when inspecting defects closer to the heated surface, whilst transmission is preferred for detecting defects closer to the non-heated surface (*i.e.* deeper defects). In general, reflection is most used because resolution is higher than trasmission mode and it is easier to be employed since both sides of the sample do not need to be available. Although deeper defects can be detected in transmission, depth information is loss since thermal waves will travel the same distance whether their strength is reduced by the presence of a defect or not. Hence, depth quantification is not possible in transmission.

Defective zones will appear at higher or lower temperature with respect to nondefective zones on the surface, depending on the thermal properties of both the material and the defect.

It is now interesting to make the link with thermal wave theory. Mathematically, a pulse can be decomposed into a multitude of individual sinusoidal components. In that respect, pulse heating of a sample corresponds to the simultaneous launching into the sample of thermal waves of various amplitudes and frequencies, in a transient mode. Utilization of a thermal pulse for stimulation of the sample is thus practical since thermal waves of many different frequencies are tested simultaneously (the flat frequency spectrum of a Dirac pulse).

The detection phenomenon in PT is illustrated in Fig. 2.4

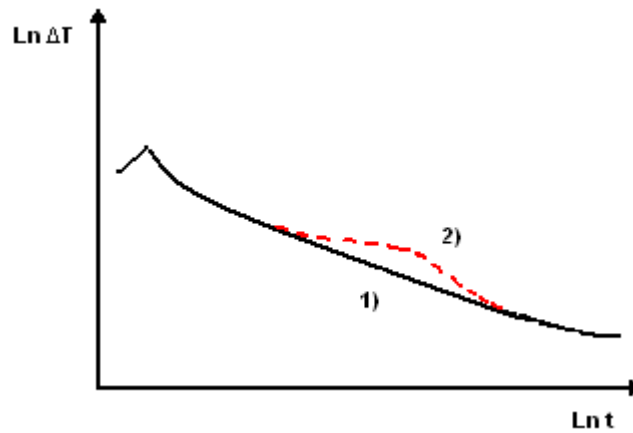


Fig. 2.4: *Temperature evolution curve after absorption of a rectangular pulse: 1) sample made of homogeneous material; 2) sample containing a subsurface flaw*

the surface temperature evolution following the application of the initial heat pulse is plotted for a thin homogeneous plate (curve 1) and for the same plate when a delamination (air layer) is present under the surface (curve 2). In the logarithmic scale we notice that the central portion of the temperature decay follows a slope of $-1/2$. In fact, for a semi-infinite medium, after absorption of a Dirac pulse, this temperature decay conforms to [66]

$$\Delta T = \frac{Q}{e_f \sqrt{\pi t}} \quad 2.2$$

where ΔT is the temperature increase of the surface, Q the quantity of energy absorbed, and $e_f = (k\rho C)^{1/2}$ is the thermal effusivity of the material, with k being the thermal conductivity, ρ the mass density, C the specific heat, and t the time, respectively.

In PT the short heating employed prevents damage to the component. Heating is generally limited to a few degrees above the initial sample temperature. Obviously, the stimulation source must be nondestructive and thus it must not damage the inspected surface either chemically or physically: this will limit its strength. This can be an issue when high-intensity pulses are employed, especially when high-intensity heating is directed on delicate surfaces (e.g. frescoes, paintings of old Masters).

It is worthwhile to notice that a cold front (heat removal) will propagate in the same way as a hot front (heat deposit) inside the material. In some inspection situations, this cold approach is cheaper: for instance, in case of the inspection of a component already at a high temperature (with respect to ambient temperature) due to the manufactured process such as for the curing of bonded parts. Moreover, it may be attractive to preheat (if necessary) the surface with a low rate of energy deposition (e.g. by means of electric heating wires). This approach avoids relying on high-intensity local heat sources, which are more costly, susceptible to rapid aging, and potentially dangerous for the surface because of the high thermal stress they induce. Cold thermal sources are also advantageous since they do not generate thermal reflective noise, which can perturb the measurement.

As for the detection depth this is limited since thermography is a border technique. Anyway the anomalies (such as cracks, etc) usually start close to the surface.

In the next section more information about a complete thermogram sequence are given. The study of the temporal temperature profile is the core in the data-elaboration in the pulsed thermography method. This is, in fact, the basis for defect detection in active thermography as described next.

2.3.1.1 The complete thermogram sequence

In pulsed thermography each infrared images sequence recorded, before and after external thermal stimulation, can be analyzed pixel to pixel. The temporal evolution associated to every pixel follows a rate that can be separated in different step.

In general, the complete thermal temporal sequence for a single pixel is composed of 5 distinctive elements depicted in fig. 2.5. At time t_0 , which defines the time immediately before heat reaches the sample's surface, a *cold image* (1) is captured. The cold image can be used to eliminate spurious reflections due to emissivity variations and to reduce fixed pattern artifacts. This is attractive for thermal data visualization and quantification although it is less useful when working with phase delay images. During (and shortly after) the application of a heat pulse, the acquired thermograms are temperature saturated (2), *i.e.* the reading is out of the calibration scale and no accurate measure can be computed. The actual number of saturated thermograms depends on the sampling frequency and on the thermal properties of the material

under inspection: low conductivity materials saturates longer than high conductivity materials, thus more thermograms, saturated or not, will be recorded using high sampling rates. Saturated thermograms give no valuable information and therefore can be safely discarded from the processing stage.

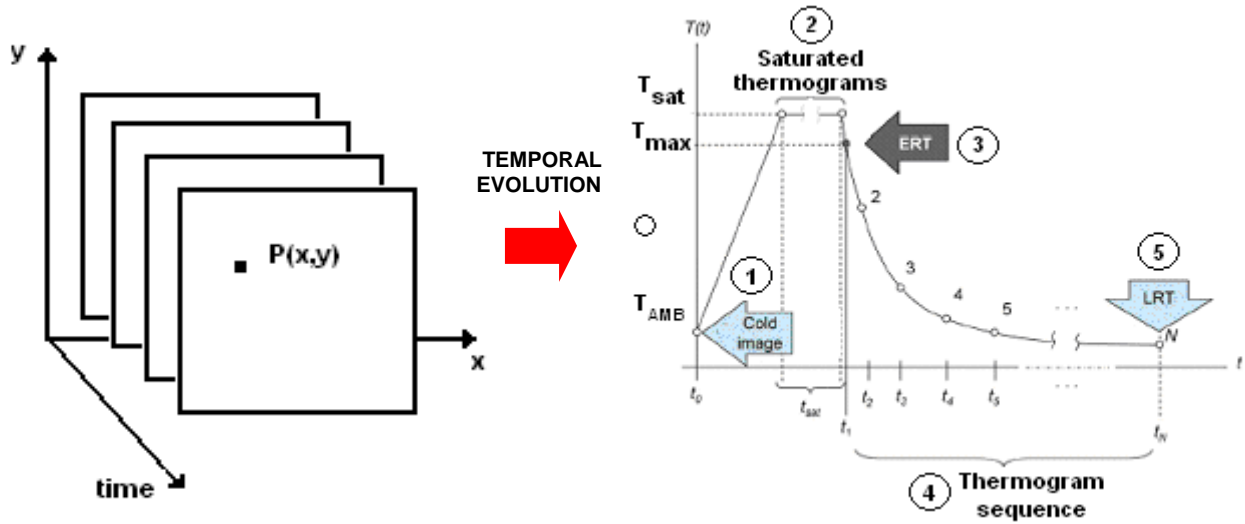


Fig. 2.5 : Complete thermogram sequence of a single pixel: 1- cold image, 2- saturated thermograms, 3- ERT-Early Recorded Thermogram, 4- thermogram sequence and 5- LRT- Last Recorded Thermogram

The first useful thermogram that comes into sight after saturation is known as the *Early Recorded Thermogram* (ERT) (3). Ideally, defects are still not visible on the ERT. Anyhow, this condition is not always encountered in practice, especially when inspecting shallow defects on high conductivity materials using low sampling frequencies and/or when strong non-uniform heating is present. Normally, this situation does not constitute a problem for defect detection purposes. However, since depth is a function of time ($z \sim t^{1/2}$ [42]), special care must be taken in order to perform quantitative analysis. Starting at the ERT at t_1 , all subsequent thermograms are of interest for defect inspection and constitute the thermogram sequence (4). The last acquired image at t_N (5) corresponds to the *Last Recorded Thermogram* (LRT). From this point, temperature variations are considered negligible. Deviation from the $t_{1/2}$ dependency on the useful part of the thermogram provides an indication of the presence of a defective area (see fig. 2.4). In order to obtain information about the presence of anomalies or defects an important parameter obtainable from an infrared sequence is the thermal contrast (ΔT). There are different definitions of thermal contrast in literature, the most used of them are described in the next section .

2.3.1.2 Definitions of thermal contrast

Several inversion procedures for defect characterization, (*i.e.* determination of the size, depth and thermal resistance of a defect, or for the evaluation of surface coatings) make use of normalized thermal contrast as an input signal. During real experiments, the thermal contrast is quite corrupted by non-uniform heating, non-uniform emissivity and absorption distributions of the inspected sample. There are some classical definitions for the thermal contrast which are acknowledged to be quite effective in reducing the effects of non uniform heating and non uniform optical properties [67, 68]. Each contrast definition is applied depending on the situation. In the following these definitions are presented. Then, at the end of the section, a definition of a newer contrast, the DAC contrast, that is reference-independent and very effective in reducing non-uniform heating effects, is given [69, 70].

- Contrast for the transmission mode

After the absorption of the heating energy by the front surface of the sample, heat diffusion within the material yields thermograms (temperature T versus time t curves) whose qualitative shapes for the rear surface are shown in Fig. 2.6 . $T_{SA}(t)$ is the thermogram in a sane area. while $T(t)$ is the thermogram in a defective area. The temperature in the defective area shows a slower increase than in the sane area. The difference of the two thermograms leads to the thermal contrast on the rear surface ΔT_{TRANS} .

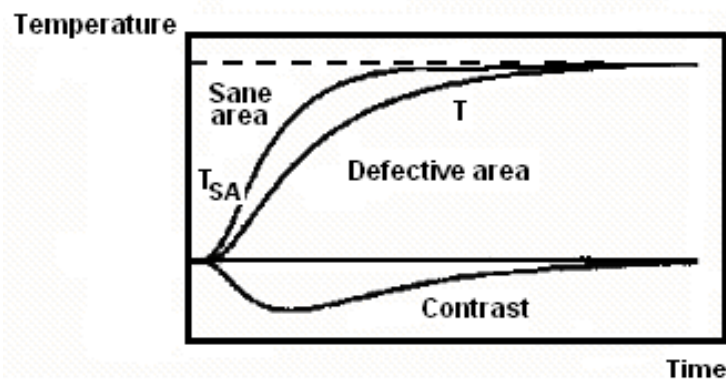


Fig. 2.6 : Temperature and contrast for the transmission mode

The curves in fig. 2.6 correspond to a theoretical case of uniform heating and adiabatic heat transfer assumption. In real life, heating is non uniform and specimens are subject to heat losses, which yields thermograms on both sane and defective areas showing distinct maxima. To overcome the effect of non uniform heating, a classical definition of the contrast [67] suggests to determine the contrast by first normalizing each thermogram on its peak value, then to calculate the difference between the two normalized thermograms, which leads to:

$$\Delta T = \frac{T}{T_{MAX}} - \frac{T_{SA}}{T_{SA,MAX}} \quad 2.3$$

where Sa = Sane area and MAX = maximum of thermogram. During the processing of the infrared sequences obtained from the PT experiments, eq. 2.3 is performed for each pixel of the images. The local normalization aspect of each thermogram used in eq. 2.3 yields an effective attenuation of the non uniformity of the heating.

- Contrast-for the reflection mode

After the heat excitation, heat diffusion within the material yields thermograms whose qualitative shapes for the front surface are shown in fig. 2.7. $T_{SA}(t)$ is the thermogram in a sane area, while $T(t)$ is the thermogram in a defective area. We can see that the defective area shows a slower decrease than the sane area. The difference of the two thermograms leads to the thermal contrast on the front surface ΔT_{REF}

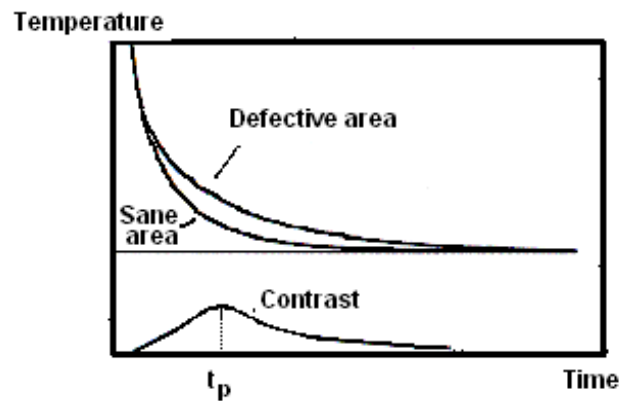


Fig. 2.7 : Temperature and contrast for the reflection mode

Similarly to the transmission case, there is a definition of a locally normalized contrast. Such a definition is convenient for the reflection mode when a stabilization temperature is attained (e.g. high conductivity materials). The curves shown in fig. 2.7 are obtained under the assumption of uniform heating and negligible heat losses. In real experiments, heating is not uniform which leads to different asymptotic levels for both defective and sane area thermograms. To reduce the effect of non uniform heating, each thermogram is normalized on its asymptotic level, and then the difference between the two normalized thermograms is determined, which leads to

$$\Delta T_{LONG} = \frac{T}{T_{LRT}} - \frac{T_{SA}}{T_{SALRT}} \quad 2.4$$

where LONG = normalization at long times, Sa = Sane area and LRT = last recorded temperature. For poor heat conductor materials, the asymptotic level at the end of the thermograms as shown in fig. 2.7 does not exist, and eq. (2.4) cannot be used. In such situations, the asymptotic adiabatic temperature can be evaluated from the thermograms at a short time (i.e. just after the flash heating). Indeed, the thermograms at those short times follow the modelling of a semi-infinite sane medium. If we denote as T_{ERT} the temperature recorded immediately after the flash heating at time t_S of the first frame, for example, we have :

$$T_{\infty} = T_{ERT} (\pi t_{SF})^{1/2} \quad 2.5$$

where t_{SF} is the Fourier number corresponding to time t_S (i.e. $t_{SF} = a_Z t_S / e^2$, where a_Z is the thermal conductivity in the z direction). The evaluation of the asymptotic level $T_{0\infty}$ for the sane area is performed the same way starting from temperature T_{OS} at time t_S . The locally normalized contrast for each pixel can therefore be calculated by :

$$\Delta T_{SHORT} = \frac{1}{\sqrt{\pi t_{SF}}} \left(\frac{T}{T_{ERT}} - \frac{T_{SA}}{T_{SA,ERT}} \right) \quad 2.6$$

Where SHORT = normalization at short times, Sa = Sane area and LRT = early recorded temperature. ΔT_{SHORT} is convenient for the reflection mode when the thermal profiles do not reach stabilization (e.g. low conductivity materials and/or short acquisition times).

- Differential Absolute Contrast (DAC)

In the last two sections it has been presented the thermal contrast definitions for the transmission and the reflection modes (for long and short times), respectively. Although the impact of non-uniform heating is minimized through the normalization process, the exact location of a non-defective area is still needed to compute the contrast. It is also possible to use other thermal contrast definitions such as the differential absolute contrast (DAC) which has proved to effectively reduce the effect of non-uniform heating and which does not require the definition of a sane area [69, 70].

The DAC technique is based on the absolute thermal contrast definition:

$$\Delta T(t) = T(t) - T_{SA}(t) \quad 2.7$$

and the 1D solution of the Fourier diffusion equation for a Dirac pulse applied on the surface ($z=0$) of a semi-infinite body, which may be written as follows [66]

$$\Delta T = \frac{Q}{e_f \sqrt{\pi t}} \quad 2.8$$

where $T(t)$ is the temperature evolution, $Q(\text{J/m}^2)$ is the injected energy at the surface, and $e_f = (k\rho C)^{1/2}$ is the thermal effusivity of the sample. The last one is a thermophysical property relevant to transient surface heating processes measuring the material ability to exchange heat with its surroundings.

In the DAC method, instead of looking for a non-defective area, T_{SA} is computed locally assuming that there is no defect visible on the first few images (i.e. it behaves as a sane area). The first step is to define t' as a given time value between the instant when the pulse is launched and the precise time when the first defective spot appears on the thermogram sequence, i.e. when there is enough contrast for the defect to be detected.

At t' , there is no indication of the existence of a defective zone yet, therefore the local temperature for a sane area is exactly the same as for a defective area:

$$T_{SA}(t') = T(t') = \frac{Q}{e_f \sqrt{\pi t'}} \quad \Rightarrow \quad \frac{Q}{e_f} = T(t') \sqrt{\pi t'} \quad 2.9$$

From the above equation, T_{SA} can be computed for every pixel at time t , and substituting it into the absolute contrast definition, eq. 2.7, It follows that :

$$\Delta T_{DAC} = T(t) - \sqrt{\frac{t'}{t}} T(t') \quad 2.10$$

Eq. 2.10 needs to be normalized. This can be done in a similar way as described for the contrast in the reflection mode. The temperature recorded immediately after the flash heating T_{ERT} at time t_S is given by eq. 2.5. From this definition and eq. 2.10, the normalized temperature for a defect is given by :

$$\frac{T(t)}{T_\infty} = \frac{T(t)}{T_{ERT}} \frac{1}{\sqrt{\pi t_{SF}}} \quad 2.11$$

and for a sound area:

$$\frac{T_{SA}(t)}{T_{\infty,SA}} = \frac{\sqrt{\frac{t'}{t}} T(t')}{T_{ERT,SA} \sqrt{\pi t_{SF}}} = \frac{\sqrt{\frac{t'}{t}} T(t')}{\sqrt{\frac{t'}{t_S}} T(t') \sqrt{\pi t_{SF}}} = \sqrt{\frac{t_S}{t}} \frac{1}{\sqrt{\pi t_{SF}}} \quad 2.12$$

From eq. 2.11 and eq. 2.12, we obtain a normalized definition for the DAC contrast:

$$\Delta T_{DACN} = \left[\frac{T(t)}{T_{ERT}(t_S)} - \sqrt{\frac{t_S}{t}} \right] \frac{1}{\sqrt{\pi t_{SF}}} \quad 2.13$$

The DAC method has proven to be very efficient in reducing artifact from non-uniform heating and surface geometry [71]. An interactive step is involved in the process of determining t' , for which semi-automated and fully automated algorithms [70] are available. Research is now moving towards the study of a modified DAC approach. This last technique utilises thermal quadrupoles and the Laplace transform in order to derive a solution that includes the plate thickness.

2.3.2 Step Heating (Long Pulse)

In contrast to the thermal stimulation scheme, for which the temperature decay is of interest, in case of Step Heating the increase in surface temperature is monitored during application of a stepped heating pulse (the sample is continuously heated, at low power). Variations of surface temperature with time are related to sample features as in pulsed thermography. This technique of stepped heating (SH) is sometimes referred to as time-resolved infrared radiometry (TRIR). Although strictly speaking, techniques using pulsed heating could also be considered time-resolved. Time-resolved means that the temperature is monitored as it evolves during and after the heating process. Stepped-heating describes the functional dependence of the heating source. SH has numerous applications, such as for coating thickness evaluation (including multilayered coatings, ceramics), integrity of the coating-substrate, bond determination or evaluation of composite structures and characterization of airframe hidden corrosion, among others. Experimental setup for SH expedients is similar to PT setup (fig.2.3). When SH was developed, only infrared scanners were available. At that time, one of the main advantages of SH was the much faster temporal resolution achievable with respect to full-field imaging at a video rate of about 25 or 30 images/s. This was because in these cases, the vertical mirror of the scanner was stopped so that the device operated only in line scan mode. More recently, thanks to the availability of fast FPA-IR cameras, the technique has been simplified. The start of the heating pulse is triggered with respect to acquisition of infrared images which are recorded sequentially for later processing of the entire heating period. Data processing includes evaluation of the thermal transit time t_T , that is, the time the normalized temperature of a given point in the field

of view differs from the evolution obtained in the case of a thick sound specimen. Transit time t_T is related to defect depth. fig. 2.8 shows the effect of the coating thickness on the sample temperature.

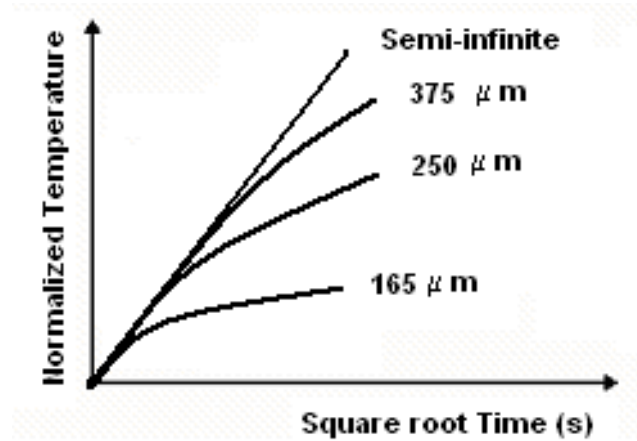


Fig. 2.8: Example of curves temperature versus $t^{1/2}$ for a sample with a coating of different thickness for a step heating pulse of duration 1 s.

Advantages of this approach are that defect depth and thermal properties are accessible from a single measurement without requiring knowledge about a defect-free region (such as to compute the contrast in PT). In fact, the early time, before the manifestation of subsurface defects, allows us to calibrate the image in order to take into account spatial variations of emissivity and reflectivity.

Although from the experimental point of view SP is different than PT, from a mathematical point of view, both procedures provide thermal signals that contain exactly the same information. The choice to rely on PT or SP will thus depend on the applications, and more specifically, on the time scale of the phenomena of interest: slow phenomena are better explored with SH and fast phenomena with PT. In general, let be called Δt_{dist} the period of time required for a given defect to distinguish itself from the background, then the procedure (SH or PT) that enables to put a maximum energy Q in the specimen during Δt_{dist} will produce the largest signal (eq. 2.2). It has been suggested [72] that for a given application, a pulse length slightly smaller than Δt_{dist} can be chosen and the pulse strength can be adjusted so that the maximum surface temperature reached does not damage the specimen. However, other practical criteria, such as limitation of power for continuous sources or limitation in the adjustability of pulse duration for pulsed sources, have to be considered as well.

2.3.3 Lock-in Thermography

Lock-in thermography (LT), sometimes called phototherapy radiometry, is based on thermal waves generated inside a specimen and detected remotely [73-77]. Wave generation, for example, is performed by periodic deposition of heat on a sample's surface (e.g. through sine-modulated lamp heating) while the resulting oscillating temperature field, in the stationary regime, can be recorded remotely through its thermal infrared emission by an IR camera. Lock-in refers to the necessity to monitor the exact time dependence between the output signal and the reference input signal (i.e. the modulated heating). This is done with a locking amplifier in point-by-point laser heating or by computer in full-field employment (lamp) so that both phase and magnitude images become available.

More specifically, measurement of temperature evolution over the specimen surface permits us to reconstruct the thermal wave (travelling inside the sample) and to establish values of A (wave magnitude) and ϕ (phase) from four equidistant temperature data points.

Although four points are enough to compute A and ϕ , more points allow us to reduce noise associated with the process. Computer-based commercial systems of LT (such as the lock-in option of FLIR/CEDIP) works on all available points recorded over one or more modulation cycles. Such a system thus provides three images: phase ϕ , amplitude A , and conventional thermography image T . The thermographic image is a mapping of the thermal infrared power emitted, the phase image is related to the propagation time and the modulation image is related to the thermal diffusivity. Obviously, one of the strong points of LT is the phase image, which is relatively independent of local optical and infrared surface features and hence it is interesting for nondestructive-testing purposes. For example, optical features refer to nonuniform heating, while infrared features may concern with a variable surface emissivity. The depth range of images is inversely proportional to the modulation frequency of the input signal, so that higher modulation frequencies restrict the analysis in a near-surface region.

Applications of LT are numerous and in different fields. For example, interestingly, in addition to photothermal heating, other heating employments are possible for various applications. In case of medicine, analysis of blood circulation was demonstrated [78]. Here, a compression cuff located in the upper arm creates the modulation, enabling us to analyze the blood flow in the forearm: repetitive compression is performed through control of the air pressure going into the cuff. Low frequencies (0.03 and 0.015 Hz) reveal blood vessel visualization down to 3 mm under the skin. This has created interest in visualizing the functionality of the circulatory

system and especially to discover changes related to a developing pathological process.

2.3.4 Vibrothermography

The concept of vibrothermography (VT) originates from the German physicist W. E. Weber (1804-1891), who discovered in 1830 that an increase in length of a material results in a decrease in temperature. Such an idea was later formalized by the English physicists W. Kelvin (1824-1907) in 1853 and J. Joule (1818- 1889) in 1857. Since this effect is reciprocal, a reduction in length causes an increase in temperature. Periodical loading of the material thus generates hot spots at locations of stress concentration.

Vibrothermography was first introduced as an application method in the late 1970's. Researchers observed that as cracks or discontinuities in a solid sample were excited with high energy – low frequency ultrasound, they generated heat and were detectable with an IR camera. Despite this promising start, the technique remained dormant until recently, when techniques known as sonic thermography, or thermosonic testing were introduced. Significant improvements in IR camera performance over the past 20 years have made it possible to detect small cracks using lower excitation energies (or short duration pulses of high energy) than the previous reports suggested. As a result, there has been considerable renewed interest in implementing vibrothermography as a nondestructive crack detection method.

Vibrothermography (VT) is an active infrared imaging technique based on that principle: under the effect of mechanical vibrations induced externally to a structure, thanks to direct conversion from mechanical to thermal energy, heat is released by fraction precisely at locations where defects such as cracks and delaminations are located, making them detectable by an infrared camera.

In the basic scheme for modern vibrothermography-based testing, an acoustic horn is placed in contact with a solid sample, and a brief pulse of acoustic energy in the 10 – 50 kHz range is applied to the sample. Pulse energy is typically in the range of 500 – 3000 Joules, and duration less than a second. The signal generation process in vibrothermography is almost entirely determined by the interaction of the injected sonic energy with the mechanical properties of the sample. The thermal and IR emission characteristics of the sample play a relatively small role. In principle, heating of the sample is minimal unless a crack or some other source of frictional

heating is present. However, in practice, there is often significant localized heating at the sonic insertion point, and also at any clamping points. Nevertheless, discrimination between cracks and background features is relatively straightforward, compared to other conventional active thermography methods.

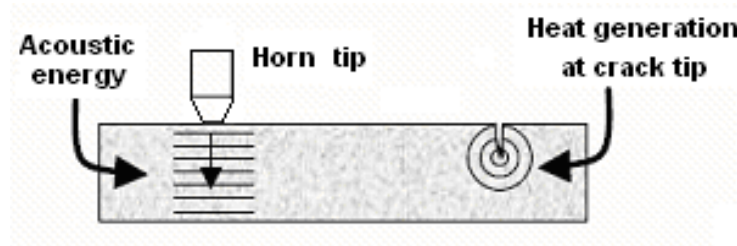


Fig. 2.9 : Sketch of basic vibrothermography interaction. Acoustic energy from a horn is injected into a solid sample, causing frictional heating at the tip, or along the faces of a crack.

In vibrothermography, flaws are excited at specific mechanical resonances. Local subplates formed from delaminations resonate independent of the rest of the structure at particular frequencies. Consequently, by changing (increasing or decreasing) the mechanical excitation frequency, local thermal gradients may appear or disappear. Finite element modeling applying 3D equations of linear elasticity permits us to evaluate local energy concentration for components submitted to mechanical loading.

However, in some circumstances, mechanical loading provokes breakdown of the sample. This is explained by dynamic instability: *one side of the hole takes more load than the other and thus becomes hotter, while on the other side, loss of stress stop heat generation.*

In vibrothermography technique most significant advantages are the detection of flaws hardly visible by other infrared thermography schemes, and the ability to inspect large structural areas in situ provided that required mechanical loading can be achieved.

2.4 Infrared detectors

An *infrared detector* or *sensor* is a device that converts radiant energy into some other measurable form, *e.g.* an electrical current. There are two main classes of infrared sensors: *thermal* and *photonic* (or *quantum*) detectors.

A thermal detector responds to incident radiation by raising its temperature. When a thermal detector is at equilibrium there is no thermal conduction, the sensor simply radiates energy at the same rate as it absorbs it. The detector's temperature will increase whenever the incident radiation rises above the equilibrium state, the detector absorbs more energy than it radiates. The excess temperature is then removed away by conduction. Types of thermal detectors include thermocouples, bolometers, pneumatic detectors, pyroelectric detectors and liquid crystals. Thermal detectors response is theoretically independent of wavelengths and they display high sensitivity at room temperature (see microbolometric spectral curve in fig. 2.11).

A photonic detector is made from semiconductor materials and operates on the principle that incident radiation excites electrons from the valence to the conduction atomic bands. Even though they provide superior sensitivity and fast response time than thermal sensors, photon detectors typically require cryogenic cooling to minimize the noise to obtain the high relative sensitivity.

In summary, thermal detectors exhibit a modest performance, with slower response than photonic sensors, but they are less expensive and do not require cryogenic cooling as their photonic counterparts. Developments in both fields predicts that uncooled photon detectors and thermal detectors with better performance will soon emerge. In the next sections, firstly it will be discussed the problem of the atmospheric transmittance that define the accessible spectral bands for infrared sensor and then, some thermal and photonic detectors of interest for infrared imaging application are briefly presented.

2.4.1 Atmospheric Transmittance

Atmosphere is a complex mix of various gases, particles, and aerosols in different concentrations. These constituents both absorb and scatter radiation as it travels from the target to the thermal imaging system. A description of the transmittance of electromagnetic energy through this mix is thus a complicated task. The main problem concerns with the transmittance of electromagnetic energy which is less than 100%. Self-absorption by gas in the atmosphere (e.g . H₂O, CO₂, O₃) and diffusion due to particles such as molecules and aerosols are responsible for this. Moreover, various factors, such as the presence of thermal gradients and turbulences, make the index of refraction inhomogeneous and contribute further to degradation of the infrared measurement through the atmosphere.

Finally, the atmosphere itself emits infrared energy which is captured by the IR sensor. Most of these effects depend on the distance, wavelength and meteorologic conditions, they are thus not easily taken into account. In order of importance, main gases that absorb the radiation transmitted are water vapor (H₂O), then carbon dioxide (CO₂) and ozone (O₃).

Due to the atmospheric special transmittance, electronic imaging system design is partitionated into seven geneneric spectral regions. Four of these are associated with thermal imaging systems. The ultraviolet (UV) region ranges in wavelength from 0.2 to 0.4 μm . The visible region ranges in wavelength from 0.4 to 0.7 μm . Televisions, electronic cameras, and most solid state cameras operate in this region. The near infrared imaging spectral region (NIR) spans approximately from 0.7 to 1.1 μm . The first infrared imaging band is the short wavelength band (SWIR) which approximately covers from 1.1 to 2.5 μm . The second infrared band is the mid-wavelength infrared (MWIR), spectral region that covers approximately from 2.5 to 7.0 μm . The third infrared band is the long wavelength infrared (LWIR) spectral band. It covers the spectral region from approximately from 7 to 15 μm . The fourth infrared band is the far infrared or very long wave infrared (VLWIR) region. The last one applies to all systems whose spectral response extends over 15 μm . The MWIR and LWIR regions are sometimes called the first and second thermal imaging bands respectively.

Fig. 2.10 shows a typical atmospheric transmittance curve that accounts for absorption only. The dominant absorber in the 3 to 5 μm region is carbon dioxide (CO₂) which absorbs at 4.3 μm . This absorption band is obvious after a few meters of path length. Water vapor (H₂O) determines the upper and lower wavelength limits for both MWIR and LWIR spectral regions.

Water vapor is also the dominant absorber in the LWIR region. As the water vapor increases, the LWIR transmittance decreases more quickly than the MWIR transmittance. This implies that a MWIR system may be better in a tropical or maritime environment.

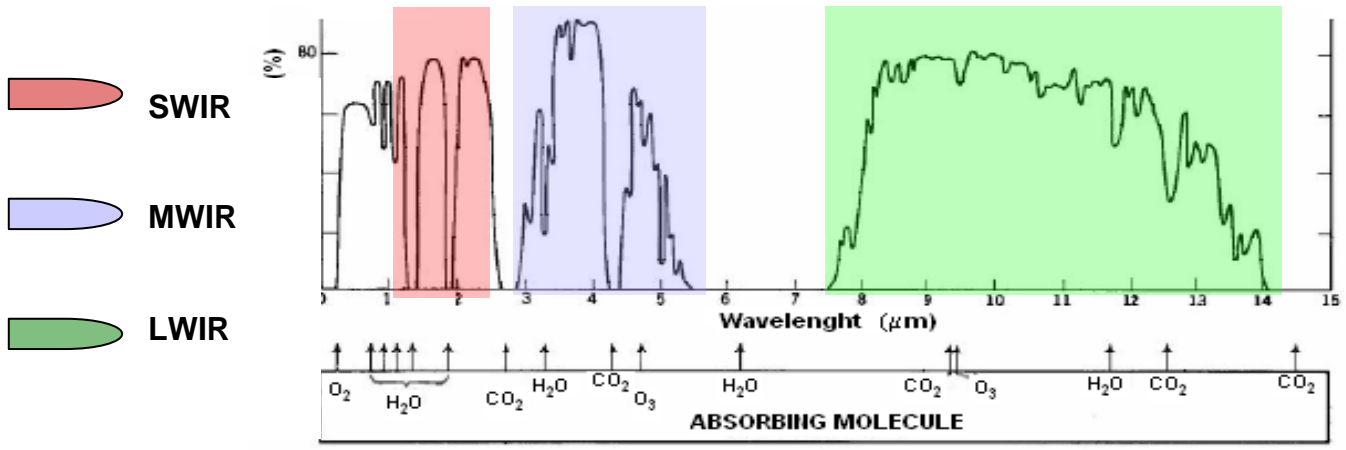


Fig. 2.10 : Atmospheric transmittance and infrared imaging bands

The selection of the operating wavelength band is affected by the application. For the majority of nondestructive-testing applications, the useful portion of the infrared spectrum lies in the range from 0.8 to 15 μm, beyond 15 μm applications are more exotic, such as high-performance Fourier transform spectrometers, which operate around 25 μm. The choice of an operating wavelength band is also important because dictates the selection of the detector type, as fig. 2.11 shows.

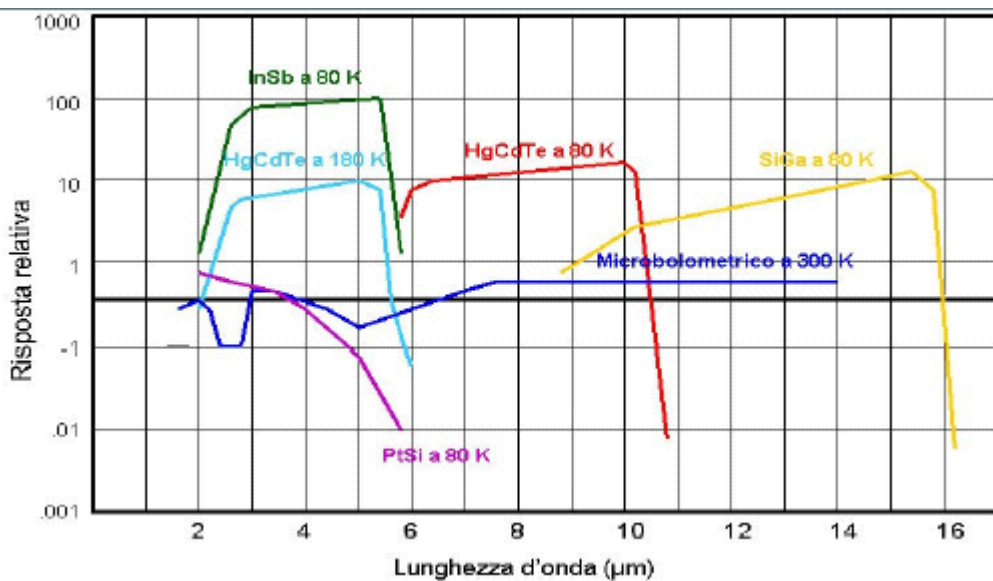


Fig. 2.11: Spectral response curves for some infrared detectors in different infrared regions

Among the important criteria for band selection there are operating distance, indoor-outdoor operation, temperature, and emissivity of the bodies of interest. As Planck's law says, high-temperature bodies emit more in the short wavelengths, consequently, long wavelengths will be of more interest to observe near room-temperature objects. Emitted radiation from ordinary objects at ambient temperature (300 K) peaks in this long-wavelength range. Long wavelengths are also preferred for outdoor operation where signal are less affected by radiation from the sun. For operation distances restricted to a few meters in the absence of fog or water droplets, atmospheric absorption has little effect. Spectral emissivity is also of great importance since it affects the emitted radiation.

Although no specific rule can be formulated, the most useful bands are from 3 to 5 μm (MWIR) and from 8 to 12 μm (LWIR) since they match the atmospheric transmission band. Most of the infrared commercial products and thermographic applications fall in these categories. The SWIR band, instead, is principally used in applications where reflected infrared property of samples are important.

However, detailed studies [79-81] have concluded that for temperature in the range from -10 to +130 $^{\circ}\text{C}$, measurements can be done without much difference in both bands (from 3 to 5 and from 8 to 12 μm). For some special applications (e.g. for the military), bispectral cameras operating simultaneously in both bands have been developed to characterize target thermal more accurately.

2.4.2 Bolometers

Bolometers are thermal detectors. For bolometers, such as thermistors, the relevant physical property is the electrical conductivity. Consequently, a current must cross the element for signal generation. It should, however, be noted that this current, having its own fluctuation, adds to the detector noise. One of the main drawbacks of bolometers is in their slow response time (from 1 to 100 ms), which restricts their use to slowly varying processes. The figure of merit of bolometers is the resistive temperature coefficient defined as

$$\alpha = \frac{1}{R_B} \frac{dR_B}{dT} \tag{2.14}$$

where R_B is the internal resistance of the bolometers and T the temperature. The value of this coefficient is either positive or negative, depending on the conduction mechanism taking place within the material of interest. Typical values are $0.1\% \text{ K}^{-1}$ for metal, from 1 to $10\% \text{ K}^{-1}$ for semiconductors, and higher values for superconductors. Recently arrays of microbolometers have opened a whole range of new infrared imagers.

2.4.3 Pyroelectric detectors

Pyroelectricity is defined as the property of certain crystals to produce a state of electric polarity by a change in temperature. A broad class of thermal detectors are pyroelectric detectors. For these detectors below the Curie temperature¹ electric charges are generated by incident radiation absorption (heating): a change in the detector temperature generates a transient change in the surface charges, thus causing a transient current available for pickup by the readout unit. Pyroelectric detectors are sensitive only to temperature variations and thus need a chopper while modulates the incoming radiation in order to maintain a signal output, unless the system is panned over the scene. This added complexity is a severe drawback. The figure of merit of pyroelectric detectors is the pyroelectric coefficient p , defined as the slope of the material polarization P versus temperature T at the operating temperature

$$p = \frac{dP}{dT} \tag{2.15}$$

This effect can be improved with the application of an electrical field bias.

¹ Temperature below which there is a spontaneous magnetization in the absence of an externally applied magnetic field

2.4.4 Quantum Detectors

Quantum detectors are solid-state photonic detectors in which photon interactions either change conductivity (photoconductor) or generate voltage (photoelectric, also called photovoltaic). Since no heating phenomenon is needed as in case of a thermal detector, the response time is short while the solid-state structure made these detectors compact, reliable, and robust. Consequently, they are quite popular. For photoconductive detectors an external current is necessary to measure conductivity change while photoelectric (photovoltaic) detectors act as a power generator, supplying a signal without need for polarization. Since biasing current is needed for photoconductor detectors, high-charge-capacity alkaline batteries can be used to induce minimum noise and ripple. This is essential to achieve stable results. In this respect, since photovoltaic detectors supply a signal by themselves, they are much more attractive than photoconductor detectors, requiring less complex readout circuits. Common materials used in photoelectric (photodiodes and phototransistors) are InAs, InSb, GaAs, PtSi and HgCdT. Fig. 2.11 presents the spectral response curves for the most common detectors.

- InSb

Indium antimonide (Insb) is a high quantum efficiency MWIR detector. It has generally replaced PtSi in those systems using modest sized arrays (e.g. standard video format with approximately 640x480 elements). Its peak response is near 5 μm . A filter is used to limit the spectral response to the MWIR region.

- HgCdTe

Mercury cadmium telluride (HgCdTe or MCT) is a mixture, in different ratio, of $\text{Hg}_{1-x}\text{Cd}_x\text{Te}$. By varying the ratio, the spectral response can be tailored to the MWIR or LWIR region. The most popular is the LWIR with a peak response near 12 μm . A filter is used to limit the response to the LWIR region. HgCdTe detectors are used in all common module systems.

- QWIP

The quantum well infrared photodetectors (QWIP) is based upon GaAs growth technology. The wells are created by layers of GaAs/AlGaAs and the response can be tailored from 3 to 19 μm . The LWIR version has a spectral responsivity from 8.3 to 10 μm . The responsivity and noise are temperature sensitive so that QWIP devices are cooled to less than 60 K.

2.5 Infrared Imaging Devices: Focal Plane Arrays (FPA)

In 1980s a new kind of imaging device started to appear and revolutionize the infrared community: large-dimensional infrared arrays simplified infrared camera construction. Due to their initial expensive cost, these devices have become popular only in the last fifteen years. Focal Plane Arrays (FPAs) are today's most common IR imaging devices configuration. A FPA is made up of rows and columns of individual infrared detectors. Using this technology, all what is needed to build an infrared camera is the optics, the focal plane array (FPA), the associated electronics, and for some detector technologies, a cooling unit. Similar to conventional video CCDs, these chips do not require any electromechanical scanning mechanism (no moving parts) for image forming and are less fragile than pyroelectric tubes. Video signals are obtained directly by on-chip electronics drive.

The fill factor is an important parameter in selecting FPAs, it provides the IR-sensitive material to total surface (including the signal transmission paths) ratio. The higher the fill factor, the higher the sensitivity, the cooling efficiency and the overall image quality of the system. If FPAs have both IR-sensitive material and signal transmission paths on the same layer they are called *monolithic* FPAs. Conversely, an *hybrid* array has the IR-sensitive detector material on one layer and the signal-transmission and processing circuitry on another layer bonded together by small collecting bumps. Hence, monolithic FPAs are easier and less expensive to manufacture than hybrid FPAs, but they generally have lower performance since, having the detector material and signal pathways on the same level significantly reduce the fill factor (~55% for a monolithic FPA vs. ~90% for a hybrid FPA). The readout device is also important. An FPA can use one of two technologies, a Charge Coupled Device (CCD) or a Complementary Metal Oxide Semiconductor (CMOS). The principal advantages of CMOS with respect to CCDs are: lower fabrication cost, possibility of developing a single-chip camera, lower voltages and have lower power requirements (portability), possibility to read out a portion of the array rather than the entire array (windowing). On the other hand, CMOS have much higher noise than CCDs, since CMOS have more on-chip circuitry and uses amplifiers for each pixel, producing nonuniformities known as Fixed Pattern Noise (FPN). FPN can be removed by recording the pattern and post processing with software to remove it [rif], but this further reduces the useful dynamic range. Furthermore, the sensitivity and the filling factor (< 30%, the amplifiers also take up more area) of the CCD is much greater. CMOS is expected to dominate in the low end consumer market (camcorders, snapshot cameras, toys, etc.) and

other specialty applications such as surveillance. However, CCDs will remain unchallenged for scientific and technical applications requiring high fidelity, resolution, and dynamic range in the next future.

- Microbolometer Arrays

In the early 1980s, with the broader availability of large integrated-circuit fabrication technology, it was possible to build large uncooled bidimensional arrays based on microbolometers.

With micromilling technology, it is now possible to constitute arrays with thousands of tiny bolometers called microbolometers, which are, in fact, thermal masses (also called microbridges) hung by low-thermal-conductivity arms supported on metal legs anchored in the silicon substrate, thus enabling a direct interface with readout electronics located under the array (fig. 2.12). The IR radiation heats the hanging mass, modifying its electrical conductivity so that a voltage or current variation appears at the device outputs. These arrays are, for example, built using planar MOS or thin coating technologies adapted to micromilling. One common technology is the VO_x (vanadium oxide). Nowadays, ferroelectric microbolometer arrays have performances such as time constant t on the order of a few milliseconds, detectivity on the order of 10^7 to $10^9 \text{ cm Hz}^{1/2} \text{ W}^{-1}$, NETD (Noise Equivalent Temperature Difference) 50 mK, and a pixel size of $25\mu\text{m}$ (since 1024×768 array size)



Fig. 2.12 : *Microbolometers array*

2.5.1 Detectors: Performance parameters

In order to compare different detectors available on the market, it is very useful to know the most used figure of merit for infrared devices. A brief description of some of them is given in this section.

- Impedence

The detector impedance Z is an intrinsic characteristic of detectors measured using Ohm's law

$$Z = \frac{dV}{dI} \quad 2.16$$

This parameter is an important design property since the maximum power we can extract from such a detector is reached when

$$Z = Z_A \quad 2.17$$

Where Z_A is the input impedance of the preamplifier to which the detector is connected. A correct impedance match is important to maximize the output signal since electric signal at the detector output are generally small.

- Responsivity

Another important parameter is the responsivity expressed in voltage (R_V) or current (R_I) and which is the transformation ratio of the incident optical flow F

$$R_V = \frac{dV}{dF} \quad R_I = \frac{dI}{dF} \quad 2.18$$

Responsivity is generally not uniform on the detector area, moreover, it also depends on the radiation wavelength and excitation frequency.

- Time constant

A useful property is also the time constant τ , which specifies the response time of a detector.

It is given by

$$\tau = \frac{1}{2\pi f_c} \quad 2.19$$

f_c is the critical frequency defined by an observed decrease of 3 dB in the maximum amplitude.

- Noise Equivalent Power

A very important figure of merit for detectors is the noise equivalent power (NEP). This is the amount of power induced by an optical signal whose amplitude is equivalent to intrinsic noise power present at the detector output without signal, which originates from thermal agitation and optical radiation granularity.

- Noise Equivalent Temperature Difference

Many detector manufacturers rate their detectors using the noise equivalent temperature difference (NETD) instead of NEP. NETD corresponds to the change in temperature of a large blackbody² in the observed scene, causing a change in the signal-to-noise-ratio of unity in the output of the detector. NETD depends on the F-number³ of the optics and on the pixel size.

- Detectivity

The detectivity D is also a widely used parameter to specify detectors. It is given by

$$D = \frac{1}{F_{NEP}} \quad 2.20$$

When F_{NEP} is the optical flow called the *noise equivalent flow*. D should be high, to obtain a reasonable signal-to-noise ratio. The detectivity depends on many parameters : spectral content and modulation of the incident radiation, receiver system bandwidth, detector temperature, and sensitive surface area.

² Perfect emitter of infrared radiation with max value of emissivity

³ The F-number of a lens is given by its focal distance divided by its effective diameter aperture

2.6 New approach of infrared imaging in medical science

Infrared imaging allows the representation of the surface thermal distribution of the human body. Several studies have been performed so far to assess the contribution that this kind of information may give to clinicians. During the last 30 years it has been widely discussed whether or not infrared imaging should be considered a good diagnostic tool. The approach generally followed consisted of the detection of significant differences between the skin thermal distributions of the two hemispheres or in the evaluation of the mismatches of the skin thermal distribution with respect to an average extrapolated from a control group. So, after the contradictory results obtained during the 1970s, a general lack of confidence has arisen among clinicians regarding the clinical use of infrared imaging.

Simultaneously, but for other purposes, technological improvements released a new generation of digital infrared cameras characterized by :

- high spatial resolution
- optimized temperature sensitivity
- very short acquisition time

By means of the last generation infrared cameras, it is possible to record in real time all the modifications of the skin thermal distribution following a physiological or environmental processes; i.e. the action of vasodilator or vasoconstrictor substances or the execution of thermal stresses.

A dynamic approach to infrared imaging by means of the characterization of the dynamics of the thermal recovery is therefore possible [82]. This permits to overcome the limitation of conventional infrared imaging and to use a new approach based on the modelling of functional parameters [83].

The functional infrared imaging is the study of the functional properties and alterations of the human thermoregulatory system based on the modelling of the bio-heat exchange processes.

The skin temperature distribution of the human body depends on the complex relationships defining the heat exchange processes between skin tissues, inner tissues, local vasculature, and metabolic activity. All these processes are mediated and regulated by the sympathetic and parasympathetic activity to maintain the thermal homeostasis. The presence of a disease can locally affect the heat balance or exchange processes resulting in an increase or in a decrease of

the skin temperature. Such a temperature change can be better estimated with respect to the surrounding regions or the unaffected contra lateral region. But then, the dynamics of the local control of the skin temperature should be also influenced by the presence of the disease. Therefore, the characteristic parameters modelling the activity of the skin thermoregulatory system can be used as diagnostic parameters.

The aims of this new approach of infrared imaging is highlighting the functional contents of skin thermal distribution, by evaluating qualitatively and quantitatively how the lesion or the disease alters the thermoregulatory response of the damaged or ill area with respect to the healthy ones.

Several studies have been performed so far to assess the contribution that this new approach may provide to the medical science. Infrared technology is used for:

- Valuation of re-perfusion process during surgery (thermo-angiography) [84]
- Follow up of the modification of the neurovascular functions of the treated district by means of the study of thermoregulatory properties [85, 86]
- Assistance to cardiac surgery and microsurgery, for which the real time evaluation of the re-perfusion processes and the estimate of the recovery of the neurovascular functions constitute important information during the follow up [84, 87]
- Validation and detection of sub-clinical varicocele [88-90]

Moreover, Infrared Imaging was used to record the temperature variation of the hands associated with sympathetic skin response [91]. The submotor thermal response may be used in the future as complementary or alternative monitoring of the activity of the autonomous system in conditions where the traditional sympathetic skin response cannot be recorded.

The new infrared approach is used, also, to determine the major infrared thermographic parameters in discriminating between patients with and without secondary Raynaud's phenomenon. Some of these regard the Raynaud's phenomenon secondary to Scleroderma (SSc) or chronic vasospastic syndromes [92-95].

Recently, a novel method of estimation of blood flow speed and vessel location from thermal imaging recording has been developed. The method is based on a bioheat transfer model that reflects the thermo-physiological processes in a skin region proximal to a major vessel [96].

A new possibility on the remote control of the human functional parameters is given from a novel method to measure human cardiac pulse at a certain distance. It is based on the

information contained in the thermal signal emitted from major superficial vessels [97-99]. The contribution that the functional infrared imaging can give in the diagnosis of the breast cancer has not been clarified. Some studies show how as the infrared imaging, thanks to pattern recognition methods, can individualize the tumoral neoangiogenesis and the excessive production from endothelium of nitric oxide associated to the lesion. Anyway, the capacity to localize the tumor with this technique is subordinates to the realization of new realistic model of the thermal diffusion in vivo [100-102].

The technology is expected to find applications among others in sustained physiological monitoring of cardiopulmonary diseases, sport training, sleep studies, and psychophysiology (polygraph).

All these studies (and many others) has proved that infrared thecnology can be advantageously used in these field thanks to its new features, overall thanks to new dinamyc approach and new images elaboration methods.

Chapter 3

INFRARED MONITORING ON PLANE ANGIOMA :

PT model and numerical simulation

3.1 Introduction

In the first chapters the problems concerning to laser applications in medical fields and infrared imaging technologies have been described.

In this chapter, instead, it will be given a detailed description of the activity research, object of the present thesis-work, in which the laser - biological tissue interaction on patients affected by plane angioma pathology has been monitored and studied with the infrared imaging technology. Subsequently, the approach employed, the pathology analyzed and computation instruments used (pulsed thermography model and a numerical simulation) will be treated and discussed.

This activity has been realized in collaboration with the LIRT of the Cybernetic Institute "E. Caianiello" - ICIB-CNR and in collaboration with the dermatological division of the II Policlinic in Naples in the laser therapy and photodynamics ambulatory.

3.2 Infrared monitoring of plane angioma treatment: approach description

In the last years, the employment of different laser systems for more and more medical treatments has had an exponential growth. The effects of the laser radiation on different organic tissues aren't easily standardizable, because of dermatological differences showed from different anatomic regions of the body and in different people. This indetermination influences the therapeutic results obtained, and, in the majority of cases, they are unsatisfactory or even harmful. The scientific research in this field is addressed to obtain quantitative and functional information about the dynamic of this interaction in order to allow specialists to employ laser systems in a more specific, well controlled and less empirical way.

Infrared imaging technology can be used, in this field, for a real-time monitoring of the laser-biological tissue interaction. This technique can give to specialist information about the reaction of the tissue in the specific region treated.

In this activity the main pathology monitored and studied with infrared technique has been the Plane Angioma known as Port Wine Stain (PWS) pathology. This pathology, as described in the next section, is a vascular malformation that consists in a blood vessels accumulation under the tissue. This accumulation forms a subsurface *plane of vessels* of depth and thickness depending on the specific anatomic region and, in general, differs from case to case.

The main problems in the cure of plane angioma with laser therapy are:

- The therapeutic efficiency can differ a lot from patient to patient. In general it can depend on the age, anatomic region, phototype, lesion depth and lesion thickness. Usually, in the median region of the face the therapeutic efficiency is better than external area.
- Possible formation of scars
- Possible formation of dischromic area

In the laser treatments on patients affected by Plane Angioma the therapeutic program and laser parameters are chosen following general tables and indications present in literature. In the next table it is shown the reference range for laser parameters advised in literature for the treatment of patients with Plane Angioma:

Referential range for laser parameters	
Wavelength	585 – 595 nm
Energy density	4 – 10 J/cm ²
Pulse duration	1 – 5 ms
Spot diameter	2 - 7 mm

Tab. 3.1: *Laser parameters for Plane Angioma treatments*

Even if modern laser system permitted more and more control on the operative variables, nowadays it is the operator who chooses the system and the operative protocol. In general, the specialist starts from the laser parameters showed in the table and then he changes these parameters based on his own experiences and so in a very empiric way.

In the research activity, object of this work-thesis, the effects of the laser-biological tissue interaction on PWS patients have been studied through the information obtained with infrared imaging technique.

With this technique it's possible to obtain information about a specific plane of vessels under treatment monitoring the thermal reaction of the tissue under laser action. The main purposes of this study have been:

- **To evaluate the support of the infrared imaging, in the dermatological field, as an efficient tool for scientific investigation**

And particularly

- **To evaluate the employment of this technique as a tool for the control and optimization of laser parameters in order to make the treatment more safety and more efficient**

So, with the intent of optimized laser parameters for each specific plane of vessels treated by specialist, the next approach has been studied.

First of all, in order to find morphological information for the specific plane of vessels under treatment a Pulsed Thermography model has been used.

With this model, in fact, from the temporal evolution of the surface's temperature obtained after a single laser pulse-test (heat source), it is possible to get a local evaluation of the depth and thickness of the plane angioma in the anatomic area that the physician wants to treat. This information permits a morphological reconstruction of the multilayer biological tissue under treatment.

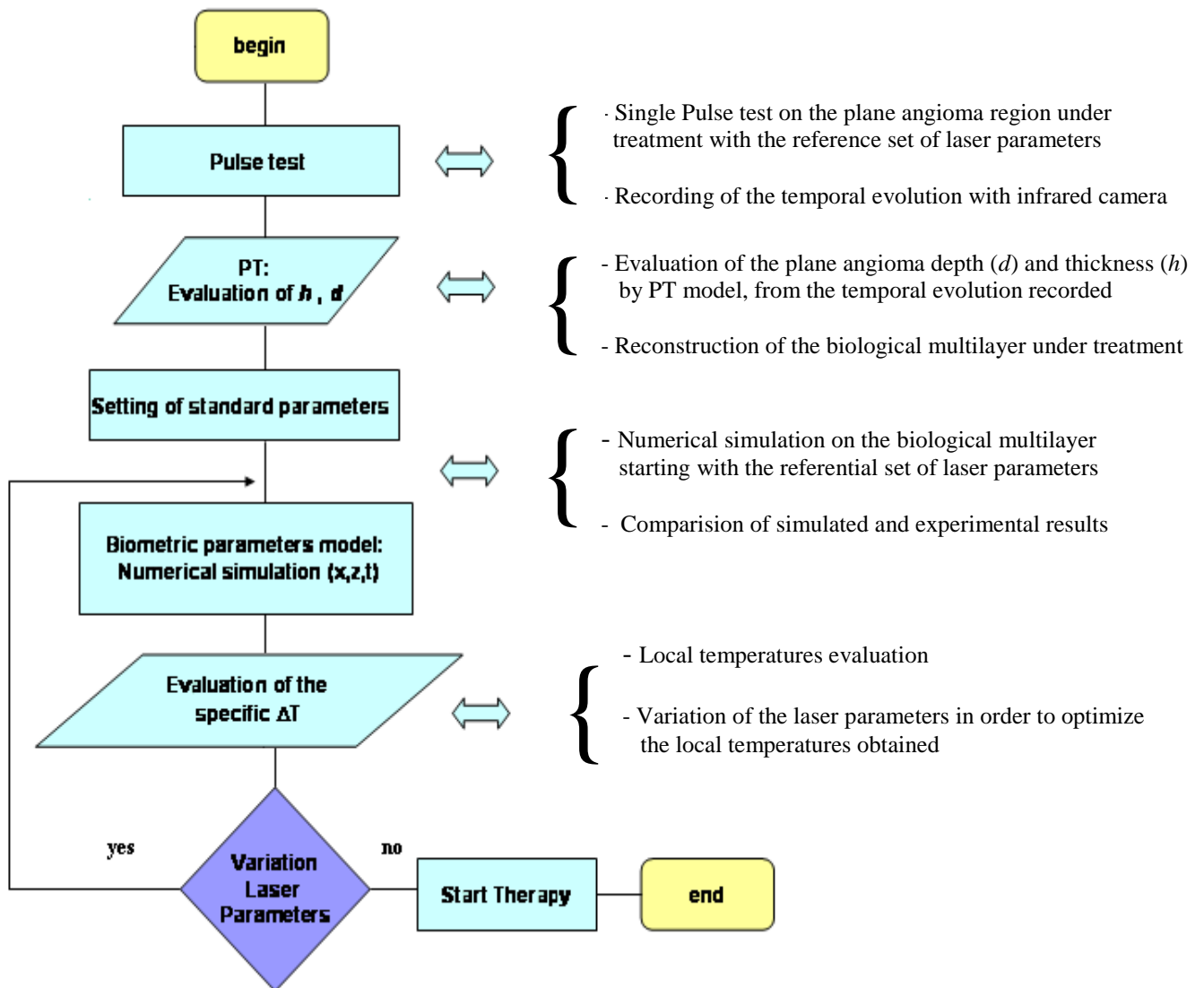
Subsequently, it is executed on this multilayer a 2D+1 numerical simulation based on a biometric heat transfer model. In the simulations the thermal behaviour of the biological multilayers can be achieved with different set of laser parameters as input.

The numerical output consists of the evaluations of the spatial and temporal temperature profiles.

Finally, these results can be used:

- To compare the thermal behaviour simulated on the multilayer's surface with the experimental data (recorded with an infrared camera) in order to check the approach performed.
- To optimize the laser parameters in order to achieve suitable local temperatures in the multilayer for the photocoagulation of the blood vessels and for reducing the risk of scars formation

Schematically, this approach can be synthesized in the next operative flow-chart :



As it is possible to see from the flow-chart, in this operative approach, the results achieved from simulations are used as a feedback in a loop in order to optimize laser parameters and so to optimize the therapeutic efficiency.

In the next sections the plane angioma pathology, the pulsed thermography model and the numerical simulation used in this approach are described and discussed extensively.

3.3 Plane angioma pathology (Port Wine Stain)

In the last 20th years, one of the field in which is much more concentrated the dermatological interest has been the treatment of the skin vascular lesion as plane angiomas (known as Port Wine Stain or Nevus Flammeus too). As it is well known, the plane angioma is a benign tumor made of blood vessels accumulation newformed and malformed. This vascular malformation, is congenital and it is present in about 3 newborns on 1000 with the same incidence for male and female. PWSs are present at birth and persist throughout life. Rarely, acquired PWS can occur at any age after birth and it is identical to congenital capillary malformations both clinically and histologically.



The exact mechanism (causes) remains unknown. Evidence for genetic influence is lacking. Capillary malformations may result from a neural deficiency of sympathetic innervation of the superficial dermal blood vessels. The mean dimensions of the blood vessels in a plane angioma are reported in the next table

Blood vessels dimensions	
Thickness	20 – 180 μm
Depth	200 – 1300 μm

Tab. 3.2 : Mean dimensions of the blood vessels in a plane angioma

The area of the skin affected grows in size commensurate with the general growth. Plane angioma occur most often on the face but can appear anywhere on the body. Early stains are usually flat and pink in appearance. As the child matures, the color may deepen to a dark red or purplish colour. The color of the capillary malformation does not correlate with the capillary depth or diameter. In adulthood, thickening of the lesion or the development of small lumps

may occur. A physician can usually diagnose a PWS based entirely upon the history and appearance. In unusual cases, a skin biopsy may be needed to confirm the diagnosis.

Many treatments have been tried for PWS including freezing, surgery, radiation, and tattooing, (plane angioma can also be covered with cosmetics). Lasers have had the biggest impact on treatment, because they are the unique method for destroying the cutaneous capillaries without a significant damage to the overlying skin. During the years many type of laser system have been used: CO₂ , Argon laser, Nd:Yag and others, but several study and experiences have highlighted as the FPDL (Flash-Pump-Dye-Laser) is, at present, the laser system tool more efficient and less dangerous for curing PWS patients. Treatment of infants with the FPDL generally produces marked improvement in appearance. However, in general, complete disappearance is rare.

Usually, in approximately 20-25 % of cases there is an optimal improvement, in 30-35 % the improvement is acceptable and, unfortunately, in approximately 50% of cases the therapy is less incisive and there may be no improvement. Stains on the face respond better than those on the trunk or limbs. Older stains may be more difficult to treat. In the absence of successful treatment, hypertrophy (increased tissue mass) of the stains may occasionally produce deformity, loss of function (especially near the eye or mouth), bleeding, and increasing disfigurement. These complications are usually seen later in life and psychosocial disability secondary to facial disfigurement can be overwhelming. If the PWS is on the face or other highly visible part of the body, the presence of PWS cause emotional and social problems for the affected person because of their cosmetic appearance. Several studies demonstrate that patients with facial capillary malformations exhibit greater self-concern, ruminative self-doubt in interpersonal interactions, social inhibition, isolated and passive orientation in interpersonal relationships, stigmatization from society, and limitations of privileges and opportunities otherwise afforded to those without facial disfigurement. A study demonstrated that the psychosocial difficulties not only persisted but actually worsened in adulthood [103].

In same cases (about 5%) plane angiomas can be a cutaneous finding of several syndromes as: Sturge-Weber syndrome, Klippel-Trenaunay syndrome, Proteus syndrome, Parkes-Weber syndrome, Von Hippel – Lindau syndrome, Cobb syndrome, Wyburn-Mason syndrome and others.

3.4 Pulsed Thermography model

In this work, in order to find unknown parameters for each specific subsurface plane of vessels, it has been used a tested modelling approach of pulsed thermography (PT) based on the use of the 3D thermal quadrupole formalism [56, 57]. In general, with this approach, from the temporal evolution of the superficial temperature, it is possible to estimate the depth and the thickness of a subsurface anomaly or disomogeneous area present in a structure. In the multilayer biological structures analyzed in this work, the role of subsurface anomaly is represented by the plane of vessels associated with the presence of a plane angioma [rif ben]. In this model, three-dimensional thermal quadrupoles are obtained by applying to the real temperature field a Laplace transform in the time domain, then a double Fourier transform in the space domain is applied to the previous Laplace temperature field. After the last three integral transforms, the temperature field is treated in the Laplace–Fourier–Fourier image domain.

A plane of blood vessels, in a multi-layer biological tissue, is thermally characterized by a thermal contact resistance. Because this resistance is small compared with the tissue whole resistance, a perturbation method [104-106] can be applied and combined with the thermal quadrupole formalism to yield simple analytical solutions of the nondestructive experiment. The perturbation procedure is based on an asymptotic expansion of the physical field (temperature or heat flux) versus a small parameter intervening in the model. The analytical solutions obtained via this method are very convenient for the development of new inversion procedures which characterize the subsurface anomalies within a three-dimensional heat transfer configuration.

Resuming, in this model, in order to accurately identify the unknown parameters associated to anomaly, two stages have been considered:

- 1) The first step is to develop a forward model which consists of describing the contrast field evolution in a mathematical formalism as accurately, simply and rapidly as possible
- 2) The second step is to develop an inverse problem that estimates the unknown parameters in order to minimize the deviation between the experimental data and the forward problem

These two important steps will be accurately described in the next subsections.

3.4.1 Formulation of the forward problem: 3D thermal quadrupoles

This model refer to the case of a rectangular ($L_1 \times L_2$) multilayer sample of thickness d_1 that contains a resistive anomaly of finite width a and finite length b , with a uniform contact resistance R_c on its whole area, typical of biological tissue affected by plane angioma.

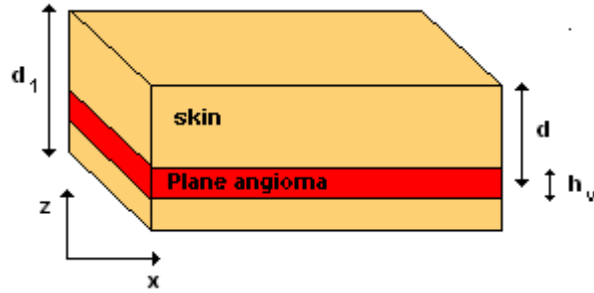


Fig. 3.1: Multilayer sample of thickness d_1 , with a plane angioma depth d and thick h_v

In a typical pulsed infrared thermography test, one can assume that:

- 1 - the thermal excitation of the sample is a Dirac distribution characterized by a uniform absorbed energy Q (at time $t = 0$)
- 2 - the front face of the sample is adiabatic
- 3 - the sample temperature is zero before excitation

Since only the face temperatures are of interest, the quadrupole technique is the easiest formalism to implement in order to describe the heat transfer. Thermal quadrupoles are obtained after performing a Laplace integral transform on the time variable t , and a double Fourier integral transform on the space variables x and y [23, 24 riferim]. Heat transfer modelling of multi-layer materials is then reduced to a simple multiplication of matrices in the transformed Laplace–Fourier–Fourier domain. First of all, recall here the heat equation in 2+1 dimensions:

$$k_z \frac{\partial^2 T}{\partial z^2} + k_x \frac{\partial^2 T}{\partial x^2} + k_y \frac{\partial^2 T}{\partial y^2} - \frac{\partial T}{\partial t} = 0 \quad 3.1$$

where T is the temperature and k is the thermal conductivity. If the initial temperature is uniform and if the heat losses are neglected, the Laplace transform $\tau(x, y, z, p)$ (where p is the Laplace variable) of the temperature $T(x, y, z, t)$ in the sample is the solution of the following set of equations:

$$\begin{aligned}
& \frac{\partial^2 \tau}{\partial z^2} + \frac{k_x}{k_z} \frac{\partial^2 \tau}{\partial x^2} + \frac{k_y}{k_z} \frac{\partial^2 \tau}{\partial y^2} - \frac{p}{k_z} \tau = 0 \\
& x = 0, L_1 \rightarrow \frac{\partial \tau}{\partial x} = 0 \\
& y = 0, L_2 \rightarrow \frac{\partial \tau}{\partial y} = 0 \\
& z = 0 \rightarrow -k_z \frac{\partial \tau}{\partial z} = Q \\
& z = d \rightarrow \frac{\partial \tau^{\text{sup}}}{\partial z} = \frac{\partial \tau^{\text{inf}}}{\partial z} \\
& \tau^{\text{sup}} - \tau^{\text{inf}} = R_c s(x, y) \left[-k_z \frac{\partial \tau}{\partial z} \right]
\end{aligned} \tag{3.2}$$

with $s(x, y) = 1$ for (x, y) inside the anomaly region $[(x_1, x_2), (y_1, y_2)]$ and $s(x, y) = 0$ elsewhere, d is the depth of the anomaly. Superscripts *sup* and *inf* relate to the upper and lower face of the anomaly

$$z = d_1 \rightarrow \frac{\partial \tau}{\partial z} = 0 \tag{3.3}$$

The analysis can simultaneously be performed for both isotropic and anisotropic materials (providing that the sample faces are parallel to the main directions of anisotropy) by using the following dimensionless governing parameters:

$$\begin{aligned}
\tau^* &= \tau(Qd_1/k_z) & a^* &= \frac{a}{d_1} (k_z/k_x)^{1/2} \\
\psi^* &= \psi/Q & b^* &= \frac{b}{d_1} (k_z/k_y)^{1/2} \\
x^* &= \frac{x}{d_1} (k_z/k_x)^{1/2} & p^* &= d_1^2 p/k_z \\
y^* &= \frac{y}{d_1} (k_z/k_y)^{1/2} & R_c^* &= R_c/(d_1/k_z) \\
z^* &= z/d_1 & d^* &= d/d_1
\end{aligned} \tag{3.4}$$

where ψ is the Laplace transform of the z component of the heat flux density $\varphi = -k_z (\partial T / \partial z)$.

In the remaining text of this chapter, the asterisk superscript in the above parameters will be omitted for clarity reasons. The partial differential equation in 3.2 then becomes

$$\frac{\partial^2 \tau}{\partial z^2} + \frac{\partial^2 \tau}{\partial x^2} + \frac{\partial^2 \tau}{\partial y^2} - p \tau = 0 \quad 3.5$$

The next step is to apply a Fourier transform to the function $\tau(x, y, z, p)$. The lateral boundary conditions determine the type of transform to carry out [25], in this case it is a cosine shape

$$q(\alpha, \beta, z, p) = \int_0^{L_1} \int_0^{L_2} \tau(x, y, z, p) \cos(\alpha x) \cos(\beta y) dx dy \quad 3.6$$

As for the boundary conditions on the opposite faces $x = L_1$ and $y = L_2$, they determine the discrete values allowed for the space frequencies: $\alpha_j = j\pi/L_1$, $\beta_k = k\pi/L_2$, j and k are non-negative integers.

Using equation (3.6) and the lateral boundary conditions, equation (3.5) yields

$$\frac{d^2 \theta}{dz^2} - (p + \alpha^2 + \beta^2) \theta = 0 \quad 3.7$$

The solution of equation 3.7 has the following form:

$$\theta = F \cosh(uz) + G \sinh(uz) \quad 3.8$$

where $u = (p + \alpha^2 + \beta^2)^{1/2}$ and F and G are two constants that can be determined using the boundary and interface conditions in z . If θ is known, back inversion into the Laplace domain is given by

$$\tau(x, y, z, p) = \frac{1}{L_1 L_2} \left[\theta_{00} + 2 \sum_{j=1}^{\infty} \theta_{j0} \cos(\alpha_j x) + 2 \sum_{k=1}^{\infty} \theta_{0k} \cos(\beta_k y) + 4 \sum_{j=1}^{\infty} \sum_{k=1}^{\infty} \theta_{jk} \cos(\alpha_j x) \cos(\beta_k y) \right] \quad 3.9$$

where $\theta_{jk} = \theta(\alpha_j, \beta_k, z, p)$.

If ϕ is the Fourier transform of the Laplace heat flux density ψ , which is unity at $z = 0$ and zero at $z = 1$ (equations 3.2 and 3.3) we obtain

$$\begin{aligned} z = 0 & \rightarrow \phi(\alpha, \beta, 0, p) = \frac{\sin(\alpha L_1)}{\alpha} \frac{\sin(\beta L_2)}{\beta} \\ z = 1 & \rightarrow \phi(\alpha, \beta, 1, p) = 0 \end{aligned} \quad 3.10$$

If the arguments other than z are omitted in the Laplace–Fourier transforms θ and ϕ , this equation leads to a linear relationship between the two quantities on the front ($z = 0$) and rear ($z = 1$) faces

$$\begin{aligned} \theta(0) &= A\theta(1) + B\phi(1) \\ \phi(0) &= C\theta(1) + D\phi(1) \end{aligned} \quad 3.11$$

Boundary conditions in (3.2) and (3.3) can be rewritten under the following matrix forms, commonly called quadrupoles [107]:

$$\begin{aligned} \begin{bmatrix} \theta(0) \\ \frac{\sin(\alpha L_1)}{\alpha} \frac{\sin(\beta L_2)}{\beta} \end{bmatrix} &= \begin{bmatrix} A_1 & B_1 \\ C_1 & D_1 \end{bmatrix} \begin{bmatrix} \theta^{\text{sup}} \\ \phi(d) \end{bmatrix} \\ \begin{bmatrix} \theta^{\text{sup}} \\ \phi(d) \end{bmatrix} &= \begin{bmatrix} \theta^{\text{sup}} + R_c I \\ \phi(d) \end{bmatrix} \\ \begin{bmatrix} \theta^{\text{inf}} \\ \phi(d) \end{bmatrix} &= \begin{bmatrix} A_2 & B_2 \\ C_2 & D_2 \end{bmatrix} \begin{bmatrix} \theta(1) \\ 0 \end{bmatrix} \end{aligned} \quad 3.12$$

$$I = \int_{x_1}^{x_2} \int_{y_1}^{y_2} \psi(x, y, d, p) \cos(\alpha x) \cos(\beta y) dx dy$$

where

$$A_i = D_i = \cosh(ud_i) \quad B_i = \frac{1}{u} \sinh(ud_i) \quad C_i = u \sinh(ud_i) \quad \text{for } i = 1, 2$$

where d_1 and d_2 are the thicknesses of the two layers of the sample.

A simpler and faster method to obtain a solution of the equations (3.12) is the perturbation method. In the following section, this approach is presented and analyzed.

3.4.2 Resolution of the forward problem: mathematical perturbations

The perturbation method consists of writing asymptotic series expansions of the variables θ and ϕ with respect to a small parameter in the model. These series expansions are then injected into set (3.12), and term-by-term identification of the coefficients of the successive powers of the small parameter leads to a coupled series of linear sets. These allow the calculation of the different components θ_i and ϕ_i . The mathematical formalism presented below is valid only for small values of the thermal contact resistance R_c . The asymptotic series expansions with respect to the small parameter R_c that will be noted ε from now on are

$$\begin{aligned}\theta(\alpha, \beta, z, p) &= \sum_{i=0}^{\infty} \theta_i(\alpha, \beta, z, p) \varepsilon^i \\ \phi(\alpha, \beta, z, p) &= \sum_{i=0}^{\infty} \phi_i(\alpha, \beta, z, p) \varepsilon^i\end{aligned}\tag{3.13}$$

Term-by-term identification of the coefficients of ε_n leads to the following quadrupole equations:

For ε_0 -order identification set (3.11) results in

$$\begin{bmatrix} \theta(0) \\ \frac{\sin(\alpha L_1)}{\alpha} \frac{\sin(\beta L_2)}{\beta} \end{bmatrix} = \begin{bmatrix} A_1 & B_1 \\ C_1 & D_1 \end{bmatrix} \begin{bmatrix} A_2 & B_2 \\ C_2 & D_2 \end{bmatrix} \begin{bmatrix} \theta_0(1) \\ 0 \end{bmatrix}\tag{3.14}$$

$$\psi_0(e_1) = \sinh(\sqrt{p}e_2) / \sinh(\sqrt{p})$$

For ε_1 -order identification set (3.12) turns out to be

$$\begin{aligned}\begin{bmatrix} \theta_1(0) \\ 0 \end{bmatrix} &= \begin{bmatrix} A_1 & B_1 \\ C_1 & D_1 \end{bmatrix} \begin{bmatrix} \theta^{\text{sup}} \\ \phi_1(d) \end{bmatrix} \\ \begin{bmatrix} \theta_1^{\text{sup}} \\ \phi_1(d) \end{bmatrix} &= \begin{bmatrix} \theta_1^{\text{inf}} + I_0 \\ \phi_1(d) \end{bmatrix} \\ \begin{bmatrix} \theta_1^{\text{inf}} \\ \phi_1(d) \end{bmatrix} &= \begin{bmatrix} A_2 & B_2 \\ C_2 & D_2 \end{bmatrix} \begin{bmatrix} \theta_1(1) \\ 0 \end{bmatrix}\end{aligned}\tag{3.15}$$

I_0 has the same definition as I in equation (3.12), just replacing ψ by ψ_0 . The substitution of ψ_0 defined by equation (3.14) into this definition allows the calculation of integral I_0 and therefore the solution of set (3.15).

The first-order temperature on the front face is given by:

$$\theta(0) = \frac{4}{\alpha\beta} K \frac{\sinh(ud_2) \sinh(\sqrt{p}d_2)}{\sinh(\sqrt{p}) \sinh(u)} \quad 3.16$$

where

$$K = \sin\left(\alpha \frac{x_2 - x_1}{2}\right) \cos\left(\alpha \frac{x_2 + x_1}{2}\right) \sin\left(\beta \frac{y_2 - y_1}{2}\right) \cos\left(\beta \frac{y_2 + y_1}{2}\right) \quad 3.17$$

Product of equation 3.16 by ε represent the Laplace–Fourier transforms $\Delta\theta = \varepsilon\theta_1$ of the contrast $\Delta T(x, y, z_s, t)$ on the front face. Return to the original (x, y, z_s, t) domain can be achieved numerically by using fast Fourier-transform (FFT) and Stehfest algorithms [108].

Let us remind that the modelling described previously is based on the assumption of an adiabatic heat transfer. In reality, nondestructive experiments are always affected by heat losses. However, as reported in the literature [109], the losses effect on thermal contrasts are very small. This last result is a consequence of the nature of the thermal contrast itself: even if each surface temperature T and T_0 might be strongly affected by heat losses, their difference, $T = T - T_0$, leads in general to a compensation for this effect.

Numerical simulations have been carried out in a previous work [106] to assess the effectiveness of the above model. The simulations have shown that the perturbed contrast profiles are in excellent agreement with the true ones for small thermal resistance values, with $\varepsilon \leq 0.3$. However, for higher resistances ($\varepsilon > 0.3$) the approximation is no longer appropriate, confirming the restriction of the above model to weak anomalies or defects.

We can observe, that in the case of anomaly represented by a plane of vessels, characteristic of a plane angioma, this condition is accomplished.

In fact, in the case of a plane of vessels thick $h_v=200 \mu\text{m}$, inside a tissue thick $h_t \cong 1.5 \text{ mm}$ (maximum depth of laser interaction in a biological tissue for a wavelength $\lambda=595 \text{ nm}$) with a thermal conductivity for the plane of vessels and for the tissue respectively of $k_v=0.492 \cdot 10^{-8} \text{ W m}^{-1} \text{ K}^{-1}$, $k_t=0.322 \cdot 10^{-8} \text{ W m}^{-1} \text{ K}^{-1}$, the normalized thermal resistance ε is given by

$$\varepsilon = \frac{h_v}{h_t} \frac{k_t}{k_v} = 0.087 < 0.3 \quad 3.18$$

In the following sections, it is described the inversion procedures that allow the evaluation of the depth and the thickness of the subsurface plane of vessels. These parameters are directly derived from the perturbation 3D modelling described in this section.

3.4.3 Evaluation of the depth

In this section, it is shown how the depth of the anomaly can be derived from the space averaging of the Laplace contrast profile $\tau(x, y, z_s, p)$.

The space average of the Laplace contrast is defined as

$$\Delta\tau = \int_0^{L_1} \int_0^{L_2} \Delta\tau(x, y, z_s, p) dx dy \quad 3.19$$

where $\Delta\tau$ is the difference between the Laplace transform of the temperature on one spot of the face of the sample and its value in the absence of anomalies. With the previous firstorder perturbation method, the integral in the right-hand side of equation (3.19) is equal to $\varepsilon\theta_1(0, 0, z_s, p)$. In the case of expansive plane of vassels $ab/L_1L_2=1$. The application of equation (3.16) allows the calculation of $\Delta\tau$ for the front face:

$$\Delta\tau(0, p) = \varepsilon \frac{\sinh^2(\sqrt{p}(1-d))}{\sinh^2(\sqrt{p})} \quad 3.20$$

Equation (3.20) written for two values p_1 and $p_2=4p_1$ yields the analytical elimination of the unknown parameters ε and. If m_1 and m_2 are the experimental average Laplace contrasts on the front face, the depth d of the flaw is the solution of the following equation:

$$\cosh(\sqrt{p_1}(1-d)) = \left(\frac{m_2}{m_1}\right)^{1/2} \cosh(\sqrt{p_1}) \quad 3.21$$

where

$$m_i = \Delta\tau(x, y, 0, p_i) \quad \text{and} \quad i = 1, 2$$

This equation leads to the following estimation of the anomaly depth:

$$d = 1 - \frac{1}{\sqrt{p_1}} \ln \left[\left(\frac{m_2}{m_1}\right)^{1/2} \cosh(\sqrt{p_1}) + \left(\frac{m_2}{m_1} \cosh^2(\sqrt{p_1}) - 1\right)^{1/2} \right] \quad 3.22$$

3.4.4 Evaluation of the thickness

In this section, it is shown how the thickness of the anomaly can be derived from the space averaging of the Laplace contrast profile $\tau(x, y, z_s, p)$, if the depth of the anomaly d has been already calculated. The thermal contact resistance per surface unit is defined as the ratio of the anomaly thickness h_v and its thermal conductivity k_v , $\varepsilon = h_v / k_v$. In case of anomaly represented by plane of blood vessels, k_v is simply the thermal conductivity of the blood, which is a known parameter. Evaluation of the thickness h_v is therefore equivalent to the estimation of its thermal resistance, ε .

The equation (3.20) shows that the average Laplace contrast (and therefore the instantaneous averaged contrast $\Delta\tau$) is proportional to the thermal resistance ε of the flaw. In other words, the average Laplace contrast is proportional to the thickness of the plane of vessels.

Equation 3.20 depends on two unknowns: the thermal resistance ε , and the depth d . If it is written for two values p_1 and $p_2 = 4p_1$ of the Laplace variable, the parameter d can then be eliminated from the two corresponding equations by using the duplication properties of the hyperbolic functions. If m_1 and m_2 are the experimental Laplace contrasts on the front face at the centre of the flaw, the thermal resistance of the plane of vessels is given by the following equation:

$$\varepsilon = \frac{m_1^2 \sinh^2(\sqrt{p_1}) \tanh(\sqrt{p_1})}{m_2 \cosh(\sqrt{p_1}) - m_1} \quad 3.23$$

where

$$m_i = \Delta\tau(x_c, y_c, 0, p_i) \quad \text{and} \quad i = 1, 2$$

3.4.5 Statistical analysis of the accuracy of the inversion procedures

Any inversion algorithm produces estimated parameters. A measurement of the quality of the inversion requires a quantification of the estimation error that has been made. This error can be divided into two parts: the error caused by measurement noise, and the error caused by performing the quadratures in time to calculate the Laplace transform and in space to calculate the average Laplace contrast, on a limited number of points. In the following, this second error will be neglected since the numbers of points, in time and space, used to perform the quadratures are considered large enough. Using a stochastic analysis with the assumptions that the noise on the thermal contrast ΔT is additive, uncorrelated and of constant standard deviation σ , it is possible to quantify the inversion errors caused by measurement noise. The effects of measurement noise on the precision of the thermal resistance and depth are represented by the variance equations 3.24 and 3.25

$$\sigma_\varepsilon^2 = \varepsilon^2 \sigma^2 \Delta t (UV) \begin{pmatrix} \frac{1}{2p_1} & \frac{1}{p_1 + p_2} \\ \frac{1}{p_1 + p_2} & \frac{1}{2p_1} \end{pmatrix} \begin{pmatrix} U_1 \\ V_1 \end{pmatrix} \quad \begin{aligned} U_1 &= \frac{-m_1 + 2m_2 \cosh(\sqrt{p_1})}{m_1 [1 + m_1 \sqrt{p_1} \sinh(\sqrt{p_1})] [-m_1 + m_2 \cosh(\sqrt{p_1})]} \\ V_1 &= \frac{[1 + m_1 \sqrt{p_1} \sinh(\sqrt{p_1})] \cosh(\sqrt{p_1})}{[1 + m_2 \sqrt{p_1} \sinh(\sqrt{p_2})] [-m_1 + m_2 \cosh(\sqrt{p_1})]} \end{aligned} \quad 3.24$$

$$\sigma_d^2 = \frac{\sigma^2 \Delta t}{4NM\varepsilon^2} \frac{1}{p_1} \left\{ \cosh(\sqrt{p}(1-d)) \left(1 + \frac{\cosh(\sqrt{p}(1-d))}{|\exp(\sqrt{p_1}(1-d)) - \cosh(\sqrt{p}(1-d))|} \right) \exp(-\sqrt{p_1}(1-d)) \right\}^2 \begin{pmatrix} U_2 \\ V_2 \end{pmatrix} \quad \begin{aligned} U_2 &= \frac{\sinh^4(\sqrt{p_1})}{2p_1 \sinh^4(\sqrt{p_1}(1-d))} + \frac{\sinh^4(\sqrt{p_2})}{2p_2 \sinh^4(\sqrt{p_2}(1-d))} \\ V_2 &= -\frac{2 \sinh^2(\sqrt{p_1}) \sinh^2(\sqrt{p_2})}{(p_1 + p_2) \sinh^2(\sqrt{p_1}(1-d)) \sinh^2(\sqrt{p_2}(1-d))} \end{aligned} \quad 3.25$$

In figure 3.2, the relative standard deviation, $\sigma_\varepsilon/\varepsilon$, σ_d/d , of the thermal resistance and of the depth are reported as a function of the Laplace variable p ($= p_1$) for different values of the anomaly depth. In the figure 3.2 the value d_l refers to maximum length of laser interaction in the tissue ($\cong 1.5$ mm for a laser wavelength $\lambda=595$ nm). With regard to the other parameters in equations 3.24 and 3.25, we used a standard deviation of the normalized ΔT contrast $\sigma = 0.1$,

a normalized time step $\Delta t = 4 \times 10^{-3}$ that corresponds a scan rate of 40 ms, a normalized thermal resistance $\varepsilon = 0.087$, the numbers M and N are both 256.

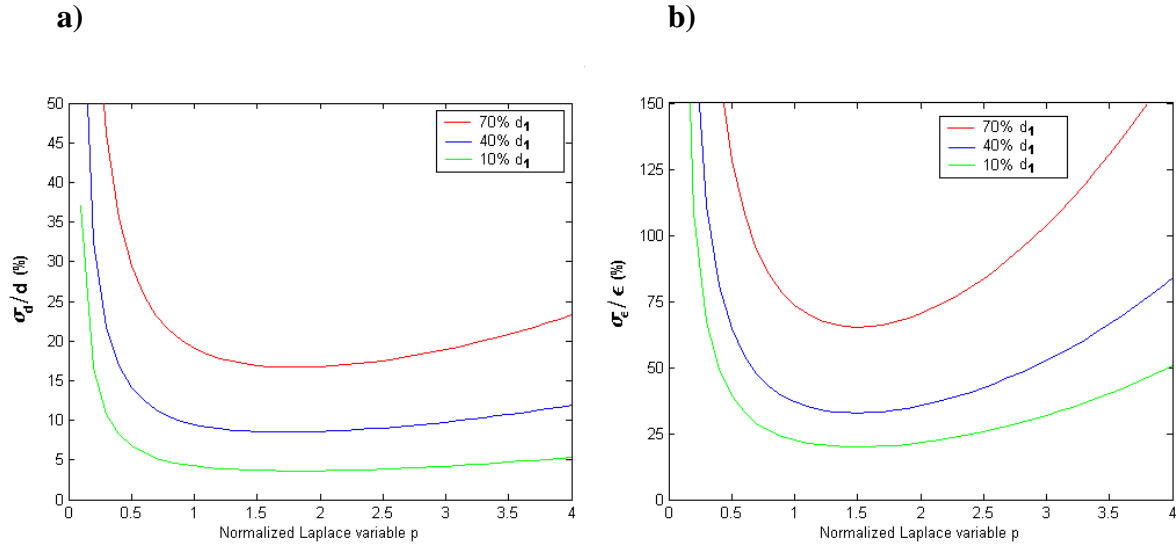


Fig. 3.2: relative standard deviation as a function of the Laplace variable p ($= p_1$) for different values of the anomaly depth. a) σ_d/d for the depth, b) $\sigma_\varepsilon/\varepsilon$ for the thermal resistance

We can note from the figures that:

From fig. 3.2.a

- 1) The choice of the optimum p -value depends on the depth d , but it is always in the range 1–2 for deep anomalies.
- 2) A bad choice of p leads only to a small error on the precision for plane of vessels located near the heated surface, whereas for deeper plane of vessels, the discrepancies are higher.
- 3) For the deep anomaly the error can changes from 3% for $d = 0.1d_1$ up to 20% for $d = 0.7d_1$.
- 4) the estimation error changes nonlinearly with the Laplace variable p and the flaw depth d .

From fig. 3.2.b

- 1) The optimum p -value that should be used for thermal resistance inversion independently from the anomaly depth must be within the range 1–2.
- 2) The estimation of the thermal resistance is better for more superficial plane of vessels, for optimum p -values the error changes from 25% for $d = 0.1d_1$ up to 75% for $d = 0.7d_1$.

3.5 Numerical simulation: biometric heat transfer model

The morphological informations, obtained for different plane of vessels with PT approach, have been used as input data for a numerical simulation based on a *biometric heat transfer model*. This model describes heat transfer in the vicinity of a large plane of vessels proximal to the skin. The mathematical problem is to retrieve the unknown spatial and temporal temperature profiles associated with a specific multi-layer biological structure and for a given set of laser parameters. It is assumed that the vessels act as a volumetric heat source for the surrounding four-layer tissue structure. These layers are successively, in positive z direction, the epidermis, the dermis, the plane of vessels, and the dermis again (core).

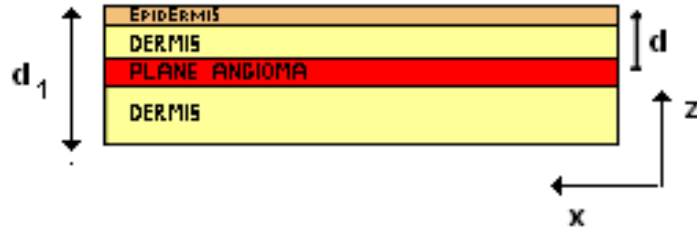


Fig. 3.3: *Multilayer biological tissue*

It has been also assumed that each layer is isotropic with respect to thermal conductivity $k(z)$, metabolic heat rate q^M , density ρ , and specific heat c of the tissue. The heat effect of the vessels on the skin temperature depends on the *vessel's location (depth)* and from its *thickness* as well as the *blood flow speed* and *temperature*. The plane of vessels can be considered a single large vessel running along the x direction without traversing across the z direction (see Figure 3.3). The thermal conduction in the tissue surrounding the plane of vessel is dominant in directions parallel (x) and perpendicular (z) to the skin. We can neglect heat transfer along the (y) axis because of the presence of other vessels, periodically arranged and similar to that considered. Therefore, the 2D + 1 model assumes the following form:

$$\rho c \frac{\partial T}{\partial t} - \frac{\partial}{\partial x} \left(k(z) \frac{\partial T}{\partial x} \right) - \frac{\partial}{\partial z} \left(k(z) \frac{\partial T}{\partial z} \right) = q^{BL}(x, t) + q^M(x, z) + q^L(x, z) \quad 3.26$$

where q^L is the heat from the laser source, q^M is the volumetric metabolic heat, q^{BL} is the heat due to mean blood flow speed u_{BL} in the plane of vessels, $k(z)$ is the thermal conductivity of a particular layer, while ρ and c are the tissue density and specific heat respectively. In the model, the following boundary conditions are used:

$$\begin{aligned}
T(x, D, t) &= T_{core} \quad x \in (0, L) \\
T(x, 0, t) &= T_{epidermis}(x, t) \quad x \in (0, L) \\
\frac{\partial T(x, 0, t)}{\partial z} &= \lambda(T(x, 0, t) - T_{air}) + q_{ir} \quad x \in (0, L) \\
\frac{\partial T(0/L, z, t)}{\partial x} &= 0 \quad z \in (0, D)
\end{aligned} \tag{3.27}$$

λ is the convection heat transfer coefficient, which depends on air flow. According to [110]: $\lambda = 2.7 + 7.4 (v_{air})^{0.67}$ ($W/m^2 K$), where v_{air} is the air speed in (m/s), q_{ir} is the radiation heat flux: $q_{ir} = \sigma \epsilon (T_{epi}^4 - T_{air}^4)$, where σ is the Stefan-Boltzmann constant and ϵ is the skin emissivity. The heat source term associated with blood flow is assumed to have the decomposition $q^{BL} = u_{BL}(t)r(x, z)$, where u_{BL} is the unknown blood flow speed in the plane of vessels and $r(x, z)$ the modified bell function:

$$r(x, z) = \mu \exp\left(-\frac{(z-d)^2}{\pi h_v^2}\right) \tag{3.28}$$

h_v is the thickness of the plane of vessels seen as a heat source. μ is defined as follows:

$$\mu = \rho_{BL} c_{BL} \frac{A}{V} (T_{vessels}(x, z, t) - T(x, z, t)) \tag{3.29}$$

where ρ_{BL} and c_{BL} are the density and the specific heat of blood respectively, A is the vessels cross section, and V is the control volume of tissue. We assume that the early temperature of the blood in the vessels is the same as the core (dermis) temperature $T_{vessels} = T_{dermis}$.

The heat source term associated with laser source is assumed to have a gaussian expression

$$\begin{cases} q^L = q_0 e^{-\alpha(z)z} e^{-(x/w(z))^2} & 0 < t \leq t_p \\ q^L = 0 & t > t_p \end{cases} \quad 3.30$$

with

$$\alpha = \alpha_a + \alpha_s(1-g) \quad w(z)^2 = w_0^2 \left(1 + \left(\frac{z\lambda}{\pi w_0^2} \right)^2 \right)$$

Where q_0 is the central maximum depending on the laser fluence, α is the total attenuation coefficient depending on the biological layer, α_a is the absorption coefficient, α_s is the scattering coefficient, g is the anisotropy coefficient, $w(z)$ is the waist size, w_0 is the half-spot diameter, λ is the laser wavelength and t_p is the pulse period.

In constructing this model, it has been assumed that there isn't heat flux between the domain of interest $(0, L) \times (0, D)$ with the rest of the body. This problem is well posed and has a unique continuous solution. The solution is C^1 but has second order derivative in the z direction with finite jump at the line of discontinuities $z = C^t$ of the thermal conductivity k .

3.5.1 Model Computation

In order to obtain a direct simulation of the model it has been used a Finite Volume (**FV**) approximation with centered cells of size $h_x \times h_z$ on a regular space grid.

The *finite volume method* is one of the methods used for representing and evaluating partial differential equations in the form of algebraic equations. In this method the values are calculated at discrete places on a meshed geometry. "Finite volume" refers to the small volume surrounding each node point on a mesh. In the finite volume method, volume integrals in a partial differential equation that contain a divergence term are converted to surface integrals, using the divergence theorem. These terms are then evaluated as fluxes at the surfaces of each finite volume. Because the flux entering a given volume is identical to that leaving the adjacent volume, these methods are conservative. The main advantage of the finite volume method is that it is easily formulated to allow for unstructured and dishomogeneous meshes (structures).

Let us denote $T_{i,j}$ the average value T of in the centered **FV** cells. The discrete version of equation (3.26) is:

$$T_{i,j}^{n+1} \Delta x \Delta z - T_{i,j}^n \Delta x \Delta z - \frac{\Delta t \Delta z}{\rho_{BL} c_{BL}} (\Phi_{i+1/2,j}^{n+1} - \Phi_{i-1/2,j}^{n+1}) - \frac{\Delta t \Delta x}{\rho_{BL} c_{BL}} (\Phi_{i,j+1/2}^{n+1} - \Phi_{i,j-1/2}^{n+1}) = \frac{\Delta t \Delta x \Delta z}{\rho_{BL} c_{BL}} \left[(\mu u_{BL}) (1 - T_{i,j}^{n+1}) \exp \left(-\frac{(z_j - h)^2}{\pi D_{VASO}^2} \right) + q_0 e^{-\sigma(z)z} e^{-(x/w(z))^2} + q^M \right] \quad 3.31$$

In the cell centred in (x_i, z_j) ,

$$\begin{aligned} x_i &= h_x / 2 + \frac{i-1}{N_x - 1} h_x \quad i = 1..N_x \\ z_j &= h_z / 2 + \frac{j-1}{N_z - 1} h_z \quad j = 1..N_z \end{aligned} \quad 3.32$$

The heat flux values at the wall of the cells are approximated with :

$$\begin{aligned} \phi_{i+1/2, j} &= k_{i+1/2, j} \frac{T_{i+1, j} - T_{i, j}}{h_x} \quad i = 1..N_x - 1 \\ \phi_{i, j+1/2} &= k_{i, j+1/2} \frac{T_{i, j+1} - T_{i, j}}{h_z} \quad j = 1..N_z - 1 \end{aligned} \quad 3.33$$

and

$$\begin{aligned} k_{i+1/2, j} &= \frac{1}{2} (k_{i+1, j} + k_{i, j}) \\ k_{i, j+1/2} &= \frac{1}{2} (k_{i, j+1} + k_{i, j}) \end{aligned} \quad 3.34$$

Where, in the equation (3.31), $T_{i, j}^n$ denotes the temperature at time ndt .

Using the boundary conditions on Φ and T we obtain a classic linear system:

$$MT^{h_x, h_z} = \delta^{h_x, h_z} \quad 3.35$$

At each time step we have to solve a linear system to obtain $T^{n+1}(x, z)$. M is pentadiagonal matrix of size $(N_x \times N_z)^2$. T^{h_x, h_z} is a matrix of size $N_x \times N_z$ reshaped from the 2D unknown solution's array $(T_{i, j})$, $i=1..N_x$, $j=1..N_z$ column-wise or row-wise. The grid computation is fixed to $N_x=N_z=64$ and the time step is of the order of 1/20 which corresponds to the time step between two frames in our thermal camera.

The numerical computations have been realized using the Matlab 6.5 code. The main thermal and optical constants used in the simulations, for the biological tissues, will be showed in the next chapter.

Chapter 4

EXPERIMENTAL AND NUMERICAL RESULTS

4.1 Introduction

In this last chapter it will be shown results obtained through the monitoring of patients affected by plane angioma in the facial region. After a description of the instruments used (laser system and infrared camera) and of the operative protocol realized the main results will be presented, confirming the great contribute of our methodological approach.

First of all, in order to emphasize the thermal behaviours associated to different facial region, some preliminaries evaluations relative to temperatures and temporal dynamics found will be illustrated. Subsequently, results obtained on different patients applying the approach described in the previous chapter will be showed and discussed. Particularly, thanks to the pulsed thermography model, depth and thickness relative to different plane of vessels have been estimated and in each different clinical situations numerical simulations have been run.

Experimental and numerical values will be analyzed and compared. Starting from this results, some set of laser parameters relative to plane angioma characterized by specific depth and thickness, will be proposed. The chapter is completed with a discussion relative to some limit conditions for laser treatment application on plane angioma pathology.

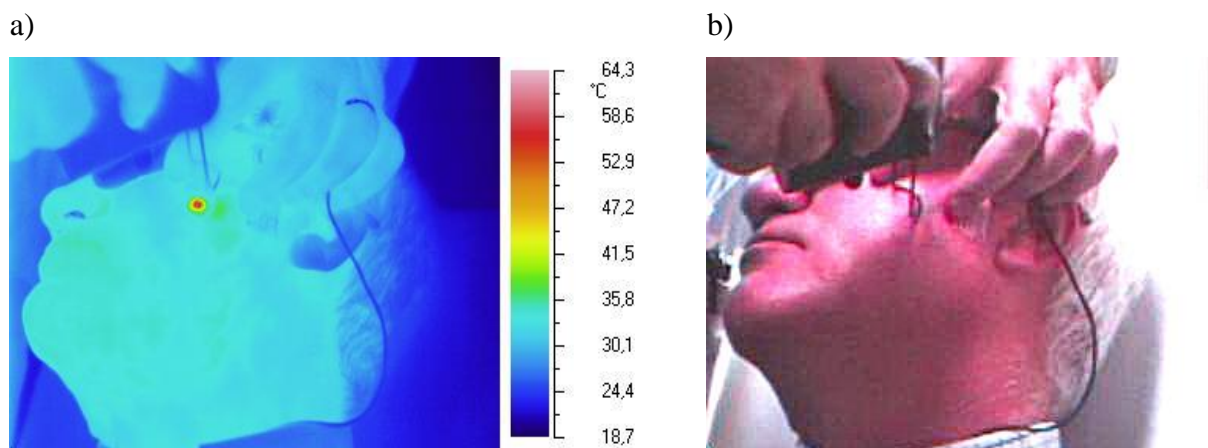


Fig 4.1 : Example of laser treatment on patient with plane angioma: a) infrared image, b) visible image.

4.2 Materials and method

In the experimental activity of this work, the laser treatments on 26 patients affected by plane angioma have been monitored. The 26 patients were 17 male and 9 female with age in the range 20-50. In order to study an homogeneous sample group we monitored all patients with a plane angioma in the facial region. In the majority of cases, the angioma was widespread in different facial region and principally on cheek, nose and temple.

The laser therapy is applied in photothermal regime using the selective photothermolysis principle. The laser system used has been Pulsed Dye Laser – Deka Dermobeam 2000 with characteristics showed in fig 4.2

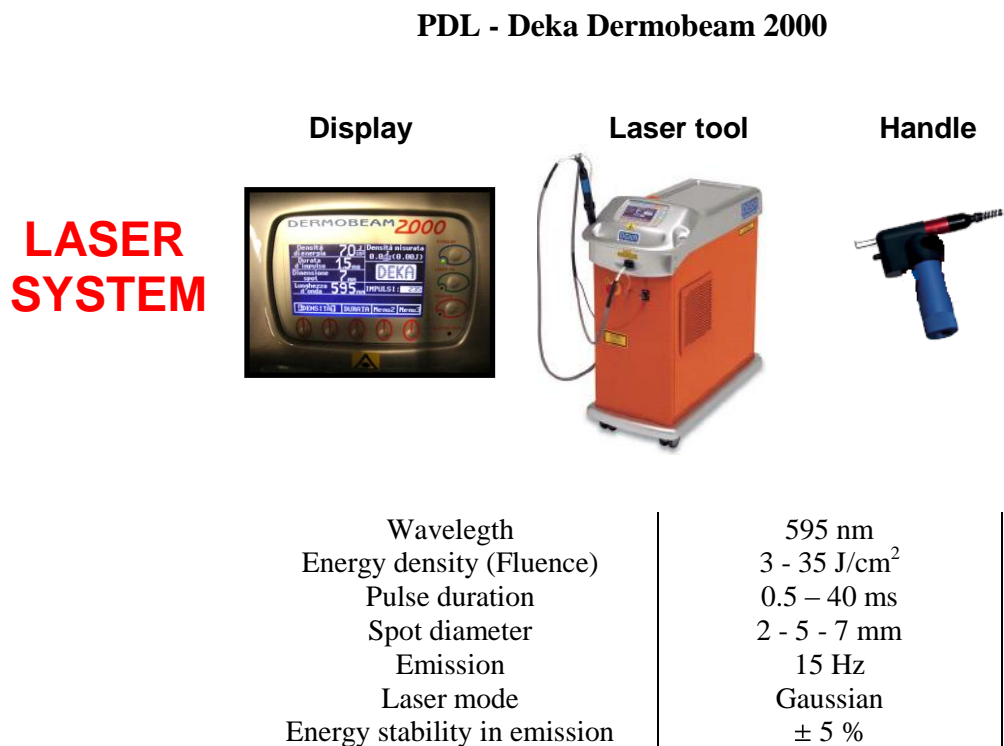


Fig 4.2 : Main characteristics of the Pulsed Dye Laser – Deka Dermobeam 2000

As described in chapter 1, being haemoglobin the most relevant chromophore in vascular pathologies, the Dye laser naturally becomes the elective therapeutic tool by selective absorption. In fact, as it is possible to see from figure 1.3, the emission wavelength of this laser

(595 nm) is very close to the absorption peak of the target (haemoglobin) as required from selective photothermolysis principle.

The infrared acquisition has been performed by means of two different digital thermal Camera: a Land FTI6 - HgCdTe camera used in preliminaries evaluation and a more performed Avio TVS 500 – microbolometer camera used in the whole study. The main characteristics of the cameras are showed in the fig. 4.3. Particularly, for the Avio camera the acquisition spectral band is within 8-14µm, the time resolution is 0.02 s, and the temperature sensitivity is 0.06 K.



Fig 4.3 : Main characteristics of the infrared cameras employed

Black body correction has been executed to evaluate and to correct drift and shift effects due to the infrared camera at the beginning of each measurement session. Emissivity of the skin has been estimated as $\epsilon = 0.95$. In the next pictures the system and laser therapy ambulatory are shown:

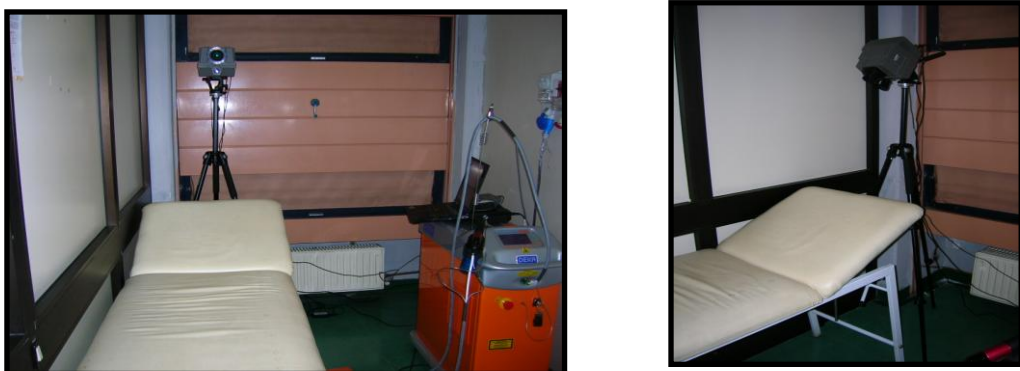


Fig 4.4 : Laser therapy ambulatory: infrared camera and laser tool

The medical protocol commonly used for the treatment of patients with plane angioma pathology by the physician is the following:

- He chooses the area of the angioma that he wants to treat (of dimension about 5x5 cm)
- He defines the laser parameters (usually, starting from referential laser parameters in tab. 3.1)
- He covers the area chosen with single laser pulses with an interval of 2-4 s

Particularly, in the covering of the area of the patient the physician lays a pulse upon the other of about 20 % of spot diameter in order to reduce dischromic effects.

In order to apply the operative approach described in the previous chapter, the next procedure has been performed sequentially:

- Acclimatization of the subject in the therapy rooms for a time not less than 15 minutes
- The anatomic facial region of interest has been cleaned with alcohol in order to remove sweat, cosmetics, dust and others
- A single pulse with referential laser parameters has been applied in the middle of the region of interest
- An infrared recording of the region under investigation has been made continuously some seconds before, during and after (for a time of about 30 s) the laser pulse.

The laser therapy room has been thermostated at 24 ± 0.5 °C during the measurement. The umidity was about 60%.

This procedure has permitted the registration of the thermal behaviour of the specific anatomic region under laser-interaction: temperature and its temporal evolution (thermal recovery). Subsequently, each information has been analyzed with the PT model and with the numerical simulation described in chapter 3. In the next sections the results achieved will be showed and discussed starting from some preliminaries evaluations. For the data and numerical analysis, self-implemented software has been realized with a MATLAB platform.

4.3 Preliminary results and observations

The first step was aimed to evaluate the thermal responses of different parts of the skin illuminated by laser power. In this section, some graphics of thermal response relative to representatives cases, extrapolated from the monitoring on all patients, are reported with the intent of emphasizing the main results obtained from these preliminaries evaluation. All graphics reported in this section refer to a set of referential laser parameters shown in the next table:

Referential laser parameters	
Wavelength	595 nm
Energy density	7 J/cm ²
Pulse duration	1.5 ms
Spot diameter	7 mm

Tab. 4.1 : Set of laser parameters used in the preliminaries monitoring

In the first graph temperatures obtained in a specific anatomic region after a single laser pulse are compared for different patients

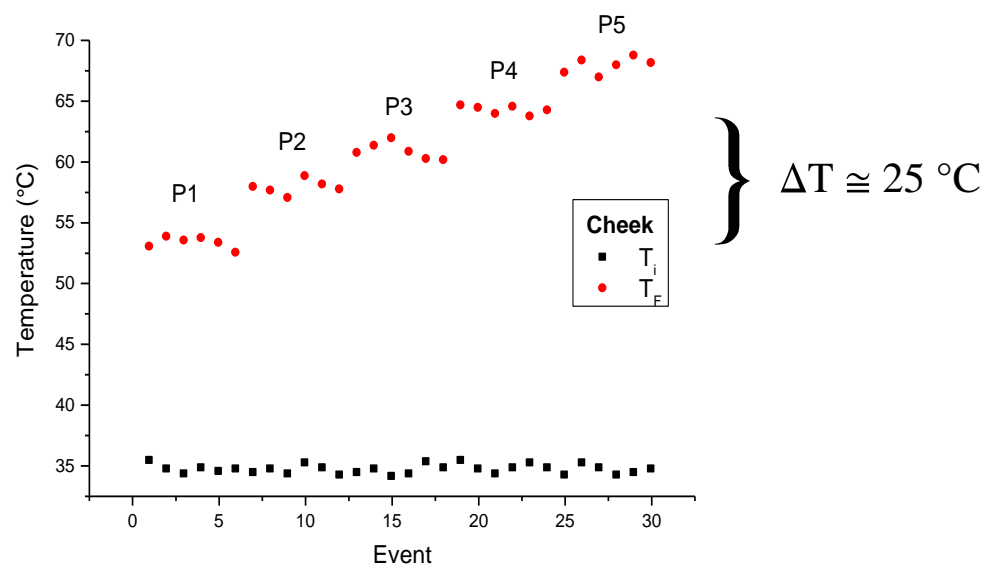


Fig. 4.5 : Temperatures obtained after laser pulse referred to cheek region

In the graph with black and red point we indicated the initial and final temperatures recorded before and after the laser pulse respectively. The evaluations refer to the same facial region affected by plane angioma (cheek) for 5 different patients (from P1 to P5). For each patient six thermal response associated to laser parameters in table 4.1 are graphicated.

As it is possible to observe, even if the initial temperatures are quite similar for all patients (physiological temperature), the final temperature, obtained immediately after the pulse, can be very different.

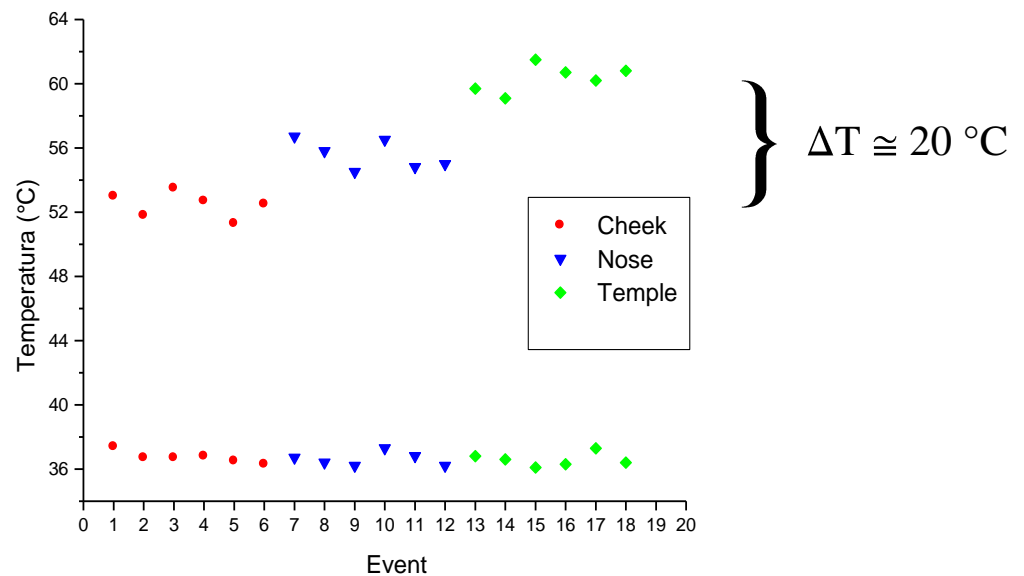


Fig. 4.6 : *Temperatures obtained after laser pulse referred to cheek region*

Similar situation has been found for the thermal response obtained in different facial region of a same patient affected by plane angioma. In general, from the evaluations performed on all patients it has been found with the same laser parameters, on a same patient and in presence of the same pathology, that the ΔT among different anatomics regions can be higher than 15-20 °C. For example, fig. 4.6 which refers to a patient affected by widespread plane angioma, shows how the temperature obtained immediately after the pulse can change from about 52 °C on the cheek to 64 °C on the temple.

However, both fig. 4.5 and 4.6, for a same patient in a same facial region show a good repetitions of the temperatures measured. The temporal evolutions of the temperature after the laser pulse has been recorded and analyzed also for different anatomics regions. In general, this dynamic depends on the region under investigation. Fig. 4.3 shows how each anatomic region of the face (of a same patients) is characterized from a different recovery time (T_r).

The recovery time is defined as the time occurring by the tissue for recovering the 70% of the induced thermal gap.

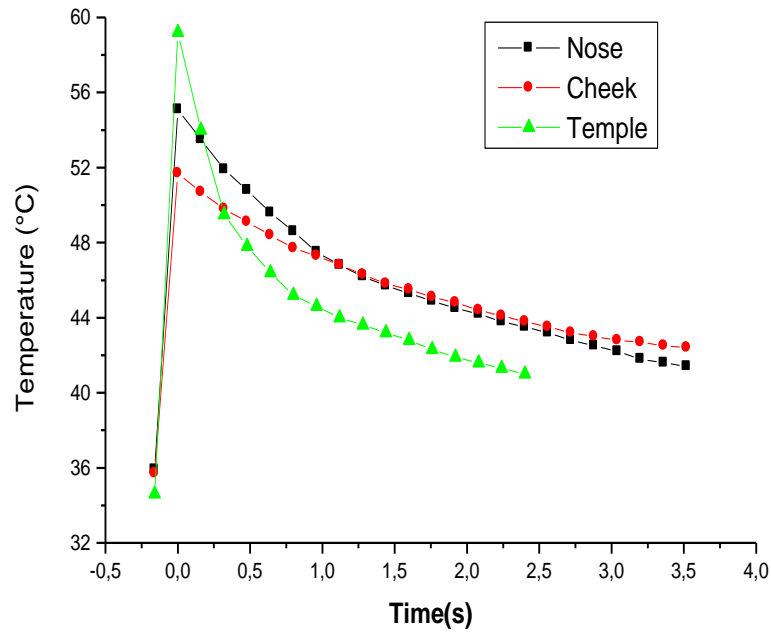


Fig. 4.7 : Temporal evolutions of the temperature after a laser pulse in three region of the face

This dependence has been found in each patient with widespread plane angioma where it has been possible to realize evaluations in different regions affected by pathology. In next table the average recovery times evaluated on three facial region are reported

Recovery time for differents facial regions	
Region	Tr (s)
Temple	2.4 ± 0.5
Nose	4.1 ± 0.6
Cheek	6.2 ± 0.6

Tab. 4.2 : Mean values of the recovery time estimated in three different facial regions

The data in table 4.2 refer to mean values obtained on all recovery time estimated in the temporal evolutions recorded.

As well as for the temperatures, when the analysis is focused on a same patients in a same anatomic region a good repeatability of the dynamics has been found. In fig. 4.8 temporal rate of the temperature referred to the cheek of a patient and estrapolated from a recorded laser treatment are reported.

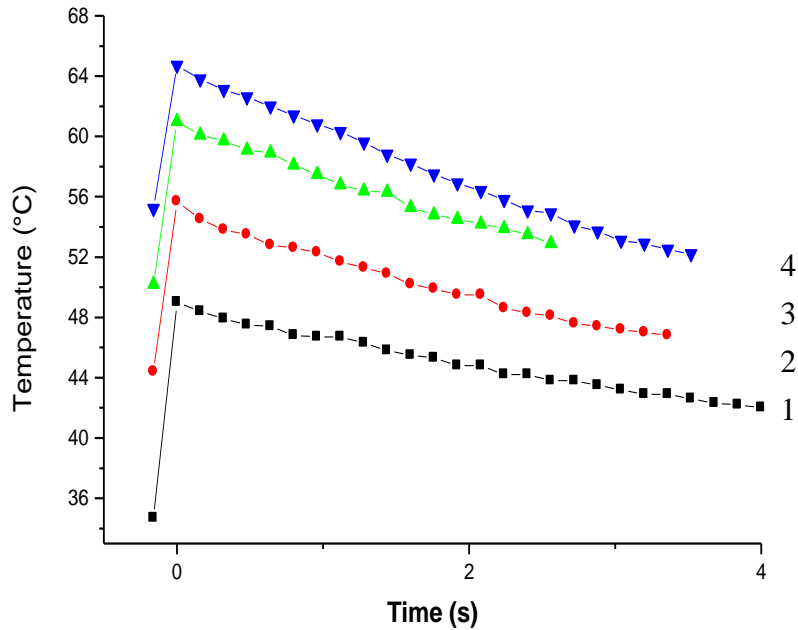


Fig. 4.8: Temporal rate of the temperature referred to the cheek of a patient after application of laser pulses

The graph shows four dynamics associated to four single laser pulse made in sequence on four neighbouring points of the tissue. The pulses are numerated from 1 to 4 in temporal order.

As it is possible to note all temporal rate reported are quite similar. In the graph, the initial temperatures referred to the dynamics are different. This is due to the thermal superimposition effect present when the time awaited between two successive pulse is lower than the time spent from the tissue for a complete recovery.

All evaluations shown since here, emphasise how the thermal behaviours of the tissue achieved under laser treatment for a given set of laser parameteres, depend on the specific target. Particularly, they can differ from region to region and from patient to patient.

It is important remember, as it has been discussed in chapter 1 that in photothermal interaction regime, the temperature induced to the tissue is strictly linked to hystological modification

obtained. Therefore, these preliminary results point out how with the same laser parameters, changing patient or anatomic region, the effects and so the therapeutic efficiency obtained can greatly differ, changing from optimal therapeutic results to unwanted harmful effects (for instance scars formation). These observations justify and confirm that if not using specific and tailored laser parameters for each different clinical situation the laser treatments on plane angioma pathology permits an optimal improvement just in a small number of patients, as discussed in the section 3.3. Starting from this observations, in order to improve the therapeutic efficiency and the safety in the laser therapy, the request of optimized set of laser parameters, for each specific treatment, becomes a necessity. With this intent the operative approach, object of this thesis work and described in previous chapters, has been performed and the main results achieved will be shown and discussed in the next section.

4.4 Pulsed Thermography model: experimental results

The operative procedure described in the section 4.2 has been applied to all patients in the anatomics regions of the face where the angioma was present. In this regions, the temporal evolution of the temperature achieved after a laser pulse has been recorded for each clinical situation. Successively, the recorded dynamics have been analyzed with the pulsed thermography model described in the section 3.4. For each patient through this model the depth and thickness of the plane of vessels associated to plane angioma in the region under treatment has been estimated . The results obtained for each patients are shown in table 4.3

Patient	Region	Depth (μm)	Thickness (μm)	Patient	Region	Depth (μm)	Thickness (μm)
1	cheek	210 ± 10	80 ± 20	14	cheek	660 ± 100	240 ± 130
	temple	120 ± 10	80 ± 20		temple	390 ± 40	160 ± 60
	nose	150 ± 10	70 ± 20		nose	450 ± 40	220 ± 120
2	cheek	310 ± 30	110 ± 40	15	cheek	630 ± 100	340 ± 240
	temple	160 ± 10	70 ± 20		temple	510 ± 80	220 ± 120
3	cheek	170 ± 10	70 ± 20	16	cheek	600 ± 90	310 ± 210
	nose	140 ± 10	80 ± 20		nose	540 ± 80	180 ± 70
4	cheek	550 ± 80	230 ± 130	17	cheek	730 ± 110	340 ± 240
	temple	520 ± 80	150 ± 60		temple	410 ± 40	180 ± 70
5	cheek	410 ± 40	160 ± 60		nose	480 ± 40	250 ± 130
	temple	320 ± 30	130 ± 50	18	cheek	610 ± 90	110 ± 40
	nose	330 ± 30	150 ± 60		temple	530 ± 80	260 ± 140
6	cheek	570 ± 80	210 ± 120	19	cheek	590 ± 90	180 ± 70
7	cheek	800 ± 160	320 ± 220		temple	320 ± 30	160 ± 60
	nose	670 ± 100	340 ± 240		nose	520 ± 80	230 ± 120
8	cheek	595 ± 90	250 ± 130	20	cheek	900 ± 180	370 ± 250
	temple	210 ± 10	90 ± 20		temple	770 ± 150	310 ± 210
9	cheek	350 ± 30	310 ± 210	21	cheek	230 ± 10	80 ± 20
	temple	310 ± 30	90 ± 20	22	cheek	520 ± 80	240 ± 130
	nose	330 ± 30	170 ± 70		temple	330 ± 30	130 ± 50
10	cheek	265 ± 20	160 ± 60	23	nose	510 ± 80	210 ± 110
	temple	160 ± 10	90 ± 20		cheek	420 ± 40	160 ± 60
	nose	190 ± 10	110 ± 40	24	cheek	810 ± 160	280 ± 150
11	cheek	430 ± 40	220 ± 120		temple	270 ± 20	140 ± 50
	temple	260 ± 20	80 ± 20		nose	720 ± 140	330 ± 230
	nose	400 ± 40	180 ± 70	25	cheek	780 ± 150	280 ± 150
12	cheek	470 ± 40	140 ± 50		temple	240 ± 20	90 ± 20
13	cheek	780 ± 160	270 ± 140		nose	710 ± 140	310 ± 210
	temple	220 ± 10	90 ± 20	26	cheek	490 ± 40	120 ± 50
	nose	470 ± 40	250 ± 130		nose	510 ± 80	120 ± 50

Tab. 4.3: Depth and thickness of the plane of vessels evaluated with the PT model

The evaluations in table 4.3 refer to mean values achieved on 5 different measurement. As it is possible to see from the table, the majority of patients were affected from a plane angioma widespread in more region of the face. In the next histograms the values for the depth and thickness of the angioma are reported without distinction of the anatomic region.

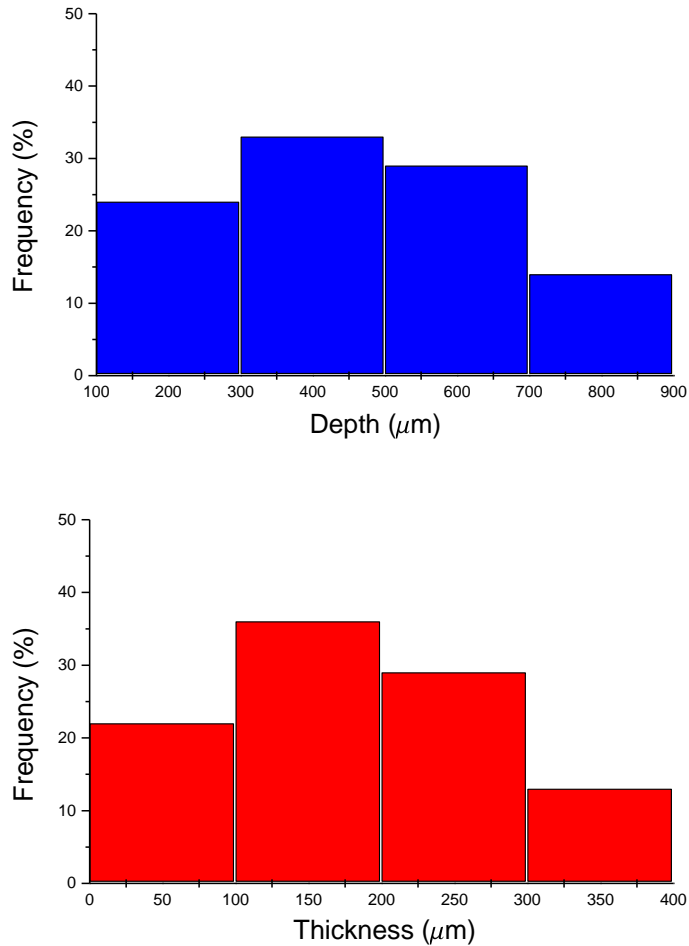


Fig. 4.9: Distributions relative to the depth and thickness evaluated globally on all anatomic facial region

As it is possible to note, the depth estimated mainly changes in the range from 300 μm to 700 μm while the thickness changes from 100 μm to 300 μm. Despite the previous case, in the next histograms the results refer to single anatomic facial region.

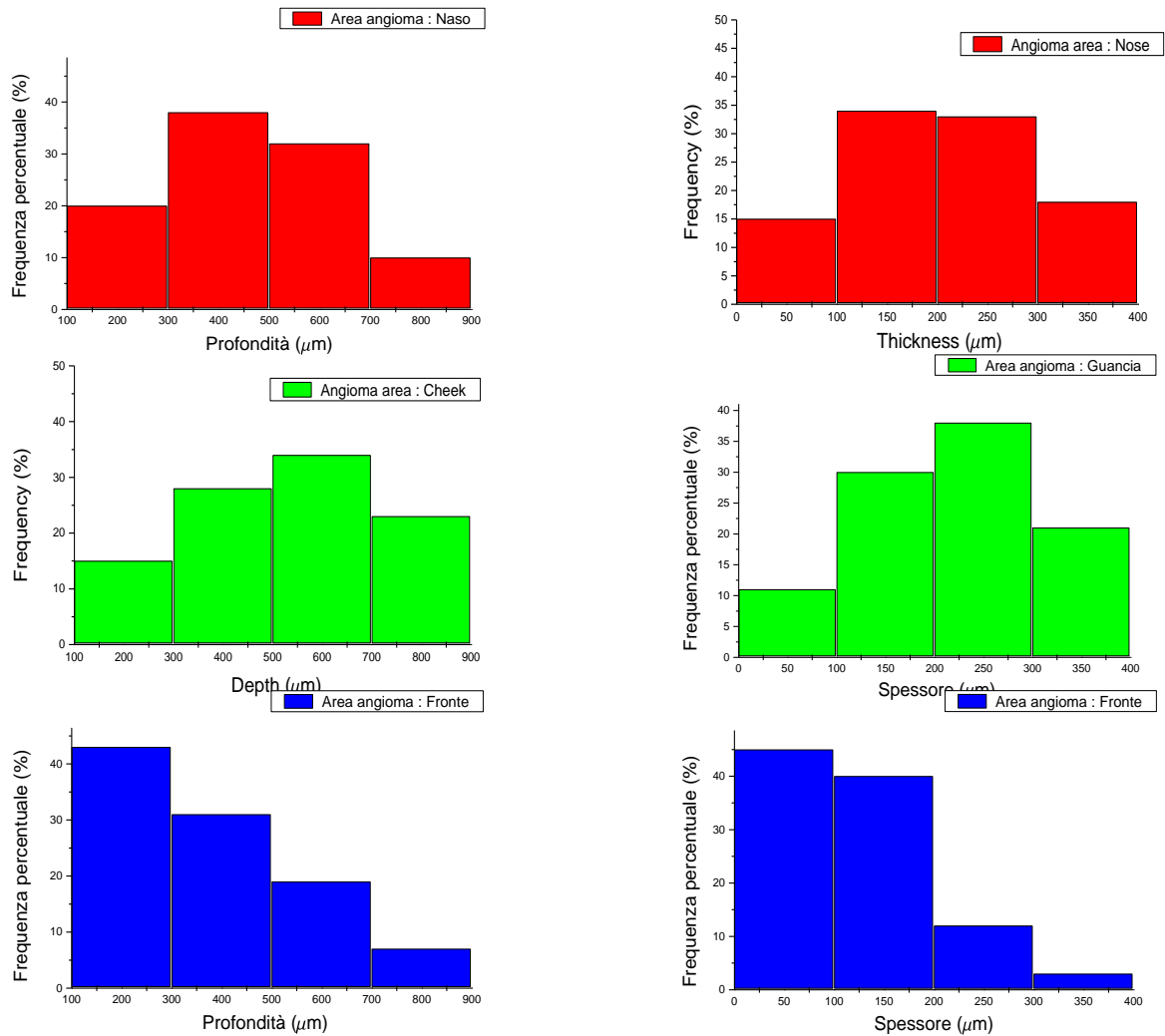


Fig. 4.10: Distributions relative to the depth and thickness evaluated on three anatomic facial region

As shown in the histograms, in average, the deeper and thicker plane angioma has been found in the cheek while the less depth and less thick on the temple. From these results, the formation of plane angioma seems to spread preferentially the anatomic region of the cheek. This is probably due to the higher presence in the cheek of subsurface fat respect to other facial region. A higher presence of fat, probably, facilitates the extention of the angioma differently from the other regions (for instance the temple) characterized by an higher presence of subsurface muscular tissue. These data permit, for each clinical situation, a specific morphological reconstruction of the multilayer biological tissue under treatment. Subsequently, on these multilayer it has been executed the 2D+1 numerical simulation based on the biometric heat transfer model described in chapter 3. In the simulations the thermal behaviour of the biological multilayers has been achieved for different set of laser parameters as input. The experimental results and the simulations referred to differents biological multilayer are reported and discussed in the next section.

4.5 Numerical simulations: results

The evaluations obtained in the previous section permit the reconstruction of the biological multilayer made of: epidermis, dermis, plane of vessels and dermis again, associated to different anatomic region of the face for each patient. Subsequently, on these multilayers it has been performed a numerical simulation based on a biometric heat transfer model described in the section 3.5. In the simulations the thermal behaviour of the biological multilayers has been achieved for different set of laser parameters as input. The numerical output consist in the evaluations of the spatials and temporal temperature profiles obtained on the multilayer after a single laser pulse. Next, some results achieved from the simulations will be shown and discussed. Moreover, different clinical situations will be compared among them. Starting from these results, at the end of the section, some set of laser parameters will be proposed for the treatment of multilayers with specific plane angioma sizes. The numerical program of calculation has been realized with a home-made Matlab code. In table 4.4 the thermal and optical costants used in the simulations and adviced from literature [110-114] are shown .

Optical and Thermal costants			
	Epidermis	Dermis	Blood vessels
Density	1 Kg dm ⁻³	1 Kg dm ⁻³	1,055 Kg dm ⁻³
Specific heat	3,7 *10 ⁻³ J Kg ⁻¹ K ⁻¹	3,7 *10 ⁻³ J Kg ⁻¹ K ⁻¹	3,6 *10 ⁻³ J Kg ⁻¹ K ⁻¹
Conductivity	0,209 *10 ⁻⁶ W m ⁻¹ K ⁻¹	0,322 *10 ⁻⁶ W m ⁻¹ K ⁻¹	0,492 *10 ⁻⁶ W m ⁻¹ K ⁻¹
Absorption coefficient	18-60 cm ⁻¹	2,2 cm ⁻¹	147 cm ⁻¹
Scattering coefficient (g)	470 cm ⁻¹ (0.790)	129 cm ⁻¹ (0.790)	468 cm ⁻¹ (0.995)
Refraction index (λ=595nm)	1,37	1,37	1,33

Tab. 4.4: *Optical and thermal costants used in the simulations*

The optical costants in table 4.4 refer to wavelenght of 595 nm and patients of phototype III. In the calculations the biological multilayer has been divided in a grid of 64x64 cells, the time step between two frames has been fixed to 1/20 s and the depth of the epidermal layer has been fixed to 100 μm.

- Numerical solution: thermal dynamics associated to the problem

In the next images, a typical case of temporal evolution achieved is shown. The sequences refer to the dynamics simulated on a structure with a plane angioma depth 600 μm and thick 100 μm obtained after a single laser pulse. The laser parameters used as input are reported in the tab. 4.5

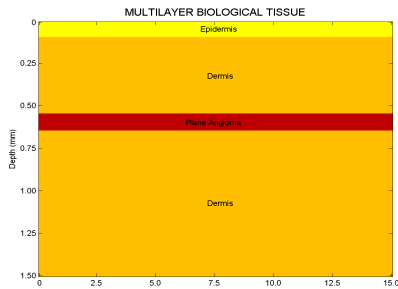


Fig 4.11: multilayer used in the simulation

laser parameters	
Energy density - Fluence	7 J/cm ²
Pulse duration	5 ms
Spot diameter	7 mm

Tab. 4.5: Laser parameters used in the simulation

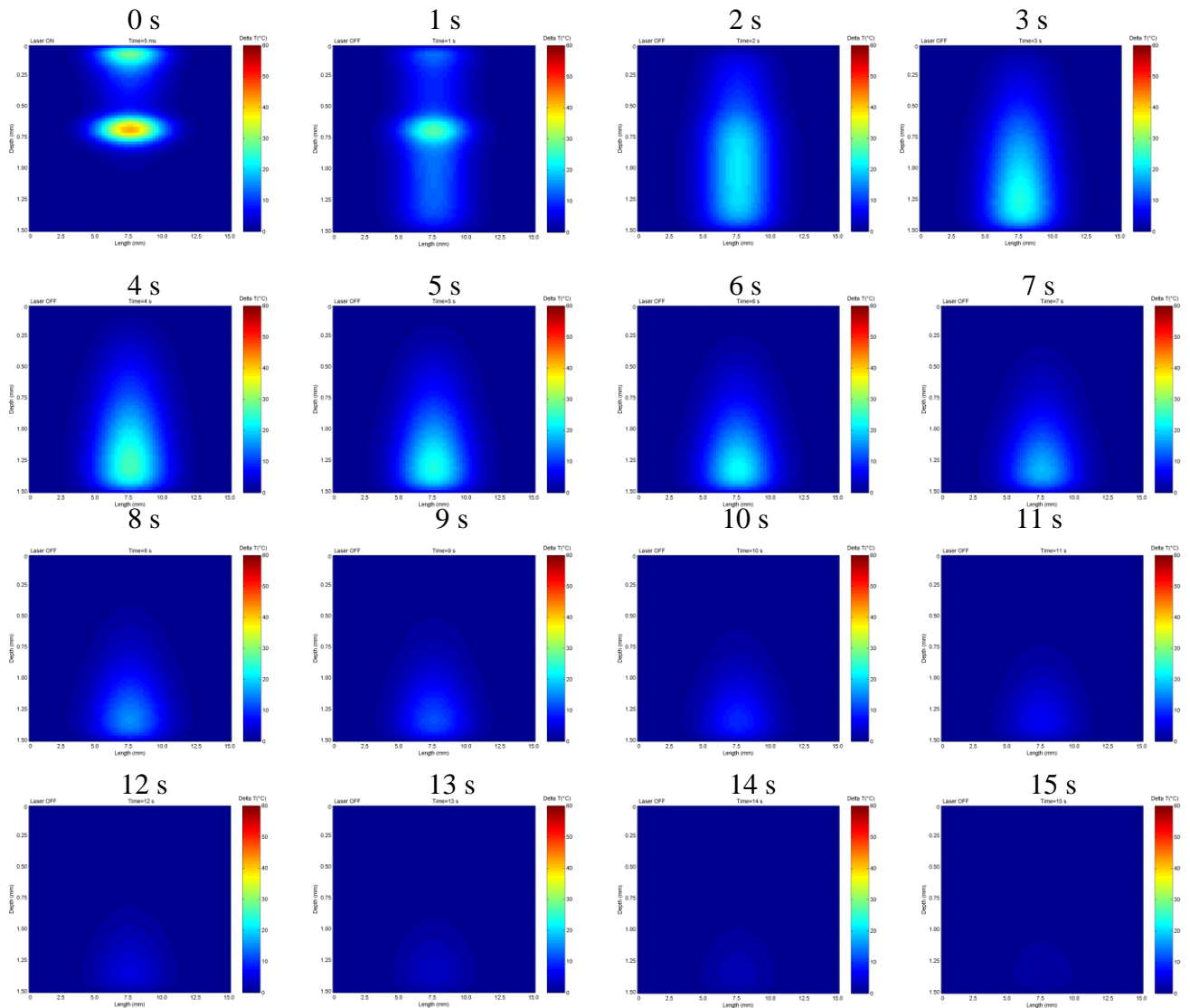


Fig 4.12: Temporal sequence of frames extrapolated from the simulations

The images reported have been extrapolated from a full sequence achieved from the simulation. The images corresponding to the instant $t=0$ s refers to the first grid calculated after the laser pulse. As it is possible to note from the sequence the thermal dynamics in the layers isn't neither homogeneous nor symmetrical as it was expected. For example, the layers more superficial recover quickly than deep layers and the heat, generated from the laser pulse, moves towards the core of the structure. This is mainly due to the different boundary condition present in the model (eq. 3.27) and associated to epidermis ($z=0$) and dermis ($z=D$, core) layers. Moreover, as widely discussed, the biological structure is a dishomogeneous multilayer with optical and thermal properties depending from the different tissues. In particular it is possible to note from fig. 4.12 (at $t=0$) how the temperature achieved on plane angioma layers is higher than the temperature found for epidermis or dermis because of the higher absorption coefficient at laser wavelength (595 nm) of the plane of blood vessels (table 4.4). This particular dynamics has been found in all numerical solutions calculated in different situations (for different multilayers and different laser parameters) and it is peculiar for this problem. Changing the biological multilayers and the laser parameters, this dynamics is obviously characterized from different temperatures for the layers and different recovery times.

- Numerical solutions referred to a same structure and for different laser parameters

In order to optimize the laser parameters for each specific treatment, the temperature obtained on the plane of vessels and on the other tissues of the structure must be evaluated for different set of laser parameters. In the next figures the results obtained from simulation on the biological multilayer in fig. 4.11 and with the laser parameters of the tab. 4.5 are reported. In particular, the distribution of the ΔT induced on the structure calculated at instant $t=0$ (immediately after the laser pulse), is showed in 2-D and 3-D representation. Moreover, the temporal evolutions and the spatial distribution of the temperature on the epidermis and on the plane of vessels are compared.

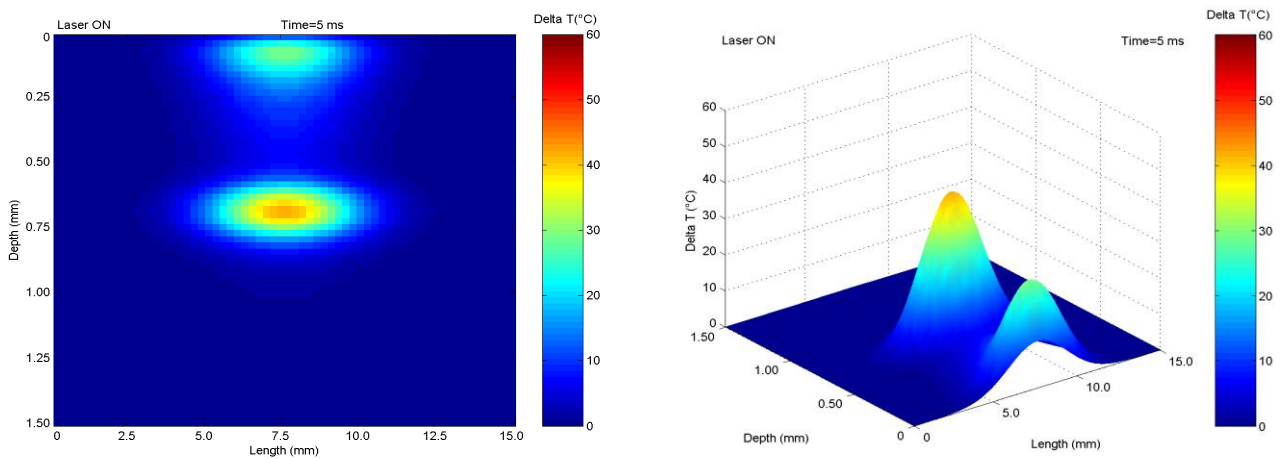


Fig 4.13: Distribution of the temperature calculated at instant $t=0$ s, 2D and 3D representation

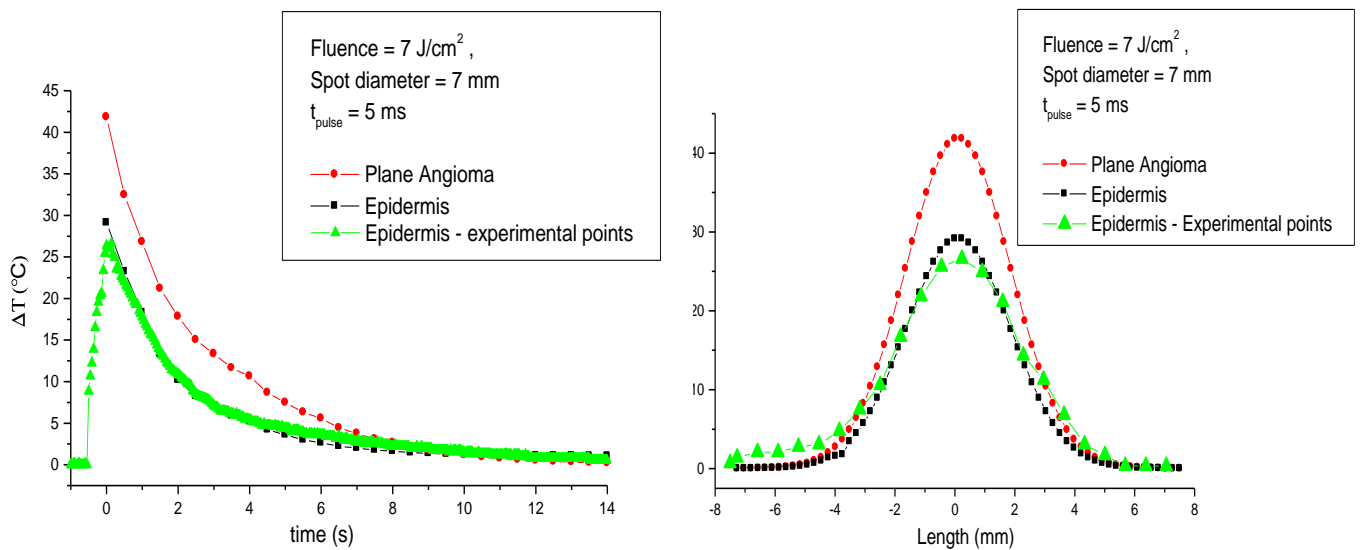


Fig 4.14: Temporal evolutions and spatial distribution of ΔT on the epidermis and on the plane of vessels

In the graphs in fig. 4.14 the temperatures for the plane angioma and the epidermis estimated from the simulation have been represented respectively with black and red point. In the same graphs, the experimental values recorded on the epidermis with the infrared camera are reported with green points. It is possible to observe as this last are in a good agreement with simulated data. The induced thermal gap calculated between the plane angioma and epidermis at instant $t=0$ s has been ~ 15 °C.

Starting from these laser parameters, the next graphs show how the numerical solutions change when the spot diameter moves from 7 mm to 2 mm or the pulse duration from 5 ms to 1 ms.

laser parameters	
Fluence	7 J/cm ²
Pulse duration	1 ms
Spot diameter	7 mm

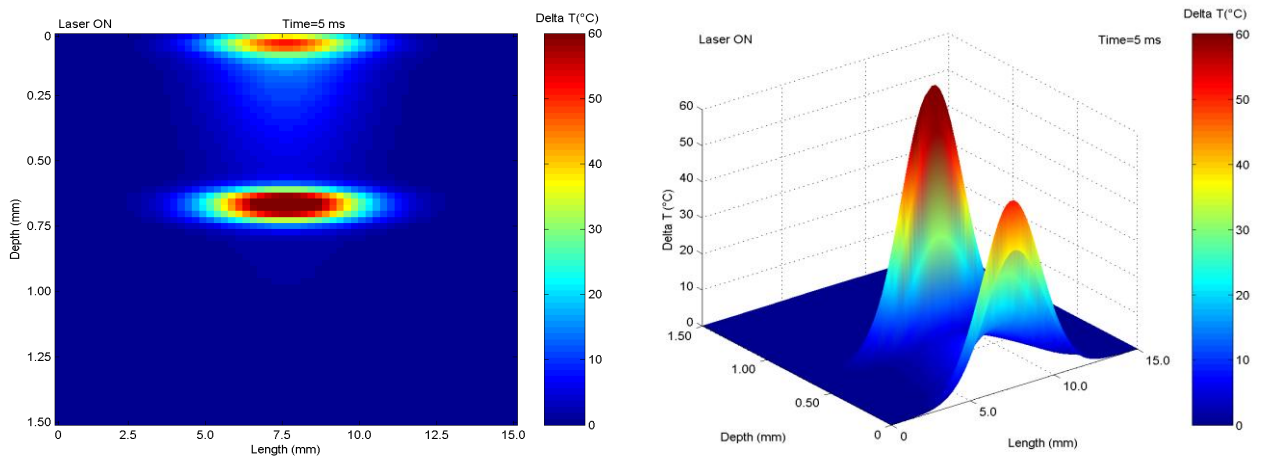


Fig 4.15: Distribution of the temperature calculated at instant $t=0$ s, 2D and 3D representations

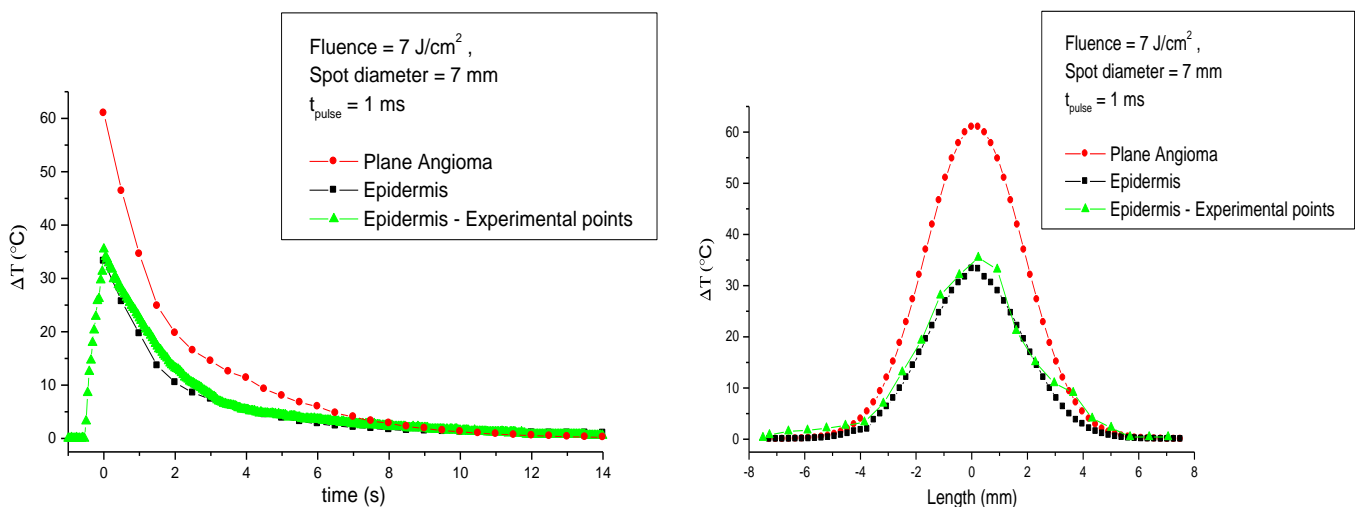


Fig 4.16: Temporal evolutions and spatial distribution of ΔT on the epidermis and on the plane of vessels

laser parameters	
Fluence	7 J/cm ²
Pulse duration	5 ms
Spot diameter	2 mm

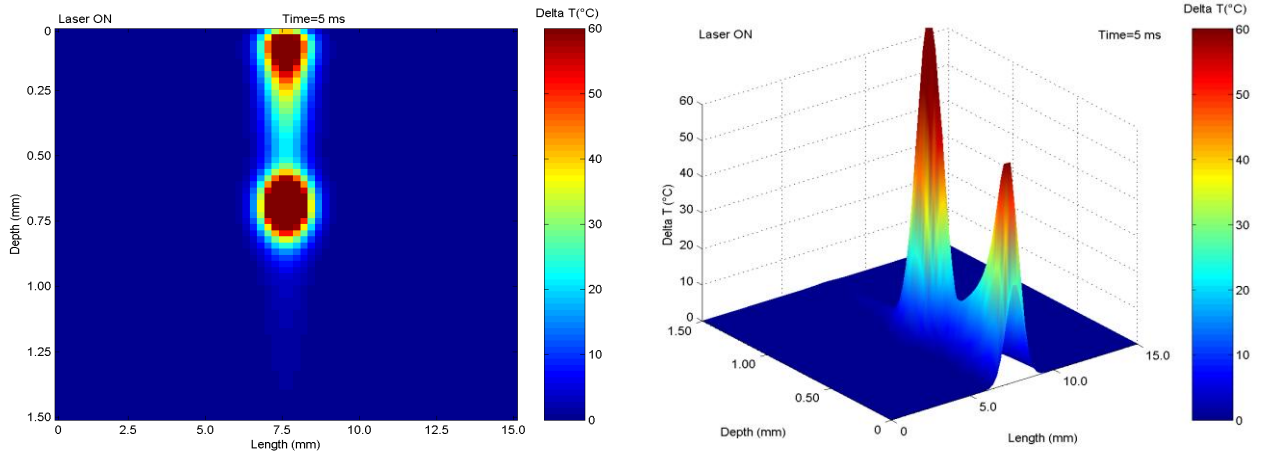


Fig 4.17: Distribution of the temperature calculated at instant $t=0$ s, 2D and 3D representations

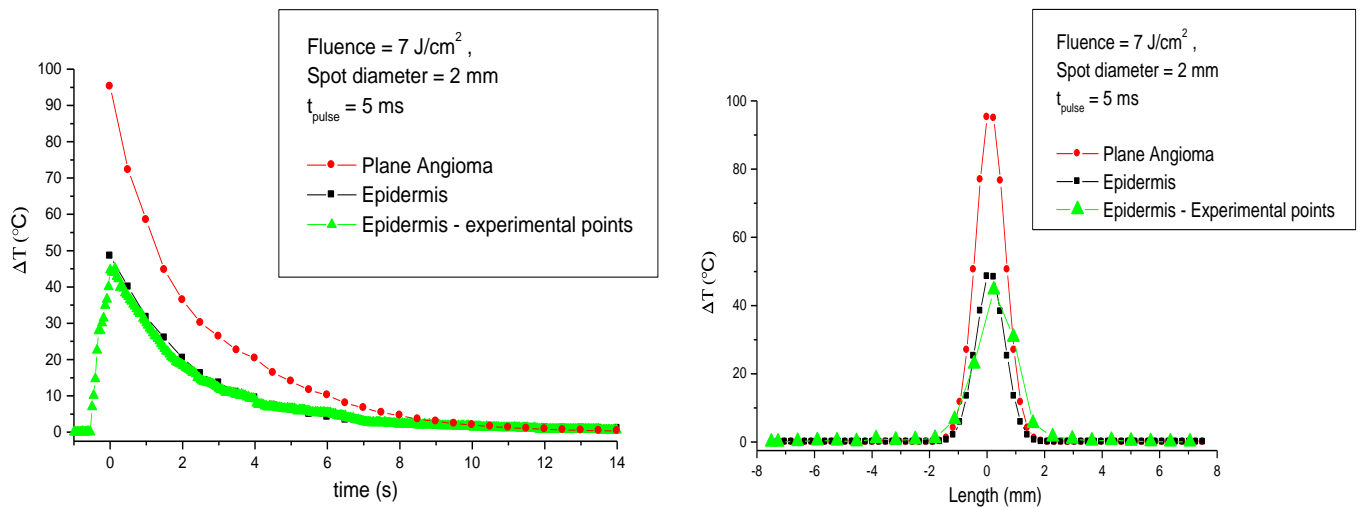


Fig 4.18: Temporal evolutions and spatial distribution of ΔT on the epidermis and on the plane of vessels

These last graphs show how, at instant $t=0$ s, both smaller spot diameter and shorter pulse duration induces a thermal gap between epidermis and plane angioma higher than the previous case. In fact, the difference on the maximum temperature achieved changes from ~ 15 °C to ~ 25 °C when the spot diameter changes from 7 mm to 2 mm and from ~ 15 °C to ~ 45 °C when the pulse duration changes from 5 ms to 1 ms. In these cases, a good agreement between numerical solutions and experimental data referred to epidermis layers has been obtained.

In the next numerical results the dynamics of the thermal gap induced by the laser pulse on the biological structure of fig. 4.11 are compared when two of the three laser parameters are fixed and just one is changed. A 2-D and a 3-D representation is given in all three different situations. In the first case, the pulse duration and spot diameter have been fixed while three different values for the fluence have been used.

laser parameters	
Pulse duration	5 ms
Spot diameter	2 mm

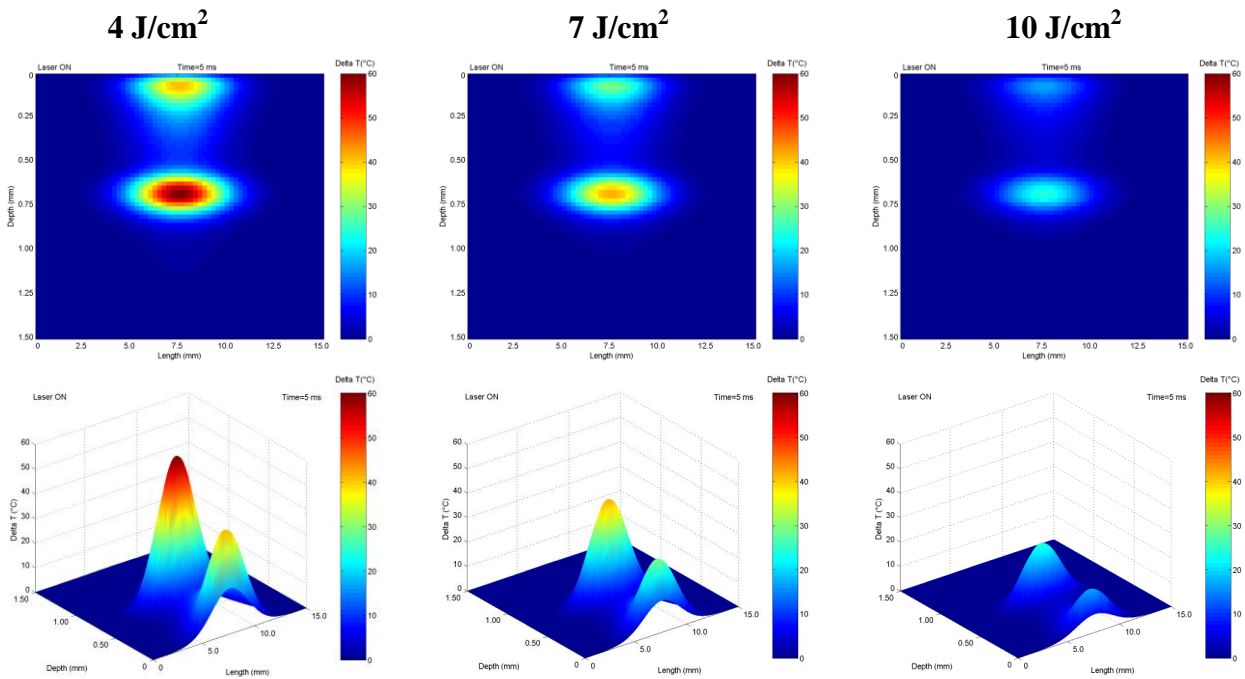


Fig 4.19: Distribution of the temperature calculated at instant $t=0$ s, 2D and 3D representations

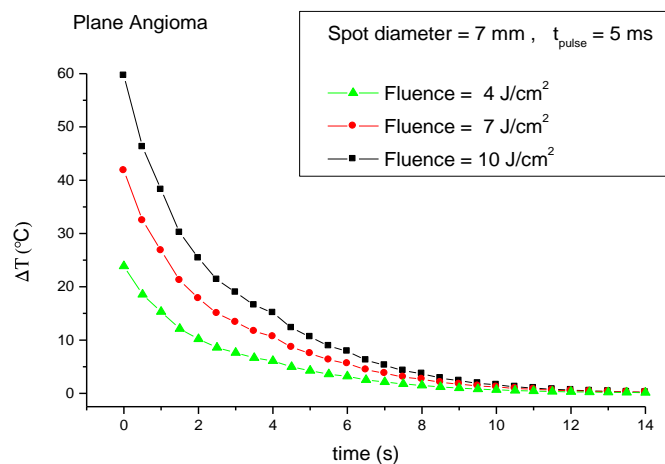


Fig 4.20: Temporal evolutions of ΔT on the plane of vessels for different fluence

The graph in fig. 4.20 shows clearly how the induced thermal gap can change from $\sim 25\text{ }^{\circ}\text{C}$ to $\sim 60\text{ }^{\circ}\text{C}$ for the range of fluence used in these simulations (4-10 J). In the second case, the fluence and spot diameter have been fixed while two different values of the pulse duration have been used.

laser parameters	
Fluence	4 J/cm ²
Spot diameter	2 mm

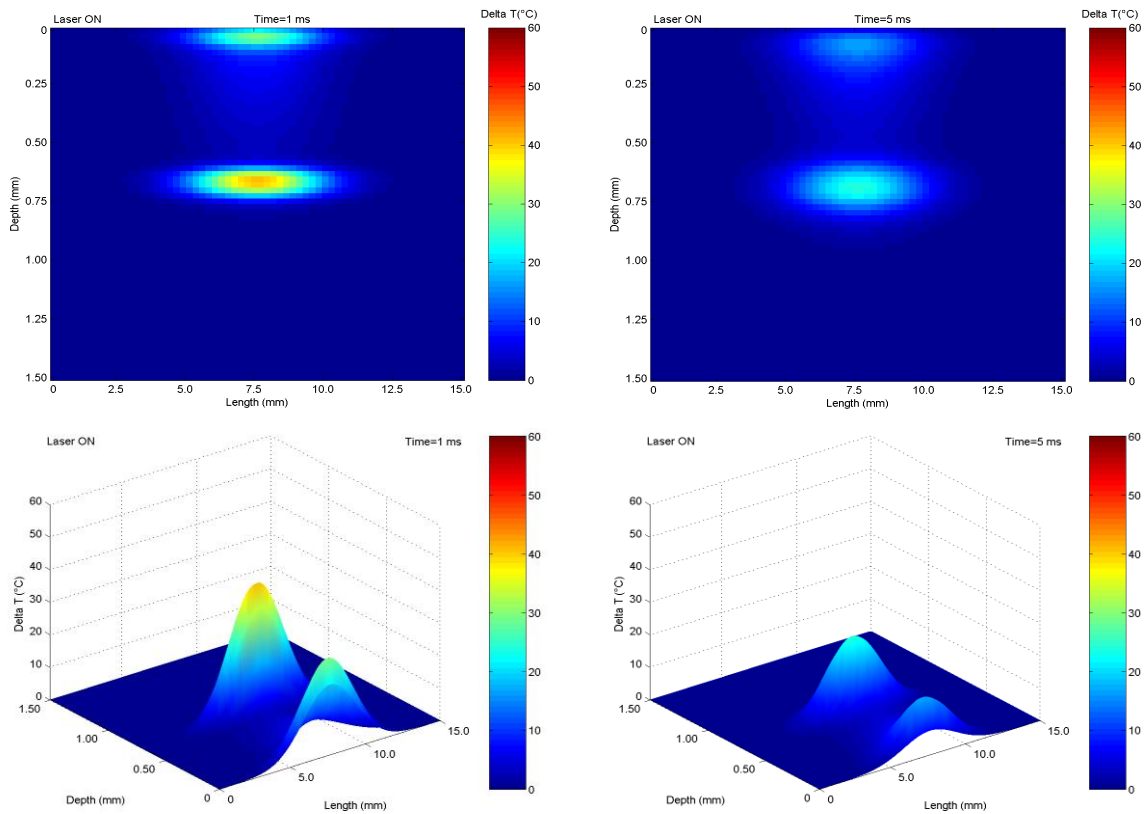


Fig 4.21: Distribution of the temperature calculated at instant $t=0\text{ s}$, 2D and 3D representations

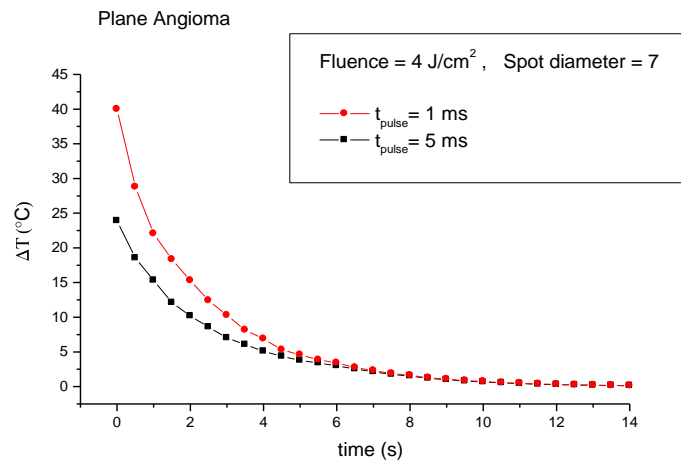


Fig 4.22: Temporal evolutions of ΔT on the plane of vessels for different pulse duration

In the last case, in the calculations, two values for the spot diameters have been used while the others two parameters have been fixed

laser parameters	
Fluence	7 J/cm ²
Pulse duration	5 ms

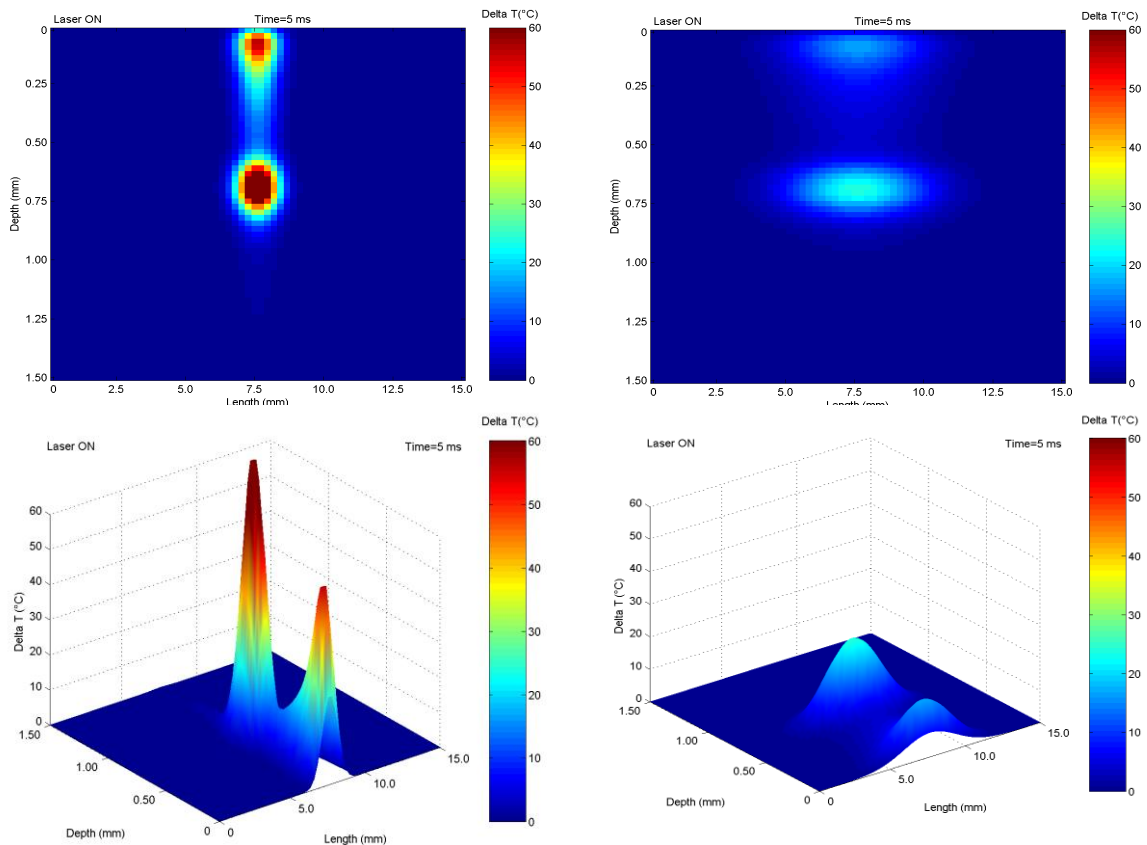


Fig 4.23: Distribution of the temperature calculated at instant $t=0$ s, 2D and 3D representations

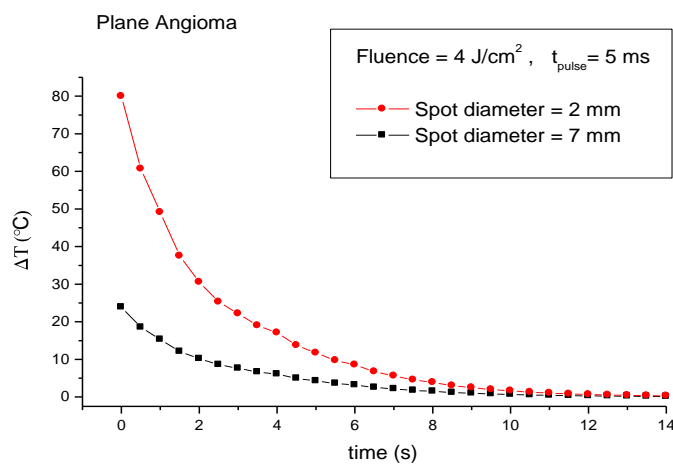


Fig 4.24: Temporal evolutions of ΔT on the plane of vessels for different pulse duration

As it is possible to observe from the last graph, the induced thermal gap from the laser pulse can vary massively when the spot diameter is changed.

- Numerical solutions referred to different structures with the same laser parameters

In this paragraph the results relative to the biological multilayer with a plane angioma at different depths or with different thicknesses are shown. All simulations and results shown in this section refer to the laser parameters reported in the table 4.5.

The first case is relative to three structures with a plane of vessels at different depth but with the same thickness. These structures associated to three different clinical situations have been numerically analysed. The depth of the angioma inside the three structures was respectively 300 μm , 600 μm and 900 μm while the thickness was 100 μm .

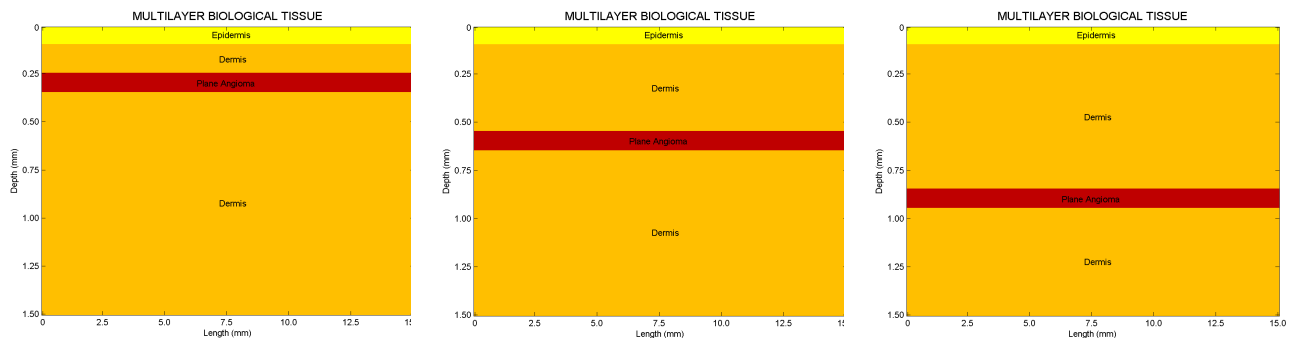


Fig 4.25: multilayer used in the simulations

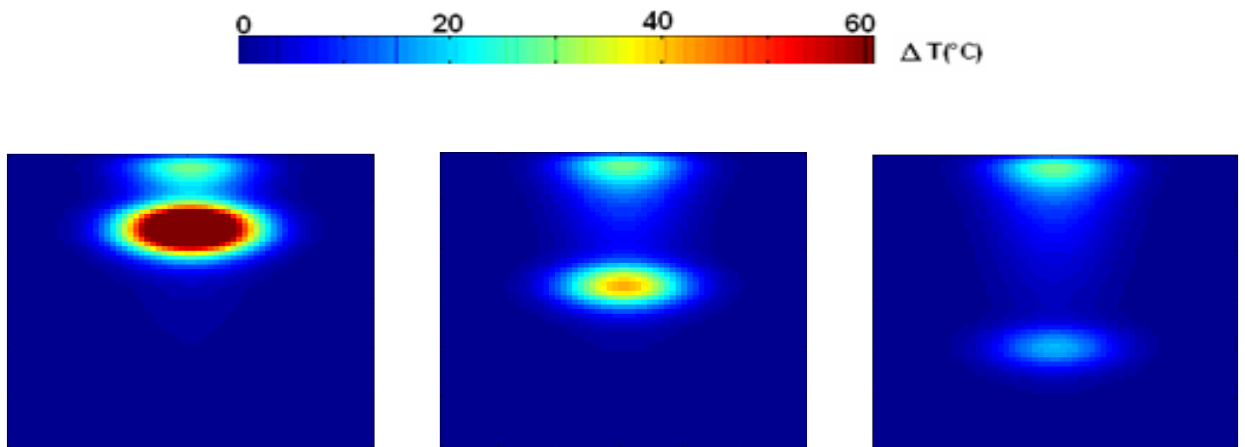


Fig 4.26: Distribution of the temperature calculated at instant $t=0$ s, 2D representation.

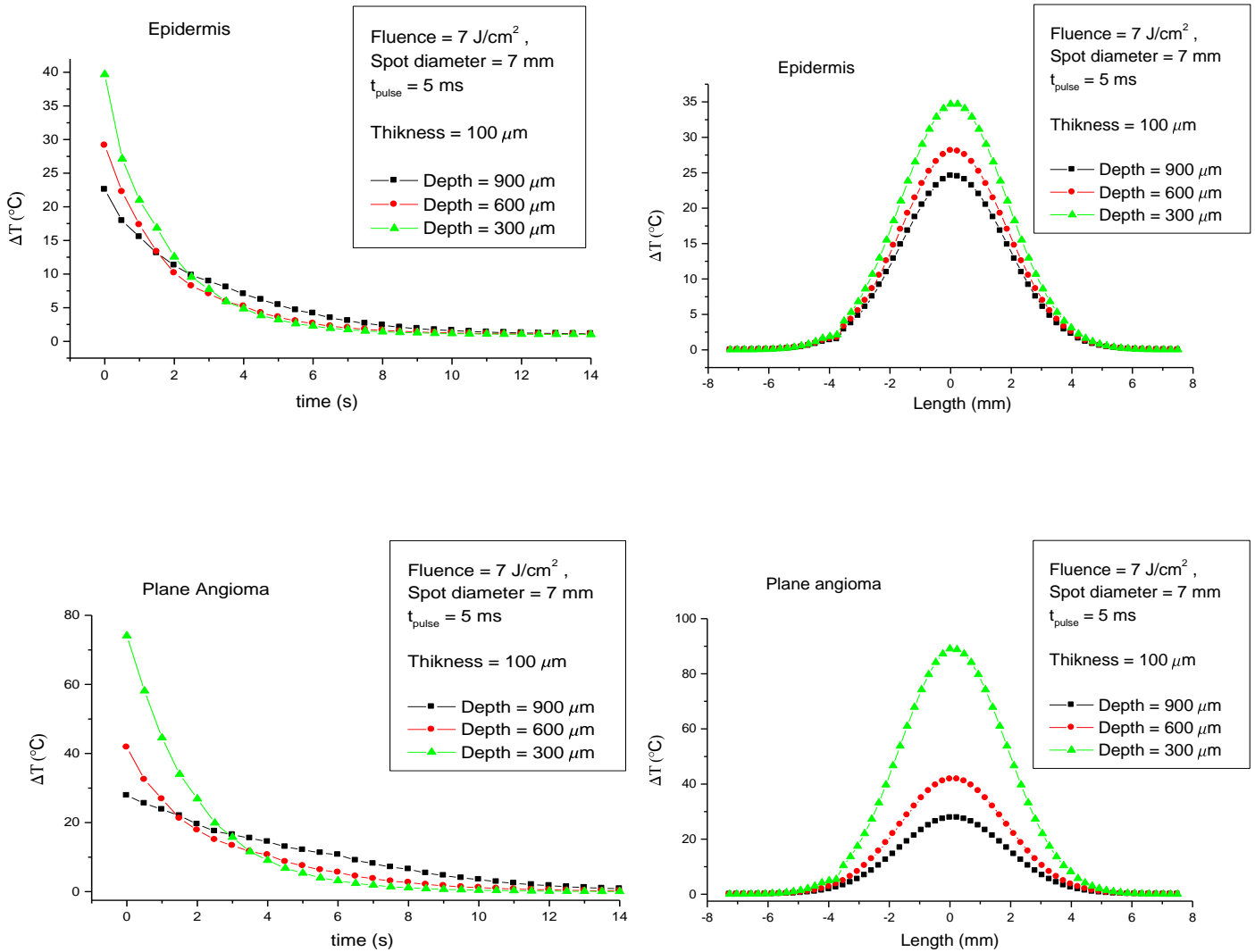


Fig 4.27: Temporal evolutions and spatial distribution of ΔT on the epidermis and on the plane of vessels

As in the previous case the false colours images extrapolated from the numerical solutions refer to the instant subsequent to the laser pulse ($t=0$ s). From the images in fig. 4 the temporal evolution and the spatial distribution of ΔT , in case of both epidermis and plane angioma layers, are graphicated. The simulations show how the difference found on the temperatures on structures affected by plane angioma to different depth in the tissue, are higher on the plane angioma layers than epidermis layers. For epidermis, ΔT change in the range from ~ 23 °C to ~ 40 °C, with a gap of ~ 17 °C, and for plane angioma layers from ~ 25 °C to ~ 75 °C, with a gap of ~ 50 °C. As it is expected, the temperatures obtained on the plane angioma are higher than the temperatures on the epidermis but the ratio $\Delta T_{\text{angioma}} / \Delta T_{\text{epidermis}}$ decreases for deeper plane of vessels. As it will be discussed later, this trend restricts just to patients affected by plane

angioma which are not too deep. In this case a laser therapy can supply good results and reduced risks.

In the next case analyzed, the numerical solutions relative to two biological structures with a plane angioma at same depth but with different thicknesses have been compared. For the two structures the thickness was 100 μm and 300 μm respectively, while the depth was 600 μm .

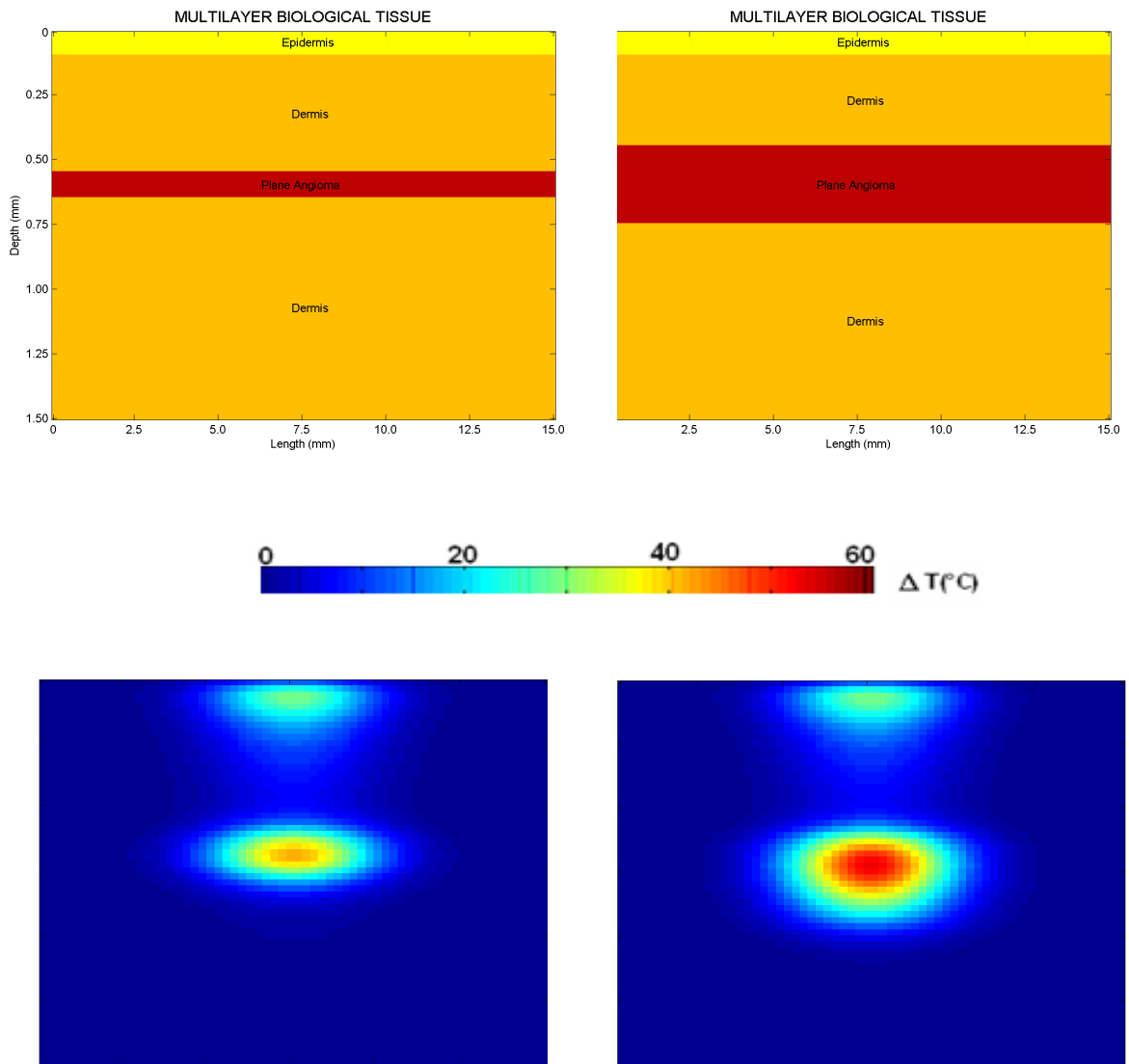


Fig 4.28: Distribution of the temperature calculated at instant $t=0$ s, 2D representation

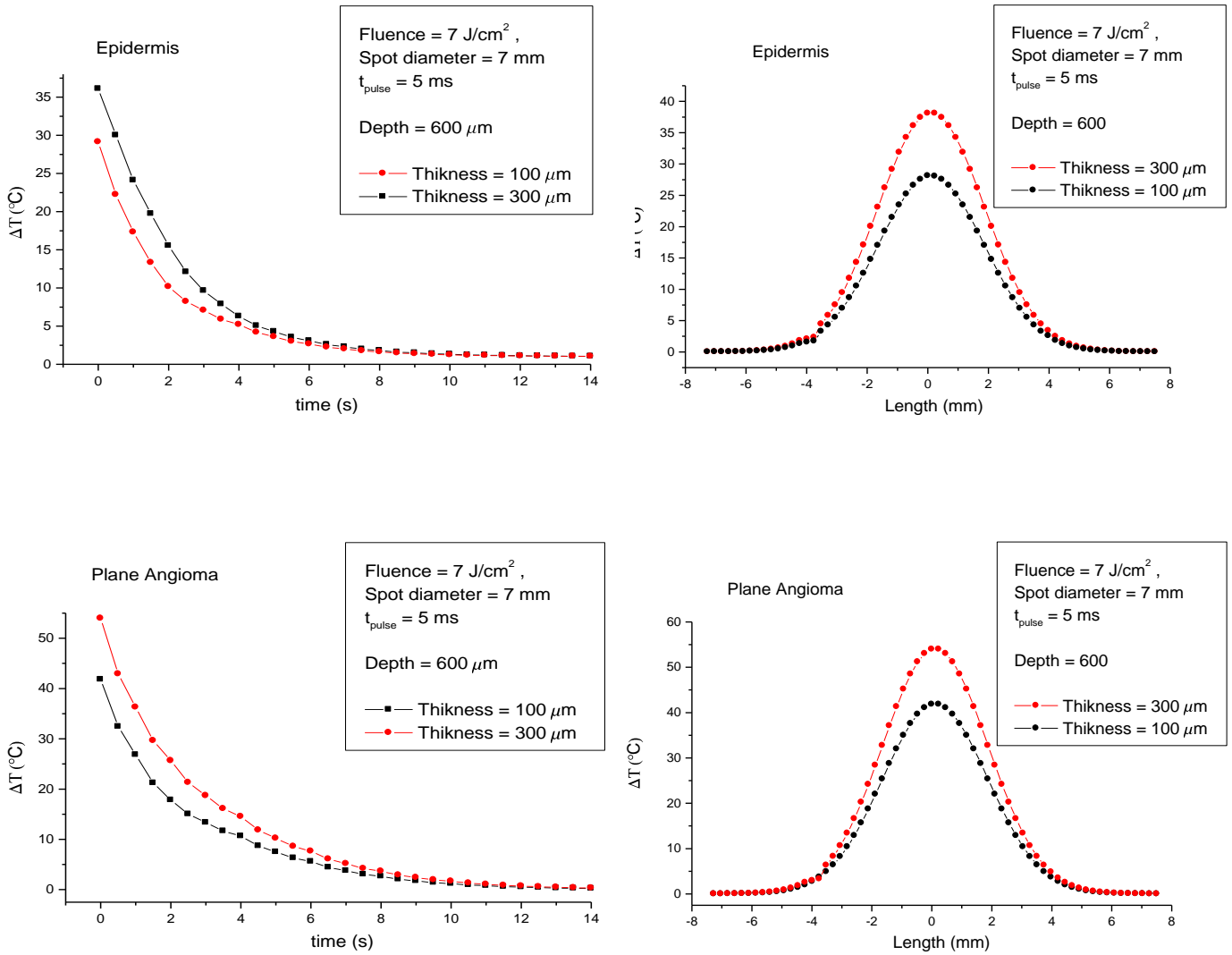


Fig 4.29: Temporal evolutions and spatial distribution of ΔT on the epidermis and on the plane of vessels

Differently from the previous case, from the graphs reported in fig. 4.29 the variations on the temperatures achieved in the two situations for the plane angioma and for epidermis are, substantially, the same. In fact, the maximum ΔT found for the plane angioma goes from ~ 42 °C to ~ 52 °C while the maximum ΔT found for the epidermis goes from ~ 28 °C to ~ 37 °C, with a gap in both situations of about ~ 9 - 10 °C. These results demonstrate how the thermal behaviour achieved in the multilayer biological structures affected by plane angioma is more sensitive to the variations of the depth than variations of the thickness.

In the next graphs the recovery time and the induced thermal gap (ΔT) versus the depth of the plane angioma in the tissue are reported. The data refer to evaluations achieved in the simulations. The values are relative to plane angioma with thickness 100 μm and 300 μm and various depths.

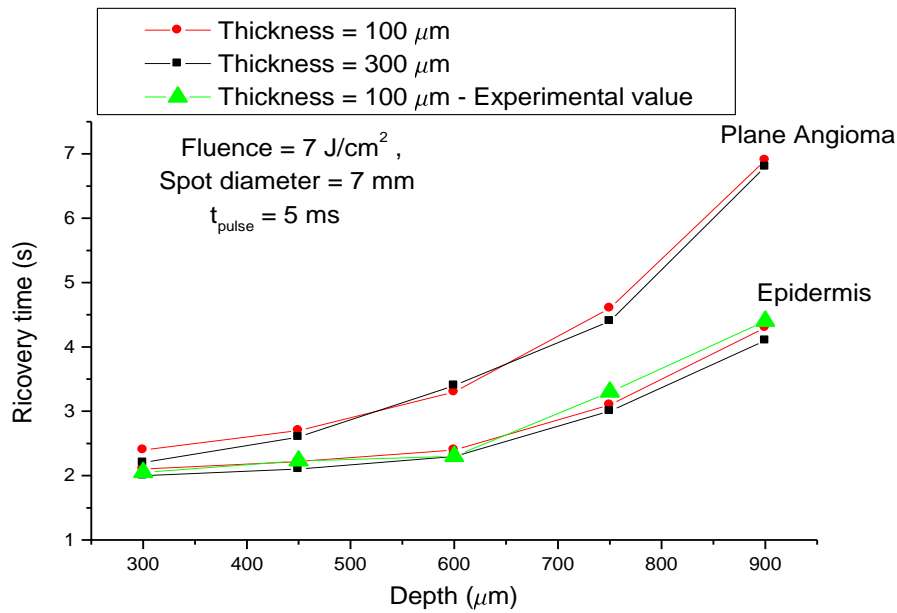


Fig 4.30: Recovery time versus depth for two different thickness

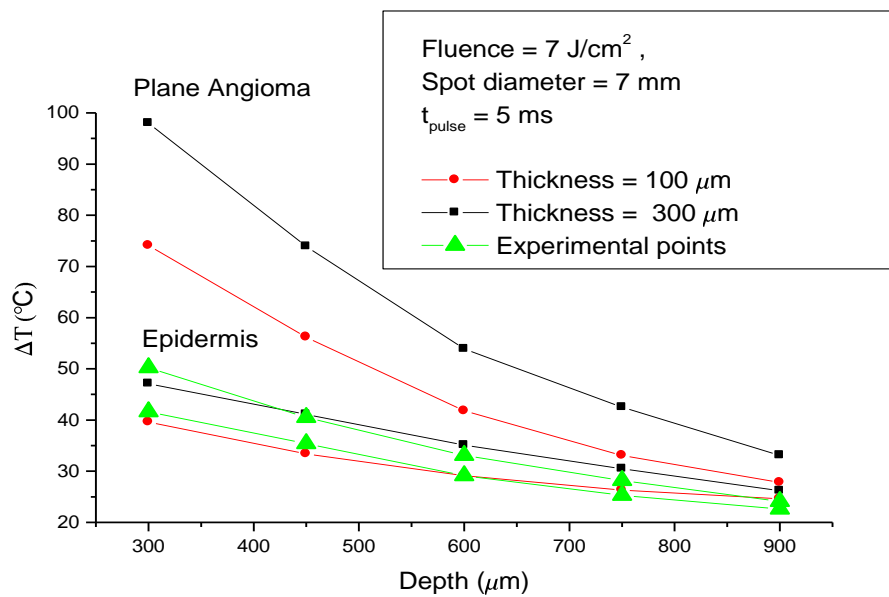


Fig 4.31: Induced thermal gap versus depth for two different thickness

From the graphs, it's clear, how the recovery time increases with the depth while it doesn't change at all to variations of the thickness. Differently from the previous case, the ΔT decreases with depth and increases with the thickness of the plane of vessels. In the graphs the experimental values referred to epidermis and extrapolated from some patients monitored are reported with green points. The graphs show clearly a good agreement between simulated data and experimental values in both situations.

- Numerical simulation for different phototypes

All numerical simulations and results up to now reported refer to patients of phototype III (typology more frequent). In this study, the thermal effects achieved on different phototypes have been compared. From an optical point of view, patients of different phototype are characterized from a different absorption coefficient for the epidermal layers. In fig. 4.33, numerical simulations on three equal multilayers (with same dimensions for the plane of vessels) but with different phototypes are shown. The results refer to structures with a plane angioma depth 600 μm and thick 100 μm (fig. 4.11) and laser parameters reported in table 4.5. The absorption coefficients for the epidermis used in the simulations are reported in table 4.6

Absorption coefficient	
Phototype I	7 J/cm ²
Phototype III	5 ms
Phototype IV	7 mm

Tab. 4.6: Absorption coefficients for the epidermis used in the simulations

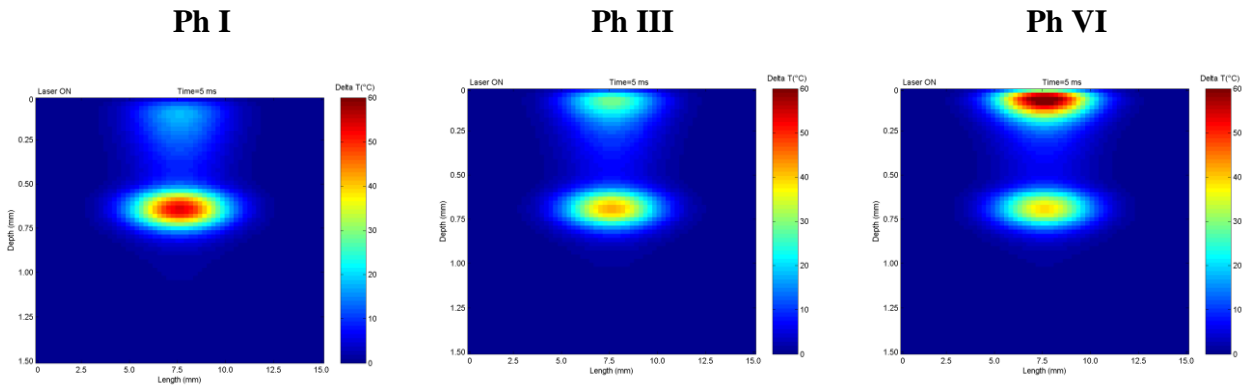


Fig 4.32: Distribution of the temperature calculated at instant $t=0$ s for different phototype

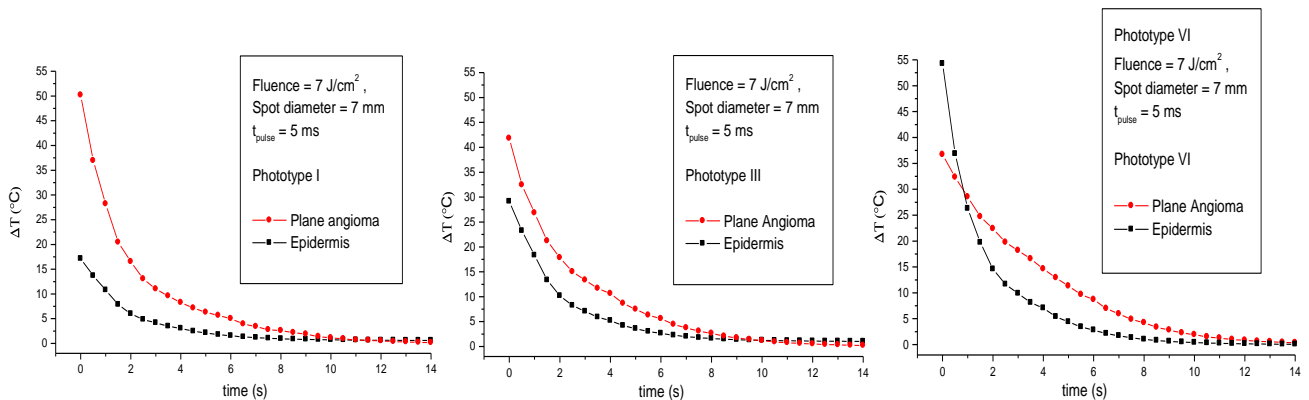


Fig 4.33: Temporal evolutions of ΔT on the epidermis and on the plane of vessels for different phototypes

In figure 4.33 the temporal rate of the ΔT calculated on epidermis and on plane angioma has been compared for each different phototype. From the graphs, the thermal gap between epidermal layer and plane angioma layer increases going from phototype VI to phototype I and in particular, for phototype VI the laser pulse induces a maximum ΔT on the epidermis (for $t = 0$ s) higher than the maximum ΔT obtained on the angioma. In next figure the temporal rate of ΔT referred to the epidermis and plane angioma are reported separately for the three phototypes

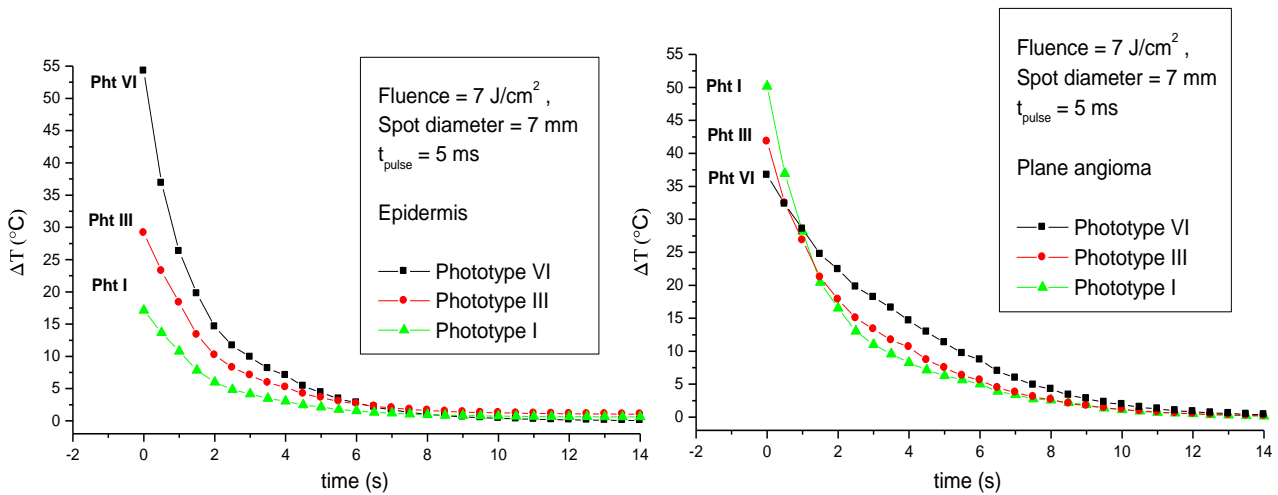


Fig 4.34: Temporal evolutions of ΔT on the epidermis and on the plane of vessels for different phototypes

The graphs show, clearly, as going from phototype I to phototype VI that the temperature obtained on the epidermis increases while the temperatures found on the angioma decreases. For the epidermis, the maximum gap of the temperature has been estimated to be about ~ 37 °C (from ~ 18 °C for phototype I to ~ 55 °C for phototype VI) while for the angioma it has been found of ~ 13 °C (from ~ 37 °C for phototype VI to ~ 50 °C for phototype I).

4.6 Limit conditions for applications of laser treatments

As discussed in chapter 1, in the laser therapy performed in the photothermal regime, the temperatures induced on the tissues are strictly linked to the histological modification obtained. In general, the goal of the laser therapy is to obtain a local and selective interaction with the target structures (selective photothermolysis principle). Particularly, for treatment on plane angioma, a complete photocoagulation of the blood vessels and, in the same time, a lower interaction with the surrounding tissues (dermal and epidermal layers) is desired. It means, practically, to maximize the temperature on the plane angioma and minimize the temperatures on the epidermis and dermis induced by a laser pulse.

The last results in fig. 4.33 and 4.34 emphasize how in some circumstance this is impossible. In fact, if the ratio $S_I = \Delta T_{\text{epidermis}} / \Delta T_{\text{angioma}}$ can be regarded as a selectivity index of the interaction, then for the tissues of phototype V-VI (where $S_I \geq 1$) the application of laser therapy can be hazardous.

In this patient the lower temperatures achieved on the angioma makes the blood vessels photocoagulation improbable and at the same time the higher temperatures achieved on the epidermis and dermis can produce the formation of scars due to the collagen denaturation. It is possible to note, as the same situation ($S_I \geq 1$) is found for angiomas deeper than about $\sim 900 \mu\text{m}$ (as it has seen above) independently from the phototypes, and, so, in these case too, the results achieved by simulations advises against the application of the laser treatments.

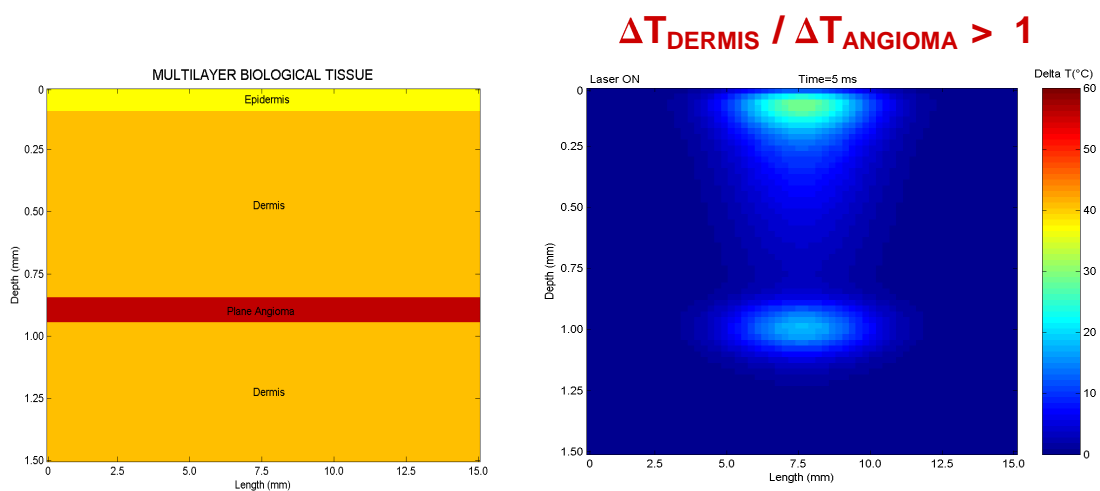


Fig 4.35: Distribution of the temperature calculated at instant $t=0$ s for a phototype III with a plane angioma depth $900 \mu\text{m}$ and thick $100 \mu\text{m}$.

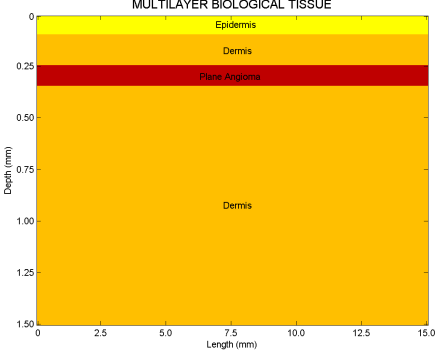
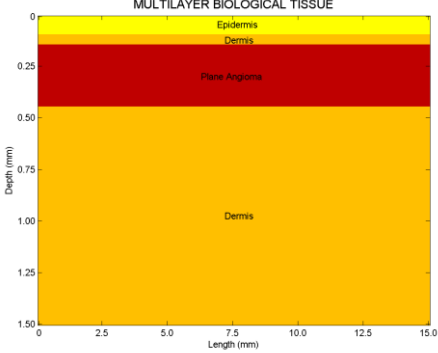
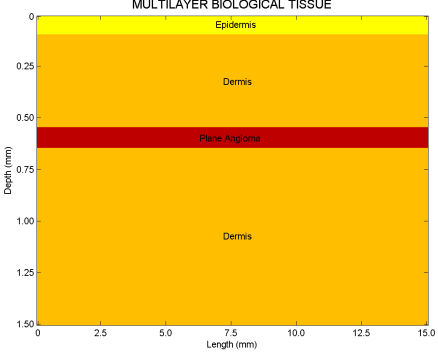
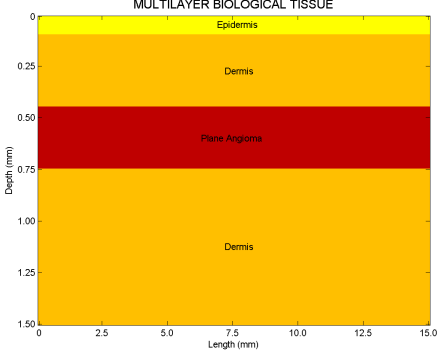
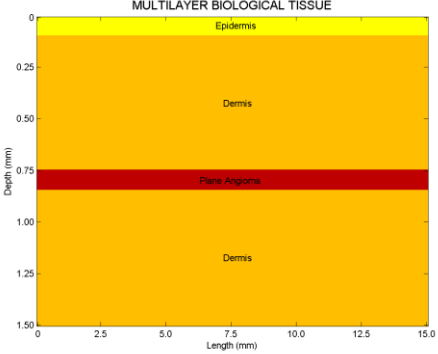
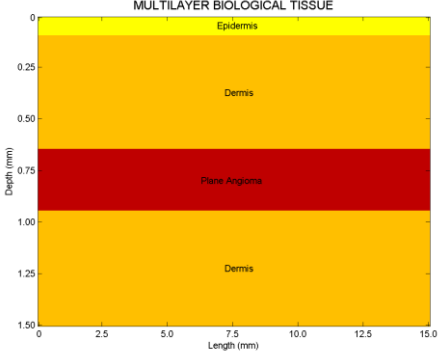
4.7 Final conclusions: set of laser parameters

The results shown up to now together with the complete study on the patients, give a wide vision about the the thermal behaviour of the biological multilayer affected by plane angioma when they are subject to selective laser interactions. These results represent a first step in order to optimize laser parameters for specific clinical situations. In fact, as an output of this work it comes that it is possible to choose a set of laser parameters in order to accomplish these relations for each different biological multilayer

$$\begin{array}{ll} \Delta T_{\text{EPIDERMIS}}, \Delta T_{\text{DERMIS}} < 30^{\circ}\text{C} & \leftarrow \text{Safety} \\ 45^{\circ}\text{C} < \Delta T_{\text{ANGIOMA}} < 75^{\circ}\text{C} & \leftarrow \text{Photocoagulation range} \end{array}$$

The above ranges, are chosen in order to photocoagulate the blood vessels of the angioma and at the same time to reduce the risks of scars formations. According to these indications, different set of laser parameters can be proposed. Just as an example, in tab. 4.7 some set of laser parameters are proposed for treatment of patients affected by plane angioma of different dimensions. The set shown refers to patients of phototype III.

These parameters are given with the aim to achieve a more specific and appropriate interaction with the tissue of the patient and to make laser treatments more safety and more efficient. With this approach, others set can be suggested for different phototype and for different sizes of the plane angioma.

<div style="text-align: center;">Thickness</div> <div style="text-align: center;">Depth</div>	<div style="text-align: center;">100 μm</div>	<div style="text-align: center;">300 μm</div>
<div style="text-align: center;">300 μm</div>	<div style="text-align: center;">  </div> <div style="text-align: center;"> <p>Fluence = 3 J/cm²</p> <p>Spot diameter = 7 mm</p> <p>Pulse duration = 5 ms</p> </div>	<div style="text-align: center;">  </div> <div style="text-align: center;"> <p>Fluence = 3 J/cm²</p> <p>Spot diameter = 7 mm</p> <p>Pulse duration = 7 ms</p> </div>
<div style="text-align: center;">600 μm</div>	<div style="text-align: center;">  </div> <div style="text-align: center;"> <p>Fluence = 9 J/cm²</p> <p>Spot diameter = 7 mm</p> <p>Pulse duration = 5 ms</p> </div>	<div style="text-align: center;">  </div> <div style="text-align: center;"> <p>Fluence = 5 J/cm²</p> <p>Spot diameter = 7 mm</p> <p>Pulse duration = 5 ms</p> </div>
<div style="text-align: center;">800 μm</div>	<div style="text-align: center;">  </div> <div style="text-align: center;"> <p>Fluence = 16 J/cm²</p> <p>Spot diameter = 7 mm</p> <p>Pulse duration = 5 ms</p> </div>	<div style="text-align: center;">  </div> <div style="text-align: center;"> <p>Fluence = 11 J/cm²</p> <p>Spot diameter = 7 mm</p> <p>Pulse duration = 5 ms</p> </div>

Tab 4.7: Some set of laser parameters proposed for a phototype III and for different dimensions of the plane angioma

In conclusion, with the approach described a good agreement between numerical solutions and experimental results has been obtained for both recovery time and temporal evolution of ΔT in the majority of cases, particularly, for more superficial angioma. In case of deeper angioma ($d > 900 \mu\text{m}$), a mismatch between numerical solution and experimental values have been often found due to a higher error achieved in the evaluation of the dimensional parameters of the angioma with the PT model used.

However, the results up to now obtained in this study are encouraging and a further goal is to extend the analysis from a relatively small number of patients monitored to a larger population. Therefore, in the next steps of this research activity, new PT models will be tested in order to achieve a more accurate evaluation of the dimensional parameters of the plane angioma and, subsequently, the set proposed will be gradually tested on different targets with the aim to obtain, eventually, a complete validation of this novel approach.

General Conclusions

In this thesis the laser – biological tissue interaction has been studied and analyzed with the support of the infrared imaging technique.

This work started with an overview on the fundamental theoretical concepts of the laser–tissue interaction. In particular, the main laser-tissue interaction mechanisms as the photothermal interaction, the photochemical interaction, the photoablation, the plasma-induced ablation and the photodisruption have been described. Greatest attention has been given to the description of the photothermal regime of interaction, to the thermodynamic effect, and to the selective photothermolysis principle which are core of the present work.

The state of art of the laser application in the medical field has been made in order to have an overview of the different use of lasers in medicine, of the laser systems applied, of the methodological approach commonly used and protocols. At the same time the results and limits of the therapy have been estimated.

Subsequently, the principles and applications of the infrared imaging technique have been reported. Both passive and active approach have been explained, mainly focusing principally the attention on the different active procedures.

Several active thermographic techniques commonly used, that differ one another mainly in the way data is acquired and/or processed, have been reviewed and discussed: pulsed approach, step heating or long pulse method, lock-in thermography and vibrothermography. In this description more emphasis has been given to the presentation of the pulsed thermography method because it is a part of the experimental procedure used in this activity. Different definitions of thermal contrasts used for inversion algorithms have been given and compared: contrast for the transmission mode, contrast for the reflection mode and the differential absolute contrast (DAC). The problems relative to the atmospheric transmittance and infrared sensors have been treated. An overview on the infrared detector as bolometers, pyroelectric detectors, quantum detectors, Focal Plane Arrays (FPA) devices and on their main performance parameters has been made. Moreover, the novel approach and the new applications of infrared imaging in medical science has been discussed.

In the third chapter, the core of the research activity has been described. The novel approach proposed for the laser parameters optimization in the plane angioma treatment has been illustrated and explained in details. The pathology analyzed (plane angioma) and computation tools used have been treated and discussed. Particularly, the pulsed thermography model and the numerical approach adopted in the operative protocol performed have been explained rigorously.

The experimental activity was constituted of the following steps:

- 1) Assembly of the monitoring station including a thermal camera, a data acquisition system and a laptop to elaborate the IR images collected.
- 2) Introduction of the monitoring station in the operative unit of photodynamic and phototherapy ambulatory of the University of Naples "II Policlinico". The research activity started, firstly, with a series of preliminaries clinical tests on patients affected by Plane Angioma.
- 3) From the results of the preliminaries test a standard procedure for data acquisition has been conceived (as described in section 4.2). All patients have been monitored along a cycle of therapies of about 18 months. During this time different data referring to the thermal behaviour of the tissue under treatment have been recorded.
- 4) The data recorded have been processed with the pulsed thermography model and then with the numerical simulation based on a biometric heat transfer model according to the operative approach described in the chapter 3.

The main experimental and numerical results found with this approach have been reported and discussed in detail. First of all, the results relative to preliminaries test and observations have been illustrated. In particular, it has been shown how comparing the thermal response obtained in a specific anatomical region after a single laser pulse on different patients (with the same laser parameters), the final temperature, achieved immediately after the pulse, can be very different, with a $\Delta T \cong 25 \text{ }^\circ\text{C}$ too. A Similar situation has been found for the thermal response obtained in different facial region of a same patient affected by plane angioma. In general,

from the evaluations performed on all patients it has been found how with the same laser parameters, on a same patient and in presence of the same pathology, the ΔT among different anatomical regions can be higher than 15-20 °C. However, for a same patient in a same facial region it has been obtained a good repetitions of the temperatures measured. The temporal evolution of the temperatures after the laser pulse has been also recorded and analyzed for different anatomical regions. In general, this dynamic depends on the anatomical region under investigation and different average recovery times have been evaluated for each facial region. However, as well as for the temperatures, when the analysis is focused on a same patient in a same anatomical region a good repeatability of the dynamic has been achieved.

All evaluations obtained in the preliminary tests, emphasise how the thermal behaviours of the tissues achieved under laser treatment for a given set of laser parameters, depend on the specific target. Particularly, they can differ from region to region and from patient to patient. As reported, in the photothermal interaction regime, the temperature induced in the tissue is strictly linked to the hystological modification obtained. Therefore, these results point out that with the same laser parameters, changing patient or anatomical region, the effects and so the therapeutic efficiency obtained can differ a lot, changing from optimal therapeutic results to unwanted harmful effects (for instance scars formation). These observations justify and confirm if we don't use specifics and tailored laser parameters for each different clinical situation the laser treatments on plane angioma pathology permits an optimal improvement just in a small part of patients.

Subsequently, the results obtained using the novel approach proposed have been illustrated. For each patient the depth and thickness associated to plane angioma in the specific region under treatment evaluated with the PT model has been showed. The depth estimated mainly changes in the range from 300 μm to 700 μm while the thickness changes from 100 μm to 300 μm . Moreover the deeper and thicker plane angioma has been found in the cheek region as an average, while the less depth and less thick has been found on the temple region. These evaluations allowed a specific morphological reconstruction of the multilayer biological tissue under treatment for each clinical situation. On these multilayer the 2D+1 numerical simulation has been executed. The numerical program of calculation has been realized with a "*home-made*" Matlab code.

In the simulations the thermal behaviour of the biological multilayers has been achieved for different set of laser parameters as input. A typical case of temporal sequence made of grid representing the temperature distribution and calculated with the numerical model has been shown and discussed.

Next, numerical solutions referred to a same structure and for different laser parameters have been illustrated. The temporal evolutions and the spatial distribution of the temperature on the biological layers have been compared. The induced thermal gap (ΔT) calculated between the plane angioma and epidermis at instant $t=0$ s referring to the reference laser parameters has been found ~ 15 °C. Changing the spot diameter or the pulse duration the induced ΔT can increase up to ~ 25 °C and up to ~ 45 °C respectively.

At a second stage, numerical solutions referring to different structures with the same laser parameters have been compared. In a first case, the results referring to three structures with a plane of blood vessels at different depth (900 μm , 600 μm and 300 μm) but with the same thickness (100 μm) have been reported. In this situations, ΔT moves from ~ 23 °C to ~ 40 °C (with a gap of ~ 17 °C) for epidermis, and moves from ~ 25 °C to ~ 75 °C (with a gap of ~ 50 °C) for plane angioma layers, when deeper angioma are taken. In a second case, two biological structures with a plane angioma at same depth (600 μm) but with different thickness (100 μm and 300 μm) have been compared. Differently from the first case, the variations on the temperatures achieved for the plane angioma and for epidermis has been, substantially, the same. In fact, the maximum ΔT found for the plane angioma goes from ~ 42 °C to ~ 52 °C while the maximum ΔT found for the epidermis goes from ~ 28 °C to ~ 37 °C, with a gap in both situations of about ~ 9 - 10 °C.

These results demonstrate how the thermal behaviour achieved under treatment, on the multilayer biological structures affected by plane angioma, is more sensitive to the variations of the depth than variations of the thickness.

Subsequently, the thermal effects achieved on different phototypes have been compared. This last evaluation emphasizes how the thermal gap between epidermal layer and plane angioma layer decreases going from phototype I to phototype VI. In particular, for phototype VI the laser pulse induces a maximum ΔT on the epidermis (for $t=0$ s) higher than the maximum ΔT obtained on the angioma.

In all situations the experimental values and the numerical results have been compared and, in the majority of cases, a good agreement has been obtained for both recovery time and temporal evolution of ΔT , above all, for more superficial angioma.

After these results, the limit conditions for application of laser treatments have been discussed, focusing on particular situation (higher phototype or deeper angioma) where the results achieved advise against the application of the laser treatments.

From the evaluation realized, it is possible to choose a set of laser parameters for each different biological multilayer in order to optimize the thermal interaction and so to make laser treatments safer and more efficient. Some set of laser parameters have been proposed and illustrated for treatment of patients affected by plane angioma of different dimensions.

In conclusion in this thesis it has been demonstrated that functional IR imaging can be used with remarkable advantages in monitoring the physical action of the laser lighth thus giving to the operator (the physician) information to optimize his activity, in terms of both therapy effect and safety.

Our further aim is to obtain a complete validation of this novel approach on this research activity will be done according to the next steps:

- Testing new PT model in order to achieve a more accurate estimation of the dimensional parameters for the plane angioma.
- Gradual application of the proposed laser parameters set on different targets.
- Validation of the operative protocol proposed.
- Prototipal realization of a infrared imaging system to support the medical laser tool.
- Testing this approach for different pathologies and in different medical fields.

The output of this research could supply the doctor with very clear indications, according to the patient, on how to use the laser in terms of power and duration of the treatment. The final output will be a methodic scheme which could be employed by the operator no longer in an empirical way but now based on specific patient and phototype skin. The monitoring system which will be designed in the future in these activities could be of interest for medical industries which operate in this sector on a national and international scale.

References

- [1] R.R. Anderson, J.A. Parrish, "The optics of the human skin", *J. Invest Dermatol* 77,13 (1981).
- [2] M.H. Niemz, "Laser-Tissue Interactions", *Springer Berlin Heidelberg New York*, ch. 1 (2003).
- [3] S.O. Kasap, "Optoelectronics and Photonics: Principles and Practices", *Prentice-Hall*, ch.1 (2001).
- [4] A. Yariv, "Quantum Electronics", *John Wiley Interscience*, ch. 1 (1975).
- [5] L. Henvey, J. Greenstein, "Diffuse radiation in the galaxy", *Astrophys. J.* 93, pp. 70-83 (1941).
- [6] H.C. van de Hulst, "A new look at multiple scattering", *Tech. Report NASA, New York*, (1962).
- [7] J.H. Joseph, W.J. Wiscombe, J.A. Weinman, "The delta-Eddington approximation for radiative flux transfer", *J. Atmos. Sci.* 33, pp. 2452-2459 (1976).
- [8] L.O. Reynolds, N.J. McCormick, "Approximate two parameter phase function for light scattering", *J. Opt. Soc.* 70, pp. 1206-1212 (1980).
- [9] A. Vassiliadis, H.C. Christian, K.G. Dedrick, "Ocular laser threshold investigations", *Aerospace Med. Rep.* F41609-70-C0002 (1971).
- [10] W.S. Weinberg, R. Birngruber, B. Lorenz, "The change in light reflection of the retina during therapeutic laser-photocoagulation", *IEEE J. Qu. Electron.* QE – 20, pp. 1481-1489 (1984).
- [11] A.N. Takata, L. Zaneveld, W. Richter, "Laser induced thermal damage in skin. Aerospace Med", *Rep. SAM-TR-* pp. 77-38 (1977).
- [12] F.C. Henriques, "Studies of thermal injury", *Am. J. Pathol.* 23, pp. 489-502 (1947).
- [13] A. Roggan, G. Muller, "Computer simulations for the irradiating planning of LITT", *Med. Tech.* 4, pp. 18-24 (1993).
- [14] P. Teng, N.S. Nishioka, R.R. Anderson, T.F. Deutsch, "Acoustic studies of the role of immersion in plasma-mediated laser ablation", *IEEE J. Qu. Electron.* QE-23, pp. 1845-1852 (1987).
- [15] D. Stern, R.W. Schoenlein, C.A. Puliafito, E.T. Dobi, R. Birngruber, J.G. Fujimoto, "Corneal ablation by nanosecond, picosecond and femtosecond laser at 532 nm and 625 nm", *Arch. Ophthalmol.* 107, pp. 587-592 (1989).
- [16] M.H. Niemz, E.G. Klancnik, J.F. Bille, "Plasma mediated ablation of corneal tissue at 1053 nm using a Nd:YLF oscillator/regenerative amplifier laser", *Lasers Surg. Med.* 11, pp. 426-431 (1991).
- [17] F. Seitz, "On the theory of electron multiplications in crystals", *Phys. Rev.* 76, pp. 1376-93 (1949).
- [18] A.G. Molchanov, "Avalanche ionization in transparent dielectrics induced by intense light pulses", *Sov. Phys. Solid State* 12, 749, (1970).

- [19] N. Yablonovitch, N. Bloembergen, "Avalanche ionization and the limiting parameter of filaments induced by light pulses in transparent media", *Phys. Rev. Lett.* 29, pp. 907-910 (1972).
- [20] N. Bloembergen, "Laser induced electric breakdown in solids", *IEEE J. Qu Electron.* QE-10, pp. 375-386 (1974).
- [21] A.S. Epifanov, "Theory of electron-avalanche ionization induced in solids by electromagnetic waves", *IEEE J. Qu Electron.* QE-17, pp. 2018-2022 (1981).
- [22] C.A. Sacchi, "Laser-induced electric breakdown in water", *J. Opt. Soc. Am.* B8, pp. 337-45 (1991).
- [23] C.A. Puliafito, R.F. Steinert, "Short-pulsed Nd:YAG laser microsurgery of the eye: biophysical considerations", *IEEE J. Qu. Electron.* QE-20, pp. 1442-1448 (1984).
- [24] M.M. Krasnov, "Laserpuncture of anterior chamber angle in glaucoma", *Am. J. Ophthalmol.* 75, pp. 674-678 (1973).
- [25] D. Aron Rosa, J. Aron, J. Griesemann, R. Thyzel, "Use of the Nd:YAG laser to open the posterior capsule after lens implant surgery: a preliminary report", *J. Am. Intraocul. Implany. Soc.* 6, pp. 352-354 (1980).
- [26] F. Frankhauser, P. Roussel, J. Steffen, E. Van der Zypen, A. Chrenkova, "Clinical studies on the efficiency of high power laser radiation upon some structures of the anterior segment of the eye", *Int. Ophthalmol.* 3, pp. 129-139 (1981).
- [27] M.J.C. van Gemert, A.J. Welch, "Time constants in thermal laser medicine", *Laser Surg. Med.* 9, pp. 405-421 (1989).
- [28] W. Seipp, D. Haina, V. Seipp, "Laser in Dermatologie. Ing. Angewandte Lasermedizin", eds. H.P. Berlien, G. Muller, *Ecomed – Verlag, Landsberg* (1989).
- [29] O.T. Tan, K. Sherwood, B.A. Gilchrest, "Treatment of children with port-wine stains using the flashlamp-pulsed tunable dye laser", *N. Engl. J. Med.* 320, pp. 416-421 (1989).
- [30] R.R. Anderson, J. A. Parrish, "Selective photothermolysis: precise microsurgery by selective absorption of pulsed radiation", *Science* 220, pp. 524-527 (1983).
- [31] S. Kimel, L.O. Svaasand, T.E. Milner, M. Hammer-Wilson, M.J. Shell, J.S. Nelson, M.W. Berns, "Laser photothermolysis of single blood vessels in the chick chorioallantoic membrane (CAM)", *Proc. SPIE* 2077, pp. 216-226 (1994).
- [32] L.G. Astafeva, G.I. Zheltov, A.S. Rubanov, "Modeling of Blood Vessel Heating by Laser Radiation", *Phys. Qu. Opt.* 90, 2, pp. 287-292 (2000).
- [33] M.J.C. van Gemert, A.J. Welch, J.W. Pickering, O.T. Tan, G.H. Gijsberg, "Wavelengths for laser treatment of port wine stains and teleangiectasia", *Laser Surg. Med.* 16, pp. 147-155 (1995).
- [34] A. Scheibner, G. Kenny, W. White, R. G. Wheeland, "A superior method of tattoo removal using the Q-switched ruby laser", *J. Dermatol. Surg. Oncol.* 16, pp. 1091-1098 (1990).
- [35] C.R. Taylor, R.W. Gange, J.S. Dover, T.J. Flotte, E. Gonzalez, N. Michaud, R.R. Anderson, "Treatment of tattoos by Q-switched ruby laser. A dose response study", *Arch. Dermatol.* 126, pp. 893-899 (1990).

- [36] M.H. Niemz, "Cavity preparation with the Nd :YLF picosecond laser", *J. Dent. Res.* 74, pp. 1194-1199 (1995).
- [37] M. H. Niemz, "Ultrashort laser pulse in dentistry- advantages and limitations", *Proc. SPIE* 3255, pp. 84-91 (1998).
- [38] W.F. Wieland, H. Nicolai, W. Rössler, F. Hofstädter, *Proc. LASERmed 93*. Springer-Verlag, Berlin, Heidelberg, New York (1993)
- [39] M.H. Niemz, T.P. Hoppeler, T. Juhasz, J.F. Bille, "Intrastromal ablations for refractive corneal surgery using picosecond infrared laser pulse", *Laser light Ophthalm.* 5, pp. 149-155 (1993).
- [40] M. H. Niemz, F. H. Loesel, M. Fischer, C. Lappe, J.F. Bille, "Surface ablation of corneal tissue using UV, green and IR picosecond laser pulse", *Proc. SPIE* 2079, pp. 131-139 (1994).
- [41] R. Spring, J. Snell, "Infrared thermography", *The Engine Yearbook* (2004).
- [42] X.P.V. Maldague, "Theory and Practice of Infrared Technology for Nondestructive Testing", *John Wiley & Sons, New York* (2001).
- [43] H. Kaplan, "Practical applications of infrared thermal sensing and imaging equipment", *Proc. SPIE* TT13, 137, (1993).
- [44] H. Kaplan, "Process control using IR sensors and scanners", *Photonics Spectra*, Dec, pp. 92-95 (1997).
- [45] S. Marinetti, D. Robba, F. Cernuschi, P.G. Bison, E. Grinzato, "Thermographic inspection of TBC coated gas turbine blades: Discrimination between coating over-thicknesses and adhesion defects", *Infrared Physics & Technology* 49, pp. 281-285 (2007).
- [46] S.Å. Ljungberg, "Infrared techniques in building and structures: operation and maintenance", Ed. X.P.V. Maldague, "Infrared Methodology and Technology, International Advances in Nondestructive Testing", *Monograph Series*, pp. 211-252 (1994).
- [47] E. Grinzato, G.P. Bison, S. Marinetti, "Moisture evaluation by dynamic thermography data modelling", *Thermosense XVI, SPIE* 2245, Orlando (USA) (1994).
- [48] E. Rosina, N. Ludwig, L. Rosi, "Optimal conditions to detect moisture in ancient buildings. Study Cases from Northern Italy", *Thermosense XX-An International Conference in thermal sensing and imaging, diagnostic applications*, Orlando (USA) (1998).
- [49] E. Grinzato, G.P. Bison, S. Marinetti, V. Vavilov, "Thermal infrared non destructive evaluation of moisture content in building" *CNR Congress on Moisture*, Varenna (Italy) (1994).
- [50] Q. Li, E. Liasi, R. Du, J. Bujas-Dimitrijevic, A. Chen, "Heating of industrial sewing machine needles: FEA model and verification using IR radiometry", eds. D.H. Lemieux, J.R. Snell, *Thermosense XXI, Proc. SPIE*, 3700, pp. 347-357 (1999).
- [51] S.M. Shepard, "Advances in Pulsed Thermography", *Proceedings of SPIE, Thermosense XXIII*, Orlando (USA), pp. 511-515 (2001).
- [52] T. Sakagami, S. Kubo, "Applications of pulse heating thermography and lock-in thermography to quantitative nondestructive evaluations", *J. Infrared Phys Technol* 43, pp. 211-218 (2002).

- [53] N. Ludwig, P. Teruzzi, “Heat losses and 3D diffusion phenomena for defect sizing procedures in video pulse thermography”, *J. Infrared Phys. Technol.* 43, pp. 297–301 (2002).
- [54] N.P. Avdelidis, D.P. Almond, “Through skin sensing assessment of aircraft structures using pulsed thermography”, *NDT&E Int.* 37, pp. 353–362 (2004).
- [55] X.P.V. Maldague, A. Ziadi, M. Klein, “Double pulse infrared thermography”, *NDT&E International* 37, pp. 559–564 (2004).
- [56] A. Bendada, F. Erchiqui, M. Lamontagne, “Pulsed thermography in the evaluation of an aircraft composite using 3D thermal quadrupoles and mathematical perturbations”, *Inverse Problems* 21, pp. 857–877 (2005).
- [57] A. Bendada, C. Ibarra-Castanedo, X.P.V. Maldague, “A combined integral transform asymptotic expansion method for the characterization of interface flaws through pulsed infrared thermography”, *QIRT Journal* 4, 1, pp. 3-23 (2007).
- [58] D. Mailliet, J. C. Batsale, A. Bendada, A. De Giovanni, “Méthodes intégrales et contrôle non destructif par thermographie infrarouge stimulée”, *Rev Gen Therm* 35, pp. 14-27 (1996).
- [59] D.A. Gonzalez, C. Ibarra-Castanedo, X. Maldague, “New algorithm based on the hough transform for the analysis of pulsed thermographic sequences”, *NDT and E Internat.* 39, pp. 617-621 (2006).
- [60] X.P.V. Maldague, Y. Largoutit, J.P. Couturier, “A study of defect depth using neural networks in pulsed phase thermography: modelling, noise, experiments”, *Rev. Gen. Therm.* 37, pp. 704-717 (1998).
- [61] X.P.V. Maldague, S. Marinetti, “Pulse phase infrared thermography”, *J. Appl. Phys.* 79, 5, pp. 2694- 2698 (1996).
- [62] X.P.V. Maldague, F. Galmiche, A. Ziadi, “Advances in pulsed phase thermography”, *J Infrared Phys. Technol.* 43, pp. 175–81 (2002).
- [63] P. Cielo, X.P.V. Maldague, A. Deem, R. Lewak, “Thermographic NDE of industrial materials and structures”, *Mater. Eval.* 45, 12, pp. 452-460 (1987).
- [64] J. Allport, J. McHugh, “Quantitative evaluation of transient video thermography”, eds. D.O. Thompson and D.E. Chimenti. *Review of progress in quantitative nondestructive evaluation*, 7A, pp. 253-262 (1988).
- [65] V.P. Vavilov, R. Taylor, “Theoretical and practical aspects of the thermal nondestructive testing of bonded structures”, eds. R.S. Sharp. *Research techniques in nondestructive testing*, 5, pp. 238-279 (1982).
- [66] H.S. Carslaw, J.C. Jaeger, “Conduction of Heat in Solids”, 2nd ed. Oxford University (1959).
- [67] D. Mailliet, A.S. Houlbert, S. Didierjean, A.S. Lamine, A. Degiovanni, “Non-destructive thermal evaluation of delaminations in a laminate: I. Identification by measurement of thermal contrast”, *Composites Sci. Technol.* 47, pp. 137–53 (1993).
- [68] A. Bendada, “Reconstruction of a non uniform interface thermal resistance by inverse conduction”, *Inverse Problems in Engineering*, pp. 79–123 (1998).

- [69] D.A. Gonzalez, C. Ibarra-Castanedo, F.J. Madruga, X.P.V. Maldague, “Differentiated absolute phase contrast algorithm for the analysis of pulsed thermographic sequences”, *Infrared Physics and Technology* 48, pp. 16–21 (2006).
- [70] D.A. González, C. Ibarra-Castanedo, M. Pilla, M. Klein, J.M. López-Higuera, X.P.V. Maldague, “Automatic Interpolated Differentiated Absolute Contrast Algorithm for the Analysis of Pulsed Thermographic Sequence”, *Proc. 7th Conference on Quantitative InfraRed Thermography (QIRT)*, Rhode Saint Genèse (Belgium), pp. 5-8, H.16.1-H.16.6 (2004).
- [71] C. Ibarra-Castanedo, A. Bendada, X.P.V. Maldague, “Image and signal processing techniques in pulsed thermography”, *GESTS Int’l Trans. Computer Science and Engr.*, 22, 1, pp. 89-100 (2005).
- [72] L.D. Favro, H.J. Jin, Y.X. Wang, T. Ahmed, X. Wang, P.K. Kuo, R.L. Thomas, “IR Thermal wave tomographic studies of structural composites”, Thompson and D.E. Chimenti, *Review of progress in quantitative nondestructive evaluation*, 11A, pp. 447-452 (1998).
- [73] D. Wu, G. Busse, “Lock-in Thermography for NonDestructive Evaluation of Materials”, *Rev. Gén. Therm.*, 37, pp. 693-703 (1998).
- [74] W. Bai, B.S. Wong, “Evaluation of Defects in Composite Plates under Convective Environments using Lock-In Thermography”, *Meas. Sci. Technol.* 12, pp. 142-150 (2001).
- [75] C. Meola, G.M. Carlomagno, A. Squillace, G. Giorleo, “Nondestructive Control of Industrial Materials by Means of Lock-In Thermography”, *Meas. Sci. Technol.* 13, pp. 1583-1590 (2002).
- [76] D.L. Balageas, P. Levesque, A. Deem, “Characterization of electromagnetic fields using a lock-in infrared thermographic system”, ed. L.R. Allen, *Thermosense XV, Proceedings SPIE*, pp. 274-285 (1993).
- [77] R. Gupta, O. Breitenstein, “Unsteady-state lock-in thermography – Applications to shunts in solar cells”, *QIRT Journal* 4, 1, pp. 85-105 (2007).
- [78] D. Wu, H. Hamann, A. Salerno, G. Busse, “Lock-in thermography for imaging of modulated flow in blood vessels”, *Proc. QUIRT-96, Eurotherm Seminar* 50, pp. 343-347 (1996).
- [79] D. Pajani, “Thermographie IR: quelle longueur d’onde choisir I”, *Measures*, May, 71-76 (1987).
- [80] D. Pajani, “Thermographie IR: quelle longueur d’onde choisir II”, *Measures*, June, 77-80 (1987).
- [81] J.T. Woolaway, “New sensor technology for 3 to 5 μm imaging band”, *Photonics Spectra*. 25, 2, pp. 113-119 (1991).
- [82] A. Merla, L. Di Donato, S. Di Luzio, G. Romani, “Quantifying the Relevance and Stage of Disease with the Tau image Technique”, *IEEE Engineering in Medicine and Biology Magazine* 21, 6, pp. 86-91 (2002).
- [83] A. Merla, G. Romani, “Biomedical Applications of Functional Infrared Imaging”, *Proc. of the IEEE Engineering in Medicine and Biology 27th Annual Conference*, Shanghai (China) (2005).
- [84] A Merla, L Di Donato, G. Romani, “Assistance to surgery by means of infrared functional imaging: preliminary results”, *Proc. of the 23th Annual International Conference of IEEE Engineering in Medicine and Biology*, Proceedings CD, track 1264, Istanbul (Turkey) (2001).

- [85] A Merla, L. Di Donato, G. Romani, P. Rossini, "Infrared Functional Imaging Evaluation of the Sympathetic Thermal Response", *Proceedings of the 2nd European Medical and Biological Engineering Conference EMBEC02*, 2, 1610-1611 (2002).
- [86] I. Pavlidis, J. Levine, P. Baukol, "Thermal imaging for anxiety detection", *IEEE Workshop on computer Vision Beyond the Visible spectrum: Methods and Applications*. pp. 104-109, Hilton Head Island, South Carolina (USA) (2000).
- [87] M. Garbey, N. Sun, A. Merla, I. Pavlidis, "Contact-Free Measurement of Cardiac Pulse Based on the Analysis of Thermal Imagery", *IEEE Engineering in Medicine and Biology Magazine*, 54, 8, pp. 1418-1426 (2007).
- [88] A. Merla, A. Ledda, A. Di Donato, G. Romani, "Assessment of the effects of the varicocele on the thermoregulatory control of the scrotum", *Fertility and Sterility*, 81, 2, pp. 471-472 (2004).
- [89] A. Merla, A. Ledda, L. Di Donato, G. Romani, "Use of Infrared Functional Imaging to detect impaired thermoregulatory control in men with asymptomatic varicocele", *Fertility and Sterility* 78, 1, pp. 199-200 (2002).
- [90] A Merla, A Ledda, L Di Donato, G. Romani, "Dynamic Digital Telethermography: A novel approach to the diagnosis of varicocele", *Medical & Biological Engineering & Computing*, 37, pp. 1080-1081 (1999).
- [91] A. Merla, L. Di Donato, G. Romani, P. Rossini, "Recording of the Sympathetic Thermal Response by means of Infrared Functional Imaging", *Proc. of the 25th Annual International Conference of the IEEE EMBS*, Catalog No: 03CH37439C, Cancun (Mexico) (2003).
- [92] A. Merla, L. Di Donato, F. Salsano, G. Romani et al., "Raynaud's Phenomenon: infrared functional imaging applied to diagnosis and drugs effects", *International Journal of Immunopathology and Pharmacology* 15, 1, pp. 41-52 (2002).
- [93] A. Merla, F. Salsano, G. Romani et al., "Infrared Functional Imaging Applied to Raynaud's Phenomenon", *IEEE Engineering in Medicine and Biology Magazine* 21, 6, pp. 73-79 (2002)
- [94] A. Merla, L Di Donato, G. Farina, S. Pisarri, M. Proietti, F. Salsano, G. Romani, "Study of Raynaud's Phenomenon by means of infrared functional imaging", *Proc. of the 23th Annual International Conference of the IEEE EMBS*, Istanbul (Turkey) (2001).
- [95] O. Schuhfried, G. Vacariu, T. Lang, M. Korpan, H. P. Kiener, V. Fialka-Moser, "Thermographic Parameters in the Diagnosis of Secondary Raynaud's Phenomenon", *Arch Phys. Med. Rehabil.* 81 (2000).
- [96] M. Garbey, A. Merla, I. Pavlidis, "Estimation of Blood Flow Speed and Vessel Location from Thermal", *Video. Proc. of the IEEE Computer Society Conference on Computer Vision and Pattern Recognition (CVPR'04)*, 1, pp. 356-363 (2004).
- [97] N. Sun, M. Garbey A. Merla, I. Pavlidis, "Imaging the Cardiovascular Pulse", *Proc. of the IEEE Computer Society Conference on Computer Vision and Pattern Recognition (CVPR'05)* , 2, pp. 416-421 (2005).
- [98] N. Sun, I. Pavlidis, M. Garbey, J. Fei, "Harvesting the thermal cardiac pulse signal", *In International Conference on Medical Image Computing and Computer Assisted Intervention (MICCAI'06)*, 2, pp. 569 -576 (2006).

- [99] M. Yang, Q. Liu, T. Turner, Y. Wu, "Vital sign estimation from passive thermal video", *Computer Vision and Pattern Recognition. IEEE Conference*, pp. 1-8 (2008).
- [100] J. R. Keyerserlingk, P. D. Ahlgren, E. Yu, N. Belliveau, M. Yassa, "Functional Infrared Imaging of the breast", *IEEE Eng. Med. Biol.*, 19, 3, pp.30-42, (2000).
- [101] M. Anbar, C. Brown, L. Milesco, J. Babalola, L. Gentner, "The potential of dynamic area telethermometry in assessing breast cancer", *IEEE Eng. Med. Biol.*, 19, 3, pp.58-62 (2000).
- [102] M. Anbar, C. Brown, L. Milesco, J.A. Babalola, "Clinical Applications of DAT using a QWIP FPA camera", *SPIE Proc.* 3698, pp. 93-104. (1999).
- [103] S.W. Lanigan, J.A. Cotterill, "Psychological disabilities amongst patients with port wine stains", *Br. J. Dermatol.* 121, 2, pp. 209-15 (1989).
- [104] A.W. Bush A, "Perturbation Methods for Engineers and Scientists", *Boca Raton, FL: CRC* (1992).
- [105] A. Aziz , T. Na , "Perturbations Methods in Heat Transfer", *Berlin: Springer* (1984).
- [106] A. Bendada, "Approximate solutions to three-dimensional unsteady heat conduction through plane flaws within anisotropic media using a perturbation method", *Modelling Simul. Mater. Sci. Eng.* 10, pp. 673-84 (2002).
- [107] D. Maillet, S. Andre, J.C. Batsale, A. Degiovanni, C. Moyne, "Thermal Quadrupoles: Solving the Heat Equation Through Integral Transforms", *Chichester: Wiley* (2000)
- [108] H. Stehfest, "Remarks on algorithm 368, numerical inversion of Laplace transforms", *Commun. ACM*, pp. 624, (1970).
- [109] D. Maillet, A. Houlbert, S. Didierjean , A.S. Lamine, A. Degiovanni, "Non-destructive thermal evaluation of delaminations in a laminate: I. Identification by measurement of thermal contrast", *Composites Sci. Technol.* 47, pp. 137-53 (1993).
- [110] J. Werner, M. Buse, "Temperature Profiles with Respect to Inhomogeneity and Geometry of the Human Body", *Journal of Applied Physiology* 65, 3, pp. 1110-1118 (1988).
- [111] L. Myron, P. Cohen, "Measurement of the thermal properties of the human skin. A review", *The J. Invest. Dermatol.* 69, pp. 333-338 (1977).
- [112] A.J. Welch, M.J.C. van Gemert, "Optical-Thermal Response of Laser-Irradiated Tissue", ed. *Plenum Press*, NY (1995).
- [113] L.F. Douven, G.W. Lucassen, " Retrieval of optical properties of skin from measurement and modeling the diffuse reflectance", *Proc. SPIE*, 3914, pp. 312-323 (2000).
- [114] W.G. Zijlstra, A. Buursma, O. W. van Assendelft, "Visible and Near Infrared Absorption Spectra of Human and Animal Haemoglobin", *VSP Publishing*, Utrecht (2000).

- [115] A. Roggan, M. Friebel, A. Hahn, G. Muller, "Optical properties of circulating human blood in the wavelength range 400-2500 nm", *J. Biomed. Opt.* 4, pp.36-46, (1999).
- [116] J. W. Pickeringt, P.H. Butler, B.J. Ring, E.P. Walker, "Computed temperature distributions around ectatic capillaries exposed to yellow (578 nm) laser light", *Phys. Med. Biol.* 34, 9, pp. 1247-1258 (1989).
- [117] G.W. Lucassen, W.V., M. Keijzer, M.J.C. van Gemert, "Light Distributions in a Port Wine Stain Model Containing Multiple Cylindrical and Curved Blood Vessels", *Lasers in Surgery and Medicine* 18, 345-357 (1996)